

Fair real-time control of energy storage systems in active distribution networks in the presence of uncertainties

Présentée le 26 juin 2024

Faculté des sciences et techniques de l'ingénieur
Laboratoire des systèmes électriques distribués
Programme doctoral en informatique et communications

pour l'obtention du grade de Docteur ès Sciences

par

Plouton GRAMMATIKOS

Acceptée sur proposition du jury

Prof. O. N. A. Svensson, président du jury
Prof. M. Paolone, Prof. J.-Y. Le Boudec, directeurs de thèse
Dr A. Bernstein, rapporteur
Dr D. Shchetinin, rapporteur
Prof. R. Cherkaoui, rapporteur

τὸ τὰ αὐτοῦ πράττειν
καὶ μὴ πολυπραγμονεῖν
δικαιοσύνη ἐστὶ
**(doing one's own business
and not being involved in many works,
that is justice)**
— Plato, Republic, Book 4 (section 433a)

To my parents...

Acknowledgements

First, I would like to thank the two advisors of my PhD thesis, Mario Paolone and Jean-Yves Le Boudec. I was lucky enough to have two wonderful advisors throughout this journey, and I feel it is necessary to acknowledge their equal contribution to my PhD supervision. They were always available when I needed them, and their advice and guidelines helped me improve my theoretical and experimental skills. I would also like to thank the members of my PhD jury, Rachid Cherkaoui, Andrey Bernstein, Dmitry Shchetinin, and Ola Svensson, who gave me valuable comments and suggestions to improve the quality of my thesis.

Throughout my PhD, I had the chance to be a member of two amazing labs, DESL and LCA2, and I collaborated with multiple people. I want to acknowledge the contribution of all my colleagues to my thesis and personal development. First, special thanks to Jagdish, who was my mentor together with Jean-Yves and Mario during the first semesters of my PhD. His guidance led to developing the methods of Chapters 2 and 4 of my thesis. I would also like to acknowledge the help of my colleagues from DESL in running the experiments carried out in my thesis. Specifically, I would like to thank Sherif, or "the COMMELEC expert" as Mario introduced him, who helped me learn the basics of COMMELEC during my first semester at EPFL. Rahul's contribution to setting up and carrying out the experiments of Section 5.2 was immense, as was the help of Francesco and Matthieu in controlling the batteries for the experiments of Section 5.3. Finally, I would like to thank Fabrizio, who allowed me to continue his work on ultra-short-term forecasting, which led to Chapter 3 of my thesis.

Next, I would like to thank my colleagues from LCA2 who I collaborated with in TAing the courses "TCP/IP networking" and "smart grids technologies." Special thanks to Hossein, Alaeddine, Ludovic, St'ephan, and Sounak for being part of this amazing TA team.

I would also like to acknowledge all the people in DESL and the other groups at ELL who made my PhD life enjoyable. I would first like to give a special thanks to César, who has been my office-mate for the past two years and made life at the office much more amusing by constantly making jokes and showing me random videos. Thanks as well to Alex, Johanna, Vlad, Simone, Willem, Max, Enea, Ji, Yihui, Ehsan, Thomas, Elias, and all the others who participated in the BBQs and the crazy grilling experiments I organized.

I am also grateful to all the new friends I made outside the lab environment during the first year of PhD. I am especially grateful to the following people: Aditya, for being the best travel buddy I could ever have; Daniel and Guohao for also joining me on trips, as well as on philosophy, cocktail, dinner, and movie nights; Dina, Michal, and Lars for being the main organizers of game nights and for helping me with the cooking in our regular "master classes"; Nicolas

Acknowledgements

for eating most of the food on those classes and for always complimenting my cooking and “game-mastering” skills; Valentin for posting some of the best memes on our meme group, and Rodrigo for truly being engaged in our philosophical discussions and for doing me the honor of asking me to be a witness in his wedding.

Finally, I would like to thank my family for always supporting me during my PhD. First, I want to thank my father, Vasileios, for always giving me the best advice regarding life decisions and ensuring I eat well by sending me the best quality olive oil to “feed my brain”, as he says. Next, my mother, Xanthi, was always there for me when things with my PhD were not going well and was always able to shift my mood for the better. Last but not least, I want to thank my brother Panagiotis, who made my evenings enjoyable with our regular video calls and game nights.

Lausanne, June 11, 2024

Plouton Grammatikos

Abstract

Active distribution networks (ADN) are a prominent solution to tackle the challenges caused by the large integration of distributed energy resources (DERs). Using suitable control strategies, distribution system operators (DSOs) can optimally balance supply and demand and satisfy their grid's operational constraints. However, achieving reliable control is particularly challenging due to the high volatility of renewable energy resources. Moreover, as more individuals own DERs, fair control might be desirable, which might compromise other objectives if not treated carefully. The thesis explores the issue of fairness in the presence of uncertainties by proposing and experimentally validating appropriate control frameworks for ADNs.

In particular, we address two issues in the state-of-the-art of real-time (RT) control of the DERs. The first one is the inadequacy of existing frameworks to handle fairness. We focus on the problem of controlling battery energy storage systems (BESSs) owned by different individuals to dispatch an ADN in RT. In this case, the DSO should, ideally, ensure that their states-of-charge (SoCs), relative to their energy capacities, are equal. In most relevant works in the literature, fairness can be controlled by tuning the controller's parameters, such as the weights of its objectives. Typically, the weights are manually tuned by evaluating the controller's performance a posteriori until a satisfactory result is obtained. These "oracle-based" approaches are impractical as they assume knowledge of the realization of the stochastic resources. To address the issues with these approaches, we propose a method to design cost functions for different RT objectives and compute their weights. The design is made such that dispatching is guaranteed with a given accuracy, and the control among BESSs is fair, i.e., their SoCs are as close as possible to each other, while a safe grid operation is guaranteed. The method translates the weights into parameters the user can intuitively choose without manual tuning. It is evaluated with simulations in various scenarios, showing its superiority over the oracle-based approaches in designing the controller's objective.

The second issue not adequately addressed by the existing literature is quantifying the uncertainty of the stochastic energy resources, which is important to ensure the controller's reliable operation. Even though the problem of quantifying uncertainty has been extensively studied in the literature, the horizons targeted by most works are much longer than what is suitable for RT control. Instead, we target ultra-short-term horizons, i.e., up to a few seconds, and propose an algorithm to compute prediction intervals (PIs) for the prosumption of heterogeneous resources. The algorithm provides a model-free approach to estimating the statistical distribution of the uncertain power of prosumers without making any assumptions about the stochastic nature of the prosumption. It has been evaluated on various prosumers with

Abstract

different power profiles and was shown to compute relatively narrow PIs with high confidence levels for time resolutions of up to 10 seconds.

After the simulation validation, an extensive experimental campaign was conducted to evaluate the methods developed in the thesis in dispatching BESSs with a fair SoC regulation. We evaluated the performance of two control frameworks using the proposed methods for the PI computation and the design of the controller's objective. The experiments were carried out in a medium voltage utility-scale grid in Aigle, Switzerland, and the EPFL smart-grid platform and demonstrated how the methods developed in the thesis can successfully control BESSs fairly for dispatching while accounting for binding grid constraints.

Keywords: Active distribution networks, energy storage systems, real-time control, optimization-based control, objective balancing, state-of-charge balancing, fairness, ultra-short-term forecasting, prediction intervals, experimental validation

Résumé

Les réseaux de distribution actifs (RDA) sont une solution de premier plan pour relever les défis posés par l'intégration à grande échelle des ressources énergétiques distribuées (RED). En utilisant des stratégies de contrôle appropriées, les gestionnaires de réseaux de distribution (GRD) peuvent équilibrer de manière optimale l'offre et la demande, ainsi que satisfaire les contraintes opérationnelles de leur réseau. Toutefois, l'obtention d'un contrôle fiable est particulièrement difficile en raison de la forte volatilité des ressources énergétiques renouvelables. De plus, comme de plus en plus d'individus possèdent des RED, un contrôle équitable pourrait être souhaitable, ce qui pourrait compromettre d'autres objectifs s'il n'est pas traité avec soin. La thèse explore la question de l'équité en présence d'incertitudes en proposant et en validant de façon expérimentale des environnements de contrôle appropriés pour les RDA.

En particulier, nous abordons deux problèmes dans l'état de l'art du contrôle en temps réel (TR) des RED. En premier lieu, nous traitons celui de l'inadéquation des contrôles existants pour gérer l'équité. Notre attention porte sur le problème du contrôle des systèmes de stockage d'énergie par batterie (SSEB) appartenant à différents individus pour répartir (dispatch) un RDA en temps réel. Dans ce cas, le GRD devrait, idéalement, s'assurer que leurs états de charge (EdC), relatifs à leurs capacités énergétiques, sont égaux. Dans la plupart des travaux pertinents de la littérature, l'équité peut être contrôlée en réglant les paramètres du contrôleur, tels que les poids de ses objectifs. En général, les poids sont réglés manuellement en évaluant les performances du contrôleur a posteriori jusqu'à ce qu'on obtienne un résultat satisfaisant. Ces approches "basées sur l'oracle" ne sont pas pratiques car elles supposent que nous connaissons la réalisation des ressources stochastiques. En vue de résoudre les problèmes posés par ces approches, nous proposons une méthode pour concevoir des fonctions de coût pour différents objectifs de TR ainsi que pour calculer leurs poids. La conception est faite de telle sorte que la répartition (dispatching) soit garantie avec une précision donnée et que le contrôle entre les SSEB soit équitable, c'est-à-dire que leurs EdC soient aussi proches que possible les uns aux autres, tout en garantissant un fonctionnement sécurisé du réseau. La méthode interprète les poids par des paramètres que l'utilisateur peut choisir intuitivement sans réglage manuel. Nous l'avons évaluée à l'aide des simulations dans divers scénarios, montrant sa supériorité sur les approches basées sur l'oracle dans la conception de l'objectif du contrôleur.

En deuxième lieu, nous traitons la quantification de l'incertitude des ressources énergétiques stochastiques, qui est importante pour garantir la fiabilité du fonctionnement du contrôleur,

Résumé

et qui n'est pas traitée de manière adéquate dans la littérature existante. Même si le problème de la quantification de l'incertitude a été largement étudié dans la littérature, les horizons de prévision visés par la plupart des travaux sont beaucoup plus longs que ce qui est approprié pour le contrôle du TR. Par contre, ce sont les horizons à très court terme auxquels nous visons, à savoir des horizons de 20 ms à quelques secondes, et c'est pour cela que nous proposons un algorithme afin de calculer les intervalles de prédiction (IP) pour la prosommation (production/consommation) de ressources hétérogènes. L'algorithme fournit une approche sans modèle pour estimer la distribution statistique de la puissance incertaine des prosommateurs sans faire des hypothèses sur la nature stochastique de la prosommation. Nous l'avons évalué sur divers prosommateurs avec différents profils de puissance et on a démontré qu'il calcule des IP relativement étroits avec des niveaux de confiance élevés pour des résolutions temporelles allant jusqu'à 10 secondes.

Après la validation des simulations, une vaste campagne expérimentale a été menée pour évaluer les méthodes développées dans la thèse dans la répartition des SSEB avec une régulation équitable de l'EdC. Nous avons évalué la performance de deux environnements de contrôle en utilisant les méthodes proposées pour le calcul des IP et la conception de l'objectif du contrôleur. Les expériences ont été menées sur un réseau de moyenne tension à Aigle, en Suisse, et sur la plateforme smart-grid de l'EPFL. Elles ont démontré que les méthodes développées dans la thèse peuvent contrôler équitablement les SSEB pour la répartition du RDA tout en prenant en compte les contraintes du réseau.

Mots clés : Réseaux de distribution actifs, systèmes de stockage d'énergie, contrôle en temps réel, contrôle basé sur l'optimisation, équilibrage des objectifs, équilibrage de l'état de charge, équité, prévision à très court terme, intervalles de prévision, validation expérimentale

Contents

| | |
|---|-------------|
| Acknowledgements | i |
| Abstract (English/Français) | iii |
| List of Figures | xi |
| List of Tables | xv |
| Nomenclature | xvii |
| 1 Introduction | 1 |
| 1.1 Motivation | 1 |
| 1.2 Structure of Thesis | 2 |
| 2 Real-Time Control of Active Distribution Networks | 5 |
| 2.1 State of the Art | 5 |
| 2.1.1 Active Distribution Networks Architecture | 5 |
| 2.1.2 Real-Time Control and Economic Dispatch | 6 |
| 2.1.3 Fairness Indicators in Electricity Markets | 10 |
| 2.1.4 Fairness in Real-Time Control of Battery Energy Storage Systems | 13 |
| 2.1.5 Ultra-Short-Term Electricity Forecasting | 15 |
| 2.1.6 Contributions to the State of the Art | 17 |
| 2.2 Real-Time Control Problem Formulation | 17 |
| 2.2.1 Optimization Problem | 17 |
| 2.2.2 Convexity of the Problem | 19 |
| 2.3 Examples of Cost Functions | 21 |
| 2.3.1 Battery Cost Function | 21 |
| 2.3.2 ADN Slack Cost Function | 21 |
| 2.3.3 ADN Voltage Cost Function | 21 |
| 2.3.4 ADN Branch Current Cost Function | 22 |
| 2.3.5 Total Grid Cost Function | 23 |
| 2.4 Configuring the Weights of the Controller | 23 |
| 2.4.1 Simulation Setup | 24 |
| 2.4.2 First Scenario - The Oracle-Based Approach | 27 |
| 2.4.3 Second Scenario - Larger Load Consumption | 30 |
| | vii |

Contents

| | | |
|----------|--|-----------|
| 2.4.4 | Third Scenario - Change In the Topology | 32 |
| 2.4.5 | Discussion | 33 |
| 3 | Quantification of Ultra-Short-Term Uncertainty of Heterogeneous Resources in Active Distribution Networks | 35 |
| 3.1 | Purpose of Chapter | 35 |
| 3.2 | Computation of Prediction Intervals | 36 |
| 3.2.1 | PI Model A | 37 |
| 3.2.2 | PI Model B | 40 |
| 3.2.3 | Classification According to Influential Variables | 40 |
| 3.2.4 | Implementation Aspects and Complexity | 42 |
| 3.3 | Performance Evaluation | 43 |
| 3.3.1 | A real case application: university buildings | 43 |
| 3.3.2 | Performance Metrics | 43 |
| 3.3.3 | Clustering Using Power Levels | 45 |
| 3.3.4 | Clustering Using Power Levels and Time of Day | 51 |
| 3.3.5 | Comparison with a Persistent Forecaster | 53 |
| 3.3.6 | Effect of the Measurement Period | 54 |
| 3.3.7 | Confidence Level Uncertainty | 57 |
| 3.4 | Conclusion | 58 |
| 4 | Design of Cost Functions for the Fair Control of Battery Energy Storage Systems | 61 |
| 4.1 | Purpose of Chapter | 61 |
| 4.2 | Battery Cost Function | 62 |
| 4.2.1 | Fair Control of Batteries | 62 |
| 4.2.2 | General Form of a Battery Cost Function | 63 |
| 4.3 | Grid Objective | 66 |
| 4.3.1 | Computing the Weights w_{y_m} | 66 |
| 4.3.2 | Application to Specific Grid Objectives | 70 |
| 4.3.3 | Visual Representation of the Computed Upper Bound | 70 |
| 4.3.4 | Multiple Objectives | 72 |
| 4.3.5 | Discussion of the Limitations of the Method | 73 |
| 4.4 | Numerical Validation of the Proposed Method | 73 |
| 4.4.1 | Evaluation Metrics | 73 |
| 4.4.2 | Evaluation of the Proposed Method in the Scenarios of Section 2.4 | 74 |
| 4.4.3 | Applicability of the Proposed Method in a Different Control Framework | 80 |
| 4.5 | Discussion and Limitations of the Proposed Method | 82 |
| 5 | Experimental Validation of the Proposed Control Framework for Battery Energy Storage Systems | 85 |
| 5.1 | Introduction | 85 |
| 5.2 | Dispatch Tracking in a Utility-Scale Grid Using the COMMELEC Framework | 86 |
| 5.2.1 | Dispatch Plan Computation | 87 |

| | | |
|----------|---|------------|
| 5.2.2 | The COMMELEC Framework | 87 |
| 5.2.3 | Experimental Setup | 89 |
| 5.2.4 | Experimental Results | 94 |
| 5.3 | A Two-Layer Control Approach for the Fair Control of multiple BESSs | 96 |
| 5.3.1 | Control Framework | 97 |
| 5.3.2 | Intra-Day MPC | 99 |
| 5.3.3 | Real-Time Control | 103 |
| 5.3.4 | Experimental Setup | 105 |
| 5.3.5 | Intra-Day Forecasting | 108 |
| 5.3.6 | Experimental Results | 110 |
| 5.4 | Conclusion and Impact of Experiments | 113 |
| 6 | Conclusion | 115 |
| A | Proofs of Theorems of Chapter 4 | 117 |
| A.1 | Proof of Theorem 4.2 | 117 |
| A.2 | Proof of Lemma 4.1 | 119 |
| A.3 | Proof of Theorem 4.4 | 121 |
| | Bibliography | 132 |
| | Curriculum Vitae | 133 |

List of Figures

| | | |
|------|---|----|
| 2.1 | Centralized ADN architecture. | 6 |
| 2.2 | Decentralized ADN architecture. | 7 |
| 2.3 | Different electricity markets and timeline (adapted from [1]). | 8 |
| 2.4 | Two-layer control framework. | 9 |
| 2.5 | Internal details of the control layer. | 10 |
| 2.6 | Interaction between sensing, actuating, and RT control layers. | 18 |
| 2.7 | Voltage cost function. | 22 |
| 2.8 | Microgrid topology. Bus 0 is the slack bus. | 24 |
| 2.9 | Equivalent circuit diagram of BESS | 25 |
| 2.10 | Short-term predictions and realizations of the stochastic power injections in the microgrid of Fig. 2.8. | 27 |
| 2.11 | Simulation results of the first scenario with equal weights for all objectives. The bottom-right graph shows the target trajectory for the SoC of the BESSs that was computed by the dispatcher. | 28 |
| 2.12 | Simulation results of the first scenario with manually picked weights: slack weight $w_s = 1$, voltage weight $w_V = 10^{-6}$, current weight $w_I = 10^{-5}$, battery weights $w_1 = w_2 = 10^{-4}$ | 29 |
| 2.13 | Simulation results of the second scenario, with higher load consumption, with weights: slack weight $w_s = 1$, voltage weight $w_V = 10^{-6}$, current weight $w_I = 10^{-5}$, battery weights $w_1 = w_2 = 10^{-4}$ | 30 |
| 2.14 | SoC of BESSs for two different load profiles and sets of weights. | 31 |
| 2.15 | Simulation results for the third scenario, with normal load consumption and a bigger BESS 1 at 60 kVA/60 kWh. The weights are the same as in the first scenario. | 32 |
| 3.1 | Operation sequence of the PI estimation models. The batch training is performed off-line, whereas the PIs computation and on-line training are performed in rolling RT. Ellipses denote the input and output of each phase. | 36 |
| 3.2 | Exemplification of the procedure (3.10)-(3.11) to approximate the quantiles for (3.8)-(3.9) for a normal distribution. In this case, the target confidence level α is 80%. | 38 |
| 3.3 | Visualization of k-means clustering for a node with an EV charging station with 8 clusters and using the power level and the time of day as influential variables. Positive power is consumption. | 41 |

List of Figures

| | | |
|------|---|-----|
| 3.4 | Normalized PDF of power prosumption for the studied prosumers. To aid readability, the x-axis has been limited to a 99.9% confidence level. | 44 |
| 3.5 | Visual representation of the CWC. $\text{error} = 1 - \text{PICP}$ is the error rate of the algorithm, and $\text{target} = 1 - \alpha$ is the target error rate. The red line indicates Equation (3.23) with the chosen value of μ , and the blue line indicates a linear penalty. | 50 |
| 3.6 | Comparison between our algorithm and a persistent forecaster for the office building. | 53 |
| 3.7 | Performance evaluation as a function of the measurement period | 55 |
| 3.8 | Box plot of model accuracy versus target confidence level at 20 ms resolution | 57 |
| 4.1 | True value of $ y_m^{real} - y_m^* $ and theoretical upper bound as a function of the weight w_{y_m} , for different values of d . The curve corresponding to the desired upper bound is the one for $d = d_{max,m}^* - \Delta y_m _{max} = 200$ W and is shown in the bottom plot. | 71 |
| 4.2 | Evaluation metric for the batteries objective. | 73 |
| 4.3 | Simulation results for the scenario of Section 2.4.2 with our proposed weight-computation method. | 75 |
| 4.4 | Simulation results for the scenario of Section 2.4.3 (higher load consumption) with our proposed weight-computation method and total grid-cost unction given by (4.24) | 78 |
| 4.5 | Simulation results for the scenario of Section 2.4.3 (higher load consumption) with our proposed weight-computation method and total grid-cost-function given by (4.25). | 79 |
| 4.6 | Simulation results for the scenario of Section 2.4.4 (bigger BESS 1 at 60 kVA/60 kWh) with our proposed weight-computation method. | 80 |
| 4.7 | Simulation results for the problem defined in [2] for three different weight configurations. | 81 |
| 5.1 | Schematic diagram of the control framework using COMMELEC. | 86 |
| 5.2 | Structure of the COMMELEC decision cycle. | 88 |
| 5.3 | Topology of the MV distribution network in Aigle. | 90 |
| 5.4 | IT infrastructure in Aigle. | 92 |
| 5.5 | COMMELEC decision cycle in the Aigle demonstrator. | 93 |
| 5.6 | Example of a Shadow Agent and the Battery Agent's PQ profile (blue) and Belief Function (red) for the implemented setpoint. | 94 |
| 5.7 | Dispatch plan tracking before (top) and after (bottom) COMMELEC control. | 95 |
| 5.8 | Performance comparison between COMMELEC and MPC. | 96 |
| 5.9 | Schematic diagram of the control framework. | 97 |
| 5.10 | Intra-day and real-time operation (executed in parallel). | 98 |
| 5.11 | π model of a branch | 99 |
| 5.12 | Intra-day (top) and real-time (bottom) time axis for a given time slice. | 103 |
| 5.13 | Topology of the distribution network at EPFL. Bus 1 is the slack bus. | 106 |
| 5.14 | IT infrastructure of the EPFL smart-grid platform. | 108 |

5.15 Expected SoC trajectories computed by the intra-day MPC for the first experiment. Each colored line corresponds to one scenario, whereas the bold black line indicates the median trajectory used by the RT control. 109

5.16 Dispatch plan tracking and BESS power and SoC for the first experiment. Positive power indicates the importing of energy from the upper grid at the top plot and the discharging of BESS at the third plot. 110

5.17 Grid state measured by PMUs for the first experiment. 111

5.18 Results for the second experiment, with artificially reduced ampacity of branch 6-8. The bold line in the second graph indicates the current of branch 6-8. . . . 112

List of Tables

| | | |
|-----|--|-----|
| 3.1 | Performance Evaluation for the Office Building at 20 ms resolution (5 best configurations) | 46 |
| 3.2 | Performance Evaluation for the Charging Station at 20 ms Resolution (5 best configurations) | 47 |
| 3.3 | Performance Evaluation for the Heat Pump at 20 ms Resolution (5 best configurations) | 48 |
| 3.4 | Performance Evaluation for the MV Feeders at 20 ms Resolution (5 best configurations) | 49 |
| 3.5 | Best Configuration at 20 ms Resolution - Clustering Based on Power (P) and Power+Time of Day (P+TOD) | 52 |
| 3.6 | Best Configuration as a Function of the Measuring Period | 56 |
| 4.1 | Value of metrics for the scenario of section 2.4.2 with the oracle-based approach and the proposed method. | 76 |
| 4.2 | Value of metrics for the scenario of section 2.4.3 (higher load consumption). | 77 |
| 4.3 | Value of metrics for the scenario of section 2.4.4 (bigger BESS 1 at 60kVA/60kWh). | 81 |
| 5.1 | Technical specifications of the BESS used for the experiments of Section 5.2 (adapted from [3]). | 91 |
| 5.2 | Technical specifications of BESSs used for the experiments of section 5.3 (adapted from [4]). | 107 |

Nomenclature

Glossary

COMMELEC A framework for the real-time control of electrical grids that computes explicit active and reactive power setpoints of the nodal injections.

Dispatchability The ability of an energy resource or power system to increase and decrease its output quickly on demand.

Oracle-based approach: The conventional approach to configuring the weights of the optimization problem. It relies on running extensive simulations with varying weights and evaluating the performance of the control a posteriori.

Prosumer: An individual who can both produce and consume electricity.

Prosumption: The aggregated power provided or consumed by users that have the capability to generate electricity by means of user-owned distributed generation locally.

Abbreviations

ADN Active Distribution Network.

BA Battery Agent.

BESS Battery Energy Storage System.

BMS Battery Management System.

CDF Cumulative Distribution Function.

CI Confidence Interval.

CWC Coverage Width-based Criterion.

DER Distributed Energy Resource.

DSO Distribution System Operator.

Symbols of real-time control

ESS Energy Storage System.

EV Electric Vehicle.

EVCS Electric Vehicle Charging Station.

GA Grid Agent.

LV Low Voltage.

MPC Model Predictive Control.

MV Medium Voltage.

PCC Point of Common Coupling.

PDF Probability Density Function.

PI Prediction Interval.

PICP Prediction Interval Coverage Probability.

PINAW Prediction Interval Normalized Averaged Width.

PMU Phasor Measurement Unit.

PV Photovoltaic.

RA Resource Agent.

RT Real Time.

SA Shadow Agent.

SoC State of Charge.

TOD Time of Day.

Symbols of real-time control

\mathcal{A}_i Constraint set of BESS i .

ΔSoC_i Difference between SoC of BESS i and its target value.

β_{hard} Hard voltage tolerance.

β_{soft} Soft voltage tolerance.

γ_{soft} Soft current tolerance.

$C_i(\cdot)$ Cost function of BESS i .

$C_{tot}(\cdot)$ Total objective.

I_l Current magnitude of branch l .

I_l^+ Sum of real and imaginary parts of complex current phasor for branch l .

I_l^- Difference between real and imaginary parts of complex current phasor for branch l .

I_l^{max} Ampacity of branch l .

$J'_{y_m}(\cdot)$ Derivative of J_{y_m} with respect to y_m .

$J(\cdot)$ Total grid objective.

$J_{y_m}(\cdot)$ Grid objective for variable y_m .

K Number of buses.

$K_{\mathcal{P},n}^m, K_{\mathcal{Q},n}^m$ Sensitivity coefficients of grid variable y_m with respect to the active and reactive power of uncontrollable prosumption n .

$K_{P,i}^m, K_{Q,i}^m$ Sensitivity coefficients of grid variable y_m with respect to the active and reactive power of BESS i .

$K_{x_i}^m$ Sensitivity coefficient of grid variable y_m with respect to x_i . Here, x_i can represent any BESS active or reactive power injection.

L Number of branches.

N_B Number of BESSs.

P^{DP} Active-power tracking value at the slack bus computed by the dispatcher.

P_s, Q_s Active and reactive power at the slack bus.

S_i Rated power of BESS i .

SoC_i State of Charge of BESS i .

SoC_i^{target} Target SoC value for BESS i computed by the day-ahead or intra-day layer.

T Period of control.

U Number of stochastic, uncontrollable energy resources.

V_k Voltage magnitude at bus k .

V_{nom} Nominal voltage.

a_p, a_Q Coefficients of battery cost function.

Symbols of intra-day control

$d_{max,m}^*$ Desired upper bound for grid variable y_m .

$r_{P,i}, r_{Q,i}$ Preference ratios of BESS i with respect to active and reactive power.

w_{y_m} Weight of grid objective for variable y_m .

$x_{i,min}, x_{i,max}$ Minimum and maximum active or reactive power of BESS i .

y_m Grid variable m . It can represent any nodal voltage, power injection, or branch current.

y_m^* Target value to be achieved by the grid objective of variable y_m .

y_m^{inf} The value of y_m within its domain that minimizes the value of J_{y_m} .

y_m^{min}, y_m^{max} Minimum and maximum value of grid variable y_m .

y_m^{opt} Optimal value of grid variable y_m .

y_m^{real} Realization of grid variable y_m .

$|\Delta y_m|_{max}$ Maximum uncertainty of grid variable y_m .

$|K^m|_{min}$ Minimum absolute value of sensitivity coefficients of grid variable y_m among all BESS setpoints.

$|P_s - P^{DP}|_{max}$ Soft slack-active-power-tracking tolerance.

$|Q_s|_{max}$ Soft slack-reactive-power tolerance.

$\hat{\mathbf{u}}$ One-step-ahead forecast of stochastic power injections.

\mathbf{u} Set of stochastic power injections.

$\mathbf{u}_n = (\mathcal{P}_n, \mathcal{Q}_n)$ Active and reactive power of stochastic prosumer n .

\mathbf{x} Set of BESS setpoints.

$\mathbf{x}_i^* = (P_i^*, Q_i^*)$ Preference of BESS i .

$\mathbf{x}_i = (P_i, Q_i)$ Active and reactive power setpoint of BESS i .

$\mathbf{x}_i^{opt} = (P_i^{opt}, Q_i^{opt})$ Solution of the RT optimization problem for BESS i .

Symbols of intra-day control

κ Time step.

F_κ Offset profile.

$S_{l,\kappa}^d = P_{l,\kappa}^d + jQ_{l,\kappa}^d$ Apparent power entering branch l from the top of the branch.

T_1 Time period of real-time control.

T_2 Time period of intra-day control.

$V_{l,\kappa}^d$ Voltage magnitude at the node at the bottom of branch l .

$V_{up(l),\kappa}^d$ Voltage magnitude at the node at the top of branch l .

b_l Shunt capacitance of branch l .

d Index of scenario.

$f_{l,\kappa}^d$ Square of the current flowing through the series branch impedance z_l .

$i_{l,\kappa}^d, i_{l,\kappa}^{b,d}$ Current magnitudes entering branch l from the top and bottom of branch respectively.

l Index of branch.

$s_{i,\kappa}^{B,d} = p_{i,\kappa}^{B,d} + jq_{i,\kappa}^{B,d}$ Power injected by BESS i .

$s_{l,\kappa}^d = p_{l,\kappa}^d + jq_{l,\kappa}^d$ Total power injected at bus l .

$v_{l,\kappa}^d$ Square of voltage magnitude at the node at the bottom of branch l .

$v_{up(l),\kappa}^d$ Square of voltage magnitude at the node at the top of branch l .

$z_l = r_l + jx_l$ Impedance of branch l .

Symbols of prediction-interval computation

α Confidence level.

ϕ Forgetting factor.

$(P^{\downarrow\alpha}, P^{\uparrow\alpha})$ Lower and upper bound of power forecast.

L Number of clusters.

P_i Power measurement at time i .

T_ϕ Forgetting time constant.

$c(\cdot)$ Classification function.

l Label of cluster.

\mathcal{G}_i^l Normalized histogram of cluster l of historical power measurements until time i .

\mathcal{H}_i^l Normalized histogram of cluster l of historical power differentials until time i .

\times Domain of power presumption.

1 Introduction

1.1 Motivation

In traditional bulk power systems, electricity is supplied by large-scale producers to consumers, the latter having mainly a passive role. However, as electricity generation becomes more distributed, thanks to the vast adoption of renewables, more individuals and communities have an active role in electricity generation and, eventually, in electricity markets. The term “prosumer” has been coined to describe such individuals who can generate electricity locally using distributed generation. Active distribution networks (ADNs) [5] and microgrids [6] are prominent solutions that emerged to manage the supply and demand equilibrium optimally. ADNs comprise low-voltage (LV) or medium-voltage (MV) electrical grids with systems in place to control a combination of distributed energy resources (DERs), such as generators, loads, and energy storage systems (ESSs). The market participants can share ESSs to synchronize the supply with the demand and respond to variations in electricity prices to maximize their profits and the system’s overall welfare.

At the same time, by using appropriate control strategies, the distribution system operators (DSO) are called to optimally control supply and demand to satisfy their grid’s operational constraints. The existing literature has proposed to structure the control of the DERs in two phases. In the first phase, a scheduling layer computes a dispatch plan that optimizes economic-related objectives over a long horizon (e.g., 24 hours) using forecasts of the stochastic energy resources. In the second phase, a real-time (RT) control framework computes the optimal power setpoints for the DERs to track the decisions made by the scheduling layer and ensure that the grid’s operational constraints are satisfied, accounting for errors in the forecasts.

We identify two problems that have not been adequately addressed in the state-of-the-art of RT control. The first one relates to the design of the optimization problem to be solved by the RT control. As more individuals can own controllable assets, the DSO should ensure they are controlled fairly. Even though fairness has been predominantly a market-related term, the concept can be extended to RT control. For example, when the grid is controlled by battery

Chapter 1. Introduction

energy storage systems (BESSs) owned by different individuals, fairness means that their states of charge (SoC) should be as close as possible. In RT control frameworks proposed in the literature, the degree of fairness can be typically controlled by carefully tuning the weights of the optimization objectives until a satisfactory solution is found. However, this approach is not viable for various reasons. First, this method only evaluates fairness ex-post after observing the result of the grid's operation. Moreover, in a practical scenario, the DSO would have to perform extensive simulations to find an optimal set of weights. Furthermore, the optimal weights depend on the configuration and the topology, and finding a set of universal weights might be impossible. Therefore, the controller's objectives must be properly designed, and the weights must be computed automatically to adapt to the topology and the scenario.

The second problem we identify is the lack of literature concerning the ultra-short-term forecasting of electrical prosumption.¹ Because of the high penetration and volatility of renewable energy resources, accurate forecasting that matches the rate of change of these resources is needed to ensure that the regulations with respect to voltage and ampacity limits violations are satisfied. As will be explained in the following chapter, the state of the art in electricity forecasting is inadequate for the needs of RT ADN control, as most existing methods, labeled as "short-term", target horizons in the order of 10 minutes to an hour. Further research is needed in the field of "ultra-short-term" forecasting, i.e., with horizons in the order of seconds or sub-seconds.

1.2 Structure of Thesis

The structure of the thesis is as follows:

At the beginning of Chapter 2, we provide a literature review on ADN control, focusing on the two problems that interest us: fairness and ultra-short-term forecasting. We review the different notions of fairness that have been used in the context of the electricity market and examine how these definitions can be adapted for RT control. We also provide a review of SoC balancing schemes and discuss their limitations. Then, we discuss the limitations of existing forecasting methodologies to deliver ultra-short-term predictions. In the rest of the chapter, we introduce the general form of the optimization problem to be solved by an RT control for an ADN controlled by BESSs. Then, we discuss, with the help of simulations, the issues the user can experience when configuring the controller's weights.

In Chapter 3, we propose an algorithm to compute prediction intervals of aggregated power prosumption of heterogeneous resources at ultra-short-term time resolutions. The algorithm is computationally efficient and is agnostic of the distribution of the power prosumption it is applied to. We extensively evaluate the algorithm for different types of prosumers and show that it can deliver relatively short prediction intervals with high confidence levels for time horizons of up to 10 seconds.

¹In power systems, the prosumption indicates the aggregated power provided or consumed by users that have the capability to generate electricity by means of user-owned distributed generation locally.

In Chapter 4, we revisit the problem of fairness of BESSs. To solve the issue of tuning the controller's weights, we give guidelines on how to design cost functions for various objectives of RT control. The cost functions satisfy our definition of fair control of BESSs, which has been inspired by notions of fairness commonly found in the literature. It also eliminates the need for manually tuning the controller's weights, by adapting the weights to the grid's state. The value of the method is highlighted by applying it to the scenarios of Chapter 2. We also demonstrate the applicability of the method to another work in the literature.

In Chapter 5, we validate the methods of Chapters 3 and 4 in an experimental setting. We employ our methods in two control frameworks, first in COMMELEC, which has already been published in the literature [7, 8], and then in a novel two-layer control framework. The experiments highlight the applicability of the contributions of the thesis in achieving dispatching and fair control of BESSs.

Finally, Chapter 6 summarizes the thesis findings.

2 Real-Time Control of Active Distribution Networks

2.1 State of the Art

We start this chapter by reviewing the state of the art on ADN control, focusing on fairness. First, in Section 2.1.1, we give an overview of ADNs' structure and two alternative architectures for their control. In Section 2.1.2, we introduce the two-layer control architecture used in the thesis. In Section 2.1.3, we review the different definitions of fairness that have been used in the context of electricity markets. In Section 2.1.4, we discuss how the conventional definitions of fairness can be used in RT control of BESSs and examine how the literature deals with the issue of fairness. In Section 2.1.5, we discuss the necessity of having ultra-short-term forecasts of electricity prosumption and the limitations of existing approaches. Finally, in Section 2.1.6, we discuss the contributions of this thesis compared to the state of the art.

2.1.1 Active Distribution Networks Architecture

Figures 2.1 and 2.2 show two different architectures for the control of an ADN. An ADN consists of a collection of DERs, which can be (i) generators, such as photovoltaic (PV) plants, wind turbines, and combined heat and power units, (ii) consumers such as residential, commercial, and industrial loads, and charging stations for electrical vehicles (EVs), and (iii) BESSs all interfaced with the electrical grid. In the centralized architecture of Fig. 2.1, a sensing layer estimates the state of the grid and the SoC of the BESSs, which are sent to a controller together with forecasts of the stochastic uncontrollable energy resources. The controller computes the optimal setpoints and sends them to an actuator layer to be implemented by the DERs. In the decentralized architecture of Fig. 2.2, each DER is equipped with a localized controller, which only utilizes local information about the state of the DER. In both cases, the electrical grid can exchange power flows with the main grid via the point of common coupling (PCC).

Various approaches to ADN control have been proposed in the literature, both centralized and decentralized. The choice depends on the objective of the control. In traditional bulk power systems, decentralized approaches have been mainly used for primary frequency and voltage

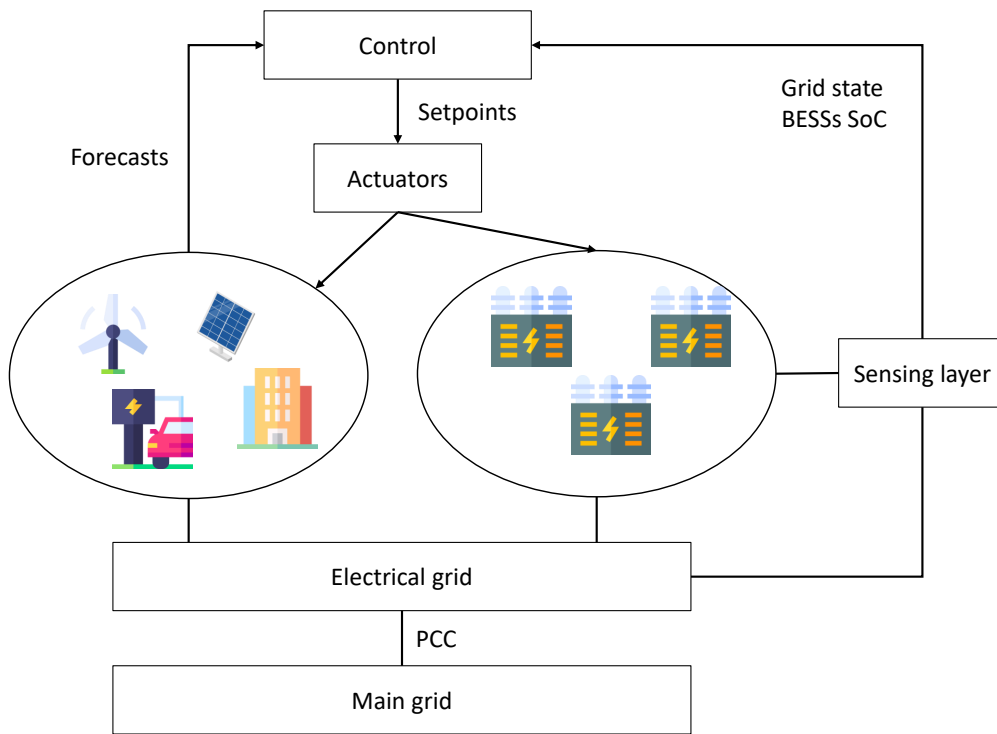


Figure 2.1: Centralized ADN architecture.

control [9]. In ADNs, these approaches are typically implemented with the use of a droop control loop (e.g., [10]), which mimics the active power-frequency and reactive power-voltage droop characteristics of synchronous generators to respond (within a few seconds) to system power imbalances. However, droop methods lack knowledge of the grid state and associated potential binding constraints; therefore, they are unsuitable for safe ADN operation.

Another category is optimization-based strategies, which can be either centralized or decentralized. These methods solve an optimization problem, either within each local controller or in a centralized controller, to compute the optimal active and reactive power setpoints for each DER based on a given objective. However, the lack of communication between DERs in the decentralized approach means that the controllers cannot achieve a global objective for the grid, for example, economic dispatching. On the other hand, the use of centralized approaches is more appealing when the control needs to account for long-term objectives, such as in the case of energy management systems (EMS) (e.g., [11]) and economic objectives, as we will see below.

2.1.2 Real-Time Control and Economic Dispatch

The traditional wholesale markets have operated on the transmission level. However, with the advent of ADNs, there has been an increasing interest in designing local electricity markets that operate at the distribution level (e.g., [12]). Fig. 2.3 shows the different electricity markets

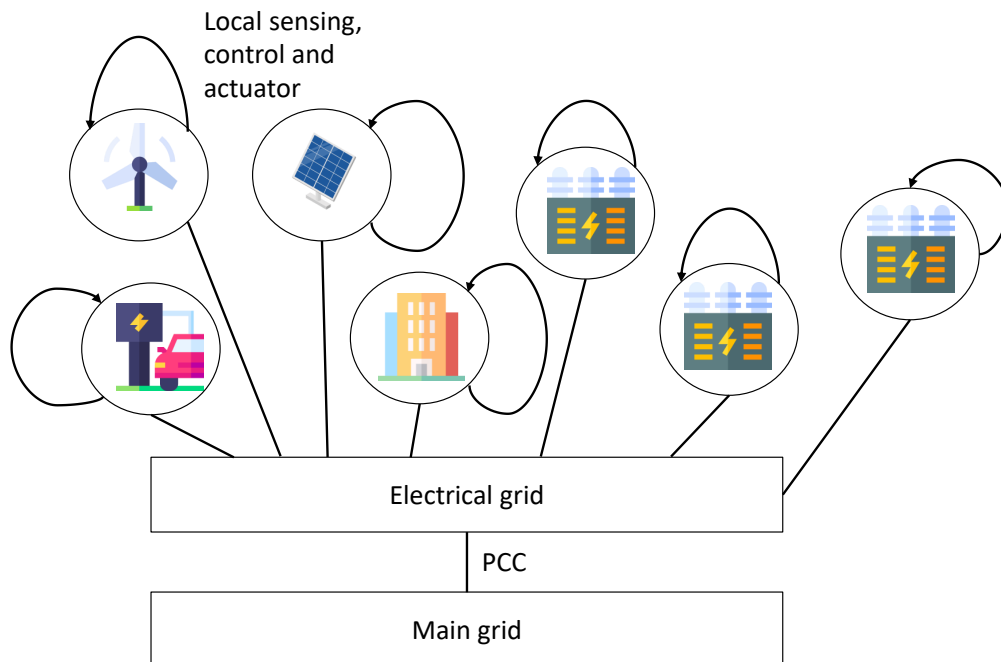


Figure 2.2: Decentralized ADN architecture.

where all the involved players can participate, along with the respective timelines [1]. Electricity can be traded among participants in the energy markets in different time frames. In the forward market, electricity is traded years or months in advance before the day of delivery. In the day-ahead market, electricity is sold via auctions usually until 12 p.m. the day before delivery, while in the intra-day and spot markets, it can be sold continuously until a given gate-closure time, e.g., one hour before delivery. Finally, the participants may make short-term trades with the system operator in the balancing market to balance the generation and demand. The purpose of the ancillary services market is to provide the necessary support to maintain the reliable power equilibrium and operation of the grid, such as ensuring adequate energy reserve and providing frequency and voltage regulation in real time.

To achieve the RT objectives of the grid and economic objectives, we can use a two-layer architecture, as has been widely used in the literature (as, for example, in [2, 13, 14, 15]). One example is shown in Fig. 2.4. We assume a centralized ADN-control architecture to participate in the day-ahead market, even though the framework can be adapted for the intra-day and balancing markets. In this case, the electricity to be exchanged between the ADN and the main grid is agreed a day-ahead for the whole day. The DSO and the other market participants are committed to tracking the agreed power profile in real-time during the day. The upper layer of the control is called the scheduling or day-ahead layer. It targets long-term energy/economic objectives and grid safety concerning nodal voltage and branch current limits by considering power forecasts for stochastic energy resources. It receives as input day-ahead scenarios of the stochastic nodal demand and generation and the SoC of the BESSs at the beginning of the day. The output of this layer is called the dispatch plan [16], which is a power profile to be tracked

Chapter 2. Real-Time Control of Active Distribution Networks

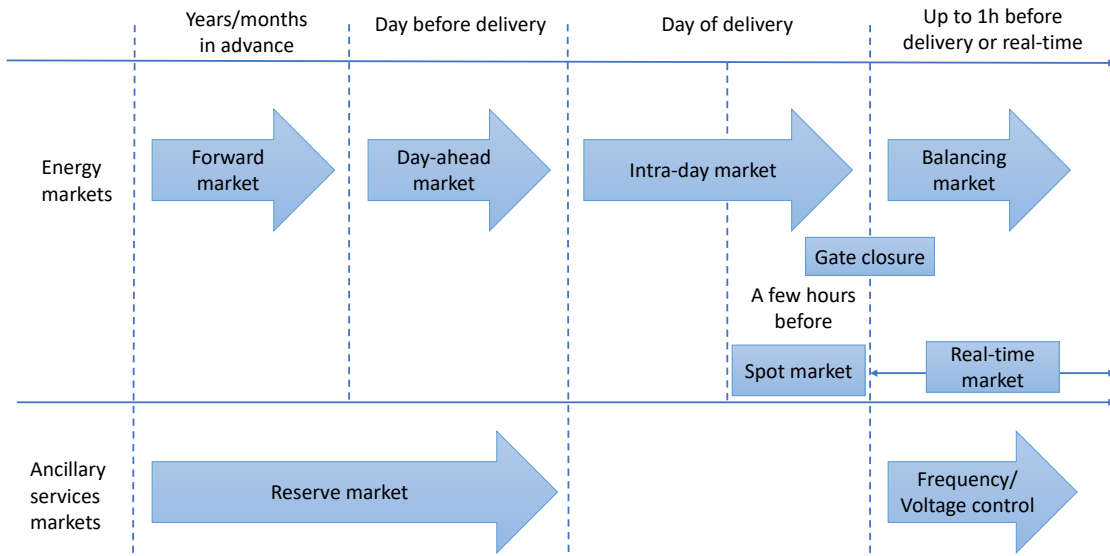


Figure 2.3: Different electricity markets and timeline (adapted from [1]).

at the PCC during the day.

The lower layer called the control layer, computes the setpoints for the controllable DERs during the day while following the decisions made by the upper layer. Because the realization of the stochastic energy resources will typically differ from the day-ahead forecasts, the decisions made by the scheduling layer for some scenarios might not be optimal or lead the system to an undesirable state concerning nodal voltages or branch currents. Therefore, the control layer should utilize updated forecasts (i.e., closer in time to the control actuation) of the stochastic resources. The control layer can consider various objectives, including: (i) tracking the dispatch plan, (ii) minimizing the reactive power exported or imported from the main grid, (iii) minimizing the grid losses, and (iv) achieving a desired SoC regulation for the BESSs (to place the state of the assets in a suitable range for future decisions). It should also satisfy the constraints of the DERs and the grid concerning nodal voltages and branch currents.

Two possible choices for the control layer are a model predictive control (MPC) (e.g., [13, 17, 18]) or a myopic control, i.e., one with a short optimization horizon (e.g., [2, 7, 14]). On the one hand, an MPC repeatedly solves an optimization problem over a long horizon (e.g., 24h) by using continuously updated, long-term forecasts and estimation of the grid state, resulting in an optimal and safe operation over a long horizon. However, because of the length of the optimization horizon, it cannot solve the problem fast enough to follow the dynamics of the stochastic resources. This means that it might be unsuitable for time-sensitive applications. On the other hand, an optimization-based control with a short horizon (e.g., a few seconds) solves a much simpler problem, which can be solved fast enough to track the stochastic presumption but fails to target long-term objectives.

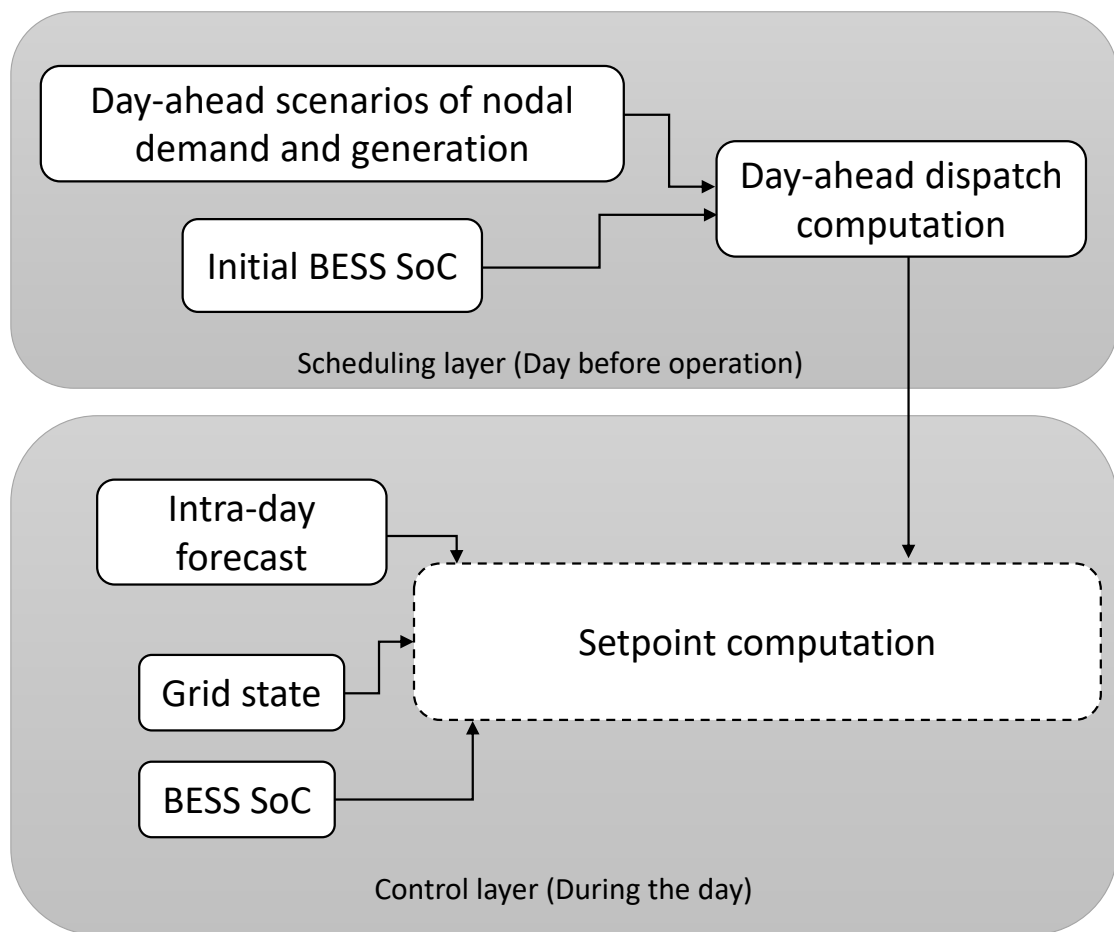


Figure 2.4: Two-layer control framework.

To exploit the benefits of the two optimization-based control approaches, we can use a combination of the two, as shown in Fig. 2.5 (as proposed in [19]). An intra-day control is executed every 5-15 minutes using updated, intra-day scenarios for the stochastic demand and generation and gives instructions to an RT control to follow updated instructions, such as an updated BESS SoC trajectory. The RT control uses short-term forecasts and RT estimation of the grid state to compute the active and reactive power setpoints of the DERs that minimize a specific objective in a short-term horizon, i.e., equal to one computation cycle.

As different individuals or companies can own the controllable DERs [20, 21] (e.g., prosumers, aggregators¹), a solution must be found to treat them fairly. Fairness has traditionally been a market-related concept, as it relates to allocating profits and costs among participants. The importance of fairness, together with the integration of local markets to the established wholesale markets, has been cited by multiple works in the literature [22, 23, 24, 25, 26]. However, in the context of RT ADN control, as defined in Fig. 2.5, the notion of fairness might need to be adapted because the economic objectives have been assigned to the scheduling

¹An actor who acts as a mediator between multiple prosumers and the market operator.

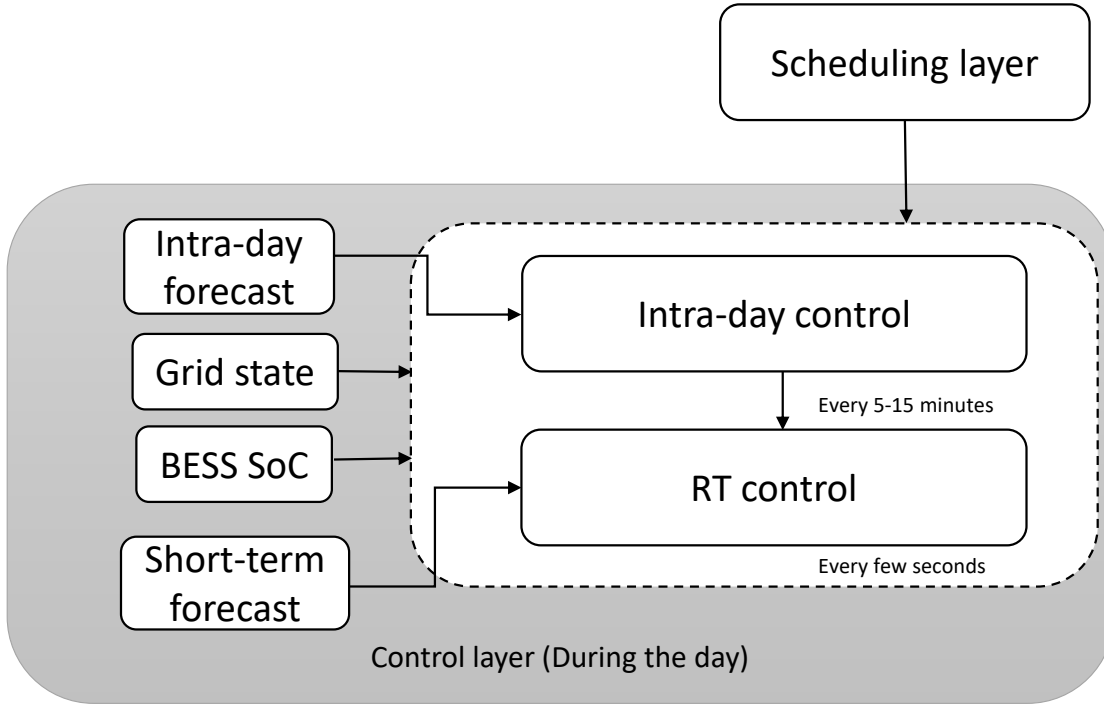


Figure 2.5: Internal details of the control layer.

layer. In the following section, we review the different fairness indicators that have been proposed in electricity markets. In Section 2.1.4, we discuss how these indicators can be adapted for a specific problem of an ADN controlled by BESSs.

2.1.3 Fairness Indicators in Electricity Markets

Regarding the problem of optimally allocating resources to electricity market participants, different fairness criteria have been proposed in the literature, as the participants can have different goals depending on the market's design. Fairness can then be evaluated ex-post using standard fairness metrics. [27] and [28] compare the values of metrics commonly used in computer networking to evaluate the fairness of a given resource allocation. These metrics are the Quality of Service (QoS), Quality of Experience (QoE), and the Min-Max indicator. QoS is typically measured by the Jain's index, defined as follows:

$$QoS = \frac{(\sum_{i=1}^N |x_i|)^2}{N \sum_{i=1}^N x_i^2} \quad (2.1)$$

where x_i is the prosumption allocated to prosumer i^2 and N is the total number of participants. The Jain's index is maximum when all the participants are allocated the same resources. However, this metric is not ideal for local electricity markets, because it assumes that all users

²In computer networks, x_i indicates the data-rate allocated to a flow.

have the same generation and demand. On the other hand, the QoE is defined based on the price of electricity perceived. Given the price α_i that each participant perceives, the QoE is defined as follows:

$$QoE = 1 - \frac{\sigma}{\sigma_{max}} \quad (2.2)$$

where

$$\sigma = \sqrt{\frac{1}{N-1} \sum_{i=1}^N (\alpha_i - \bar{\alpha})^2} \quad (2.3)$$

is the sample standard deviation of electricity prices and σ_{max} is the maximum price deviation defined by:

$$\sigma_{max} = \alpha_{imp} - \alpha_{exp} \quad (2.4)$$

where α_{imp} and α_{exp} are the prices of imported and exported energy respectively. The indicator is maximum when all participants experience the same price. The Min-Max indicator is defined as:

$$MiM = \frac{\min_i \alpha_i}{\max_i \alpha_i} \quad (2.5)$$

which again takes the maximum value when all participants perceive the same price. According to the findings of [27] and [28], these metrics yield vastly different evaluations of the degree of fairness for the same allocation. In case there are multiple objectives in the resource allocation, the values of the metrics are also affected by the choice of the objectives' weights, as is demonstrated in [28].

The problem of weight choice is also encountered in [29]. The authors address the issue of "spatial fairness", which is important when considering prosumers in different positions in a grid. In an AC grid, different nodes can have a different effect on the grid's operational constraints. For example, prosumers placed further from the feeder might experience more frequent curtailments than those placed closer because the former have a higher effect on the grid's voltages. Therefore, there might be issues of fairness concerning the position of the prosumer in the grid. The authors of [29] tackle this issue by proposing a control framework that incorporates Jain's index in the optimization problem and accounts for the AC grid model. However, there is a trade-off between Jain's index and welfare maximization, which is controlled by a weight factor. This means that the interpretation of the metrics' values might be ambiguous as they depend on the choice of weight. Therefore, proper fairness criteria must be used for the energy allocation problem to avoid ambiguities.

The works in [30, 31, 32] use fairness criteria inspired by computer networking. The authors of [30] also address the problem of spatial fairness. In particular, they consider the problem of curtailing PVs at different positions in the grid for voltage control. However, instead of using weights, fair curtailment is achieved by choosing proper logarithmic cost functions according to the proportional fairness criterion from computer networking. [31] also addresses the problem of PV curtailment and compares different fairness criteria, such as egalitarian curtailment and curtailment proportional to the maximum PV generation. Finally, [32] uses

Chapter 2. Real-Time Control of Active Distribution Networks

weighted proportional fairness to provide voltage control. The inverter's capacity is used as the weighting factor to ensure that the contribution of each prosumer to the voltage control is proportional to the prosumer's capabilities.

The works presented in [33, 34, 35] exploit concepts from game theory. Two types of games have been defined: cooperative, where participants can form coalitions to achieve a common goal, and non-cooperative, where coalitions are not allowed or desired. Cooperative games are more appealing for ADNs and microgrids, as the participants can benefit from the cooperation to increase both their individual profits and those of the whole community [33]. The participants can share ESSs to respond to electricity price variations, as is done in [34]. When ESSs are shared, the installment's capital cost and the benefits obtained from it must be shared fairly among participants. The allocation of costs is fair if all participants are satisfied and have no motivation to abstain from the cooperation. A similar game-theoretic approach is followed in [35], where fairness is ensured by sharing the total profits among the participants in proportion to the amount of energy they contribute. The costs of power losses and battery degradation are also considered with appropriate cost functions.

[36] and [37] define fairness utilizing the Shapley Value, which has been extensively used in game theory. The Shapley Value measures each participant's contribution, determined by the profit or loss incurred in the system if the participant is removed. However, the computation of the Shapley Value is generally intractable, but it can be approximated or estimated with learning methods as in [37]. [36] proposes a two-phase framework for participation in the day-ahead market. In the first phase, each prosumer optimizes their own consumption to maximize their profits. In the second phase, the aggregator coordinates the decisions of the prosumers and offers them incentives to reduce their consumption. The incentives offered are proportional to the curtailment sustained after the coordination, ensuring fairness.

Finally, apart from networking and game theory, various other notions of fairness have been proposed in electricity markets. These approaches do not differ substantially from those already discussed, as they rely on the notion of proportionality. For example, in [38], the payoffs from electricity trading are distributed among participants in proportion to the risk they are willing to take. [39, 40, 41] use a notion of priority to assign costs to different prosumers. In [39], different types of prosumers are assigned costs depending on the importance of the deviation from their personal goal. For example, the cost of PV curtailment is given a higher cost (higher priority) than the cost of flexible-load alteration. However, it is not obvious how the costs for different prosumers should be chosen. The same authors quantify the value of flexibility in [40], which is considered to be equal to the value of the grid reinforcement it replaces. The value of each flexible resource is computed in proportion to the resources' flexibility. [41] defines priority factors for energy traded among microgrids. The priority of each microgrid considers the energy requested by it and its consumption history. The importance of priority in the energy allocation is controlled by a user-defined weight. This creates again ambiguous results, as explained above.

2.1.4 Fairness in Real-Time Control of Battery Energy Storage Systems

Since in the framework of Fig. 2.5 monetary objectives are taken care of by the day-ahead layer, the criteria of fairness presented in Section 2.1.3 need to be adapted within the context of an RT control. One case of particular interest is when the control of the grid is provided by BESSs, as they are reliable and highly controllable energy sources that can balance the uncertainties of renewables and reduce the needed power reserve [16]. In this context, fairness consists in assessing the way the SoCs of the BESSs are evolving. Assuming that the BESSs provide an energy reserve for dispatching, the DSO should ensure that their SoCs (relative to their energy capacity) are balanced throughout the day. For example, if the BESSs are owned by different individuals, SoC balancing is a fair control scheme because it ensures that no BESS is used more than the others, so they are all degraded at the same rate. This definition is quite similar to the notion of proportionality used in the state-of-the-art market design, as the contribution of each BESS should be proportional to their energy reserve to achieve SoC balancing. In addition to reasons of fairness, SoC balancing is a desirable property because (i) it offers additional protection of the BESS against overcharging or over-discharging and (ii) it keeps the total power capacity³ of the system always at the maximum [42].

However, perfect SoC balancing might not be achievable when the grid's or the DERs' constraints are binding. Moreover, imposing an additional constraint on SoC fairness might compromise other grid objectives, such as dispatching. Therefore, the RT control needs to be designed properly to achieve a balance between optimality and fairness. Ideally, the design should not involve tuning weights manually to avoid any ambiguities in interpreting the results. In what follows, we present a literature review on control methods used for SoC balancing and list the limitations of these methods concerning dispatching and binding constraints.

Various SoC balancing schemes have been proposed in the literature. The works in [43, 44, 45] achieve BESS SoC balancing with droop controllers. In particular, the droop coefficients are modified using information on the SoC of the BESSs. However, droop methods do not consider the grid's binding constraints, as already explained in Section 2.1.1. The works in [42, 46, 47, 48, 49] use consensus algorithms so that all SoCs in the system converge to the average state. However, [46, 47] do not consider dispatching and use droop controllers for the power regulation regardless. On the other hand, even though [42, 48, 49] consider dispatching, they ignore grid losses, voltage constraints, and line congestions.

[18, 50, 51, 52, 53, 54, 55] all propose optimization-based strategies for dispatching ADNs with multiple BESSs. Most of them, however, [18, 50, 51, 52, 53] do not consider SoC balancing in the objective function. In addition, even though [52] and [53] consider the degradation of the BESSs, it is either not handled fairly, or the degree of fairness depends on user-defined parameters. A plausible reason why fairness is not considered is that these works implicitly assume that all the assets are owned by the same entity.

³By power capacity, we mean the maximum apparent power that can be produced or absorbed by the BESSs.

Chapter 2. Real-Time Control of Active Distribution Networks

On the other hand, [54] achieves SoC balancing by minimizing the differences between the different SoCs, but it does not consider other objectives, such as voltage regulation. Finally, [55] considers a fair load-sharing among the BESSs in proportion to their rated power, in addition to voltage and frequency control. However, the objective of load-sharing is weighed by a user-defined parameter, the choice of which is not justified. This means that a sub-optimal choice might not guarantee fair load-sharing.

This work in [55] is an example of what will henceforth be referred to as an “oracle-based approach”. A common approach to configure the control parameters relies on the use of an “oracle” that finds the optimal set of parameters a posteriori so that acceptable performance is achieved. In other words, multiple simulations are run with different sets of weights until a satisfactory set is found. Even though this approach might work when a single scenario is considered, it might not be viable in a real-life scenario because the optimal sets of weights are most likely grid and scenario-dependent. A DSO might have to configure multiple grids; hence, they would likely have to perform an extensive series of simulations to determine the optimal set of parameters for each one. Furthermore, in case there is a change in the topology of a grid, the specifications of any asset are modified, or the boundary operating conditions are changing, the set of parameters might no longer achieve the desired performance, so the whole process would most likely have to be repeated anew.

The use of this approach can be inferred in various works in the literature. The works presented in [56, 57, 58] optimize SoC-related penalties in addition to the monetary cost of power generation. The cost functions used employ certain coefficients, which were chosen manually for the problem at hand, hence the problem definition does not generalize easily to other cases. A similar approach is followed in [59]. The authors define a cost function for energy storage units, which penalizes the charging/discharging of the unit. They use a multi-agent approach to satisfy all single-device goals as much as possible; they also follow a central message to meet a proposed demand. However, it is not clear how the cost functions used in the simulations are designed. The issue of objective weighing is also addressed, but the choice of the weights does not seem straightforward.

The work presented in [2] is more closely related to the problems studied in our work, as it employs a two-layer approach. It incorporates a day-ahead scheduler that computes a power profile to be followed by the intra-day scheduler while minimizing voltage deviation and power losses. The authors present a case study that examines the effect of the weights of the respective objectives, but no intuition is given behind the choice of the values. Finally, in [7, 60], each resource is assigned a penalty term on its active and reactive power; there is also an objective to follow a target state in the grid. However, the problem formulation includes certain weights in the objective, the choice of which is not specified.

The common problem with these methods is that there is no formal way to define cost functions or choose their weights. Having no explicit guidelines for designing the cost functions in the RT layer might lead to an unfair usage of the BESSs in favor of a certain objective. This

problem will be extensively addressed in this thesis. Our contributions with respect to this problem will be summarized in Section 2.1.6.

In the thesis, we only focus on the problem of controlling an ADN with BESSs. This choice was made because we assume that all economic objectives are incorporated in the dispatch plan and that the only purpose of the control layer is to track the aggregated dispatch plan. Moreover, the BESSs are assumed to be used only to follow a common objective and they do not have a personal economic objective, for example, by participating in the market. If, on the other hand, we considered other controllable resources, their economic objectives would need to be considered, so different notions of fairness other than SoC balancing would need to be studied. We leave the study of such cases for future research.

2.1.5 Ultra-Short-Term Electricity Forecasting

In addition to the fairness problem among BESSs, we identify another problem of RT controls that the state of the art has not adequately addressed: the forecasting of power prosumption in the ultra-short term (second to sub-second scales). Forecasting of power prosumption, coupled with an appropriate RT control, is essential to ensure the safe operation of the grid and the optimal usage of the hosted resources.

Due to the low level of aggregation, the ADN requirements for electrical-power prosumption forecasting are different than for conventional large interconnected grids. In particular, when decreasing the aggregation level and measurements sampling time, the power-prosumption volatility and noise level become prominent because consumer behaviors tend not to cancel out [61], making the forecasting particularly challenging.

There are many cases where short-term forecasting is required. One example relates to the possible violation of the ampacity rating of transformers, power converters, and lines due to sudden prosumption changes associated with prosumers' highly stochastic nature. A significant change in the prosumers' renewable-power generation, or a spike in load, can create power-flow variations that can exceed the rating of transformers. Whereas, a spike in current could cause the line relays to trip. This example is particularly relevant in the presence of PVs and EV charging stations (EVCS) in the grid (e.g., [62]). The former can exhibit power variations of even 60% of their capacity in under a second [63], whereas the latter can cause significant load changes of hundreds of kW within a few seconds [64].

Even faster decisions are needed when a microgrid needs to switch to operating as a standalone system. In certain cases, microgrids might need to operate islanded, i.e., disconnected from the main grid, to enhance the resiliency of the supply to the local load. The islanding maneuver (i.e., the operation sequence for bringing a microgrid from connected to off-grid) needs to be performed by a myopic control which utilizes predictions over a short horizon in the range of the fundamental frequency period (e.g., 20 ms for a 50 Hz system) to prevent steering the system to an undesirable state. This can be achieved, for example, by correctly setting the

Chapter 2. Real-Time Control of Active Distribution Networks

gains of the slack resource droop control (e.g., [65]).

A third example, which is of high importance both in distribution and transmission networks, is that of voltage sags [66, 67]. Voltage sags are defined as a sudden reduction of the voltage between 90% and 10% of the nominal value and can last from 10 ms up to 1 minute. They are caused primarily by power-system faults, such as short circuits, or by the start-up of large motors and can cause system outages if not treated in time. For distribution systems, where voltage sags typically last between 90-2000 ms [68], in order to mitigate the voltage drop, a control framework equipped with a forecasting tool acting in the sub-second range could have a timely reaction to the voltage sag by injecting an optimally computed active/reactive power into the grid.

As ultra-short-term power-prosumption forecasts are actionable for fundamental decisions in the context of ADN/microgrid operation and their RT control, we note that well-established forecasting methodologies (e.g., developed using several techniques, such as regression-based model, artificial neural network (ANN) [69, 70, 71, 72, 73, 74, 75, 76]) are not suited for this purpose because, besides referring to point predictions, they were developed considering a high level of aggregation and forecasting horizon from 15 minutes and up. Even though ANN-based algorithms could be used for computing prediction intervals (PIs) at shorter time scales, to the best of our knowledge, there is no work using these methods to deliver forecasts in faster resolutions. Moreover, in certain applications, such as robust optimization (e.g., [77]), worst-case analysis is required; therefore, PIs instead of point predictions are desirable.

When using parametric point predictors (such as autoregressive integrated moving average (ARIMA) models), we can determine the PIs by estimating the variance of the model residuals and computing the quantiles for the prescribed confidence level. This procedure can be performed under the hypothesis of Gaussian *iid* (independent and identically distributed) model residuals. Moreover, it is reasonable to assume that for ultra-short-term horizons and low aggregation level, the forecast distribution will change model over time. Therefore, the adoption of a parametric forecasting model may be inappropriate. In cases where these hypothesis does not hold, non-parametric methods could be considered. For example, in order to determine the PIs of the power output of a wind farm, the authors of [78] apply quantile regression to characterize the historical residuals of a state-of-the-art point-prediction model.

The same concept, but developed using fuzzy inference instead of quantile regression, is described in [79]. As far as forecasting the electrical-power prosumption is concerned, non-parametric methods have been proposed in [80] and [81]. In the former work, an ANN with an empirically chosen number of layers was trained using historical data to provide a 30-minute-ahead PI for a given confidence level according to the values of selected data features. The latter work is concerned with predicting the minimum and maximum bounds of the power consumption by applying empirical-mode decomposition and support-vector regression to an interval-valued time signal obtained from a one-hour historical sample of power consumption. Both methods target a prediction horizon that is too long for the

requirements of RT ADN/microgrid operation.

2.1.6 Contributions to the State of the Art

Our contributions compared to the state of the art are the following:

- In Chapter 3, we propose a non-parametric method for delivering ultra-short-term prediction intervals of heterogeneous prosumers in ADNs. The method empirically learns the CDF (Cumulative Distribution Function) of the prosumption, bypassing the problems tied with parametric methods. It also continuously updates the CDF as new measurements become available.
- In Chapter 4, we give guidelines to the design of cost functions for various objectives related to the RT control of ADNs. Our method reduces the time and effort needed to configure the parameters of the controller and gives some intuition on how it will perform a priori without the need to run an extended series of simulations. It also has the advantage of being grid and scenario-independent. This means that DSOs can employ it without any modifications. The choice of the respective cost functions is made so that the control tries to keep the SoC trajectories of the BESSs close to each other while following the grid's objectives and satisfying its constraints.
- In Chapter 5, we experimentally validate two control frameworks that employ the methods of the other two chapters to achieve dispatching and fair control of BESSs.

In the rest of this chapter, we give a general formulation of the optimization problem targeted by an RT control for controlling BESSs. We also give further insight into the problems with the oracle-based approach via simulations.

2.2 Real-Time Control Problem Formulation

2.2.1 Optimization Problem

We assume the centralized control architecture of an ADN shown in Fig. 2.1. The ADN is controlled by a two-layer control framework as the one introduced in Fig. 2.5. In this thesis, we assume a given scheduling layer and focus on the design of the control layer, comprised of the RT and intra-day controls. The design is done bottom-up, i.e., starting with the RT control. In the rest of this section, we study the problems that arise when designing the optimization problem to be solved by the RT control. A possible design of the intra-day control will be proposed in Chapter 5.

To bridge the gap from the state-of-the-art concerning the control of BESSs, we assume that the controllability of the ADN is provided exclusively by BESSs, whereas the rest of the energy resources are uncontrollable stochastic renewable generators and loads. We consider

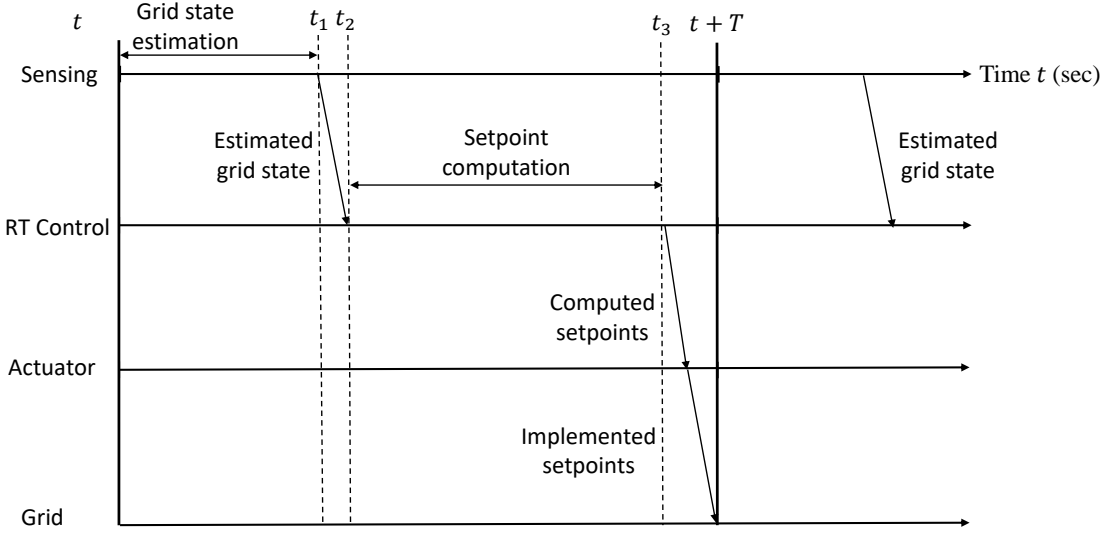


Figure 2.6: Interaction between sensing, actuating, and RT control layers.

an ADN connected to the main grid to be controlled by N_B BESSs that can implement any active/reactive power setpoint $\mathbf{x}_i = (P_i, Q_i) \in \mathcal{A}_i, i = 1, \dots, N_B$, where \mathcal{A}_i is the constraint set of BESS i . The grid also consists of U stochastic, uncontrollable energy resources of uncertain prosumption $\mathbf{u}_n = (\mathcal{P}_n, \mathcal{Q}_n), n = 1, \dots, U$.

The interaction between the sensing, RT control, and actuator layers is shown in Fig. 2.6. At time t , the computation cycle for the optimal setpoints at time $t + T$ starts, where T is the period of the control in seconds. At time t , the sensing layer starts estimating the state of the grid, which finishes at time t_1 . At time t_2 , the control layer starts computing the optimal setpoints for the BESSs by using the grid state and the SoC of each BESS estimated at t_1 , and the forecasts of the prosumptions \mathbf{u}_n for $t + T$. The computation finishes at time t_3 , and the setpoints are sent to the actuator layer for implementation (time $t + T$). Then, the sensing layer initiates again the state estimation and the cycle continues.

The optimal setpoints are computed by solving an optimization problem. Each BESS has a cost function, called *battery objective*, related to it; it indicates its preference to implement a specific point within its constraint set. We indicate with $C_i(\mathbf{x}_i | S_i, SoC_i)$ the cost function of BESS i , where SoC_i is its SoC and S_i is the rated apparent power of its power-electronic converter⁴. In addition to the individual battery objectives, the controller should aim to achieve a target grid state. For example, it should achieve a target power at the PCC, minimize the reactive power exchange with the main grid or minimize the grid losses. We call this the *grid objective*, denoted as $J(\mathbf{x} | \mathbf{u})$, where $\mathbf{x} = (\mathbf{x}_1, \mathbf{x}_2, \dots, \mathbf{x}_{N_B})$ is the set of BESS setpoints and $\mathbf{u} = (\mathbf{u}_1, \mathbf{u}_2, \dots, \mathbf{u}_U)$ is the set of the stochastic power injections.

At every time step t , the controller's objective is to minimize the total forecast cost for $t + T$,

⁴In this work, we assume that the single purpose of a BESS is to provide an energy reserve for dispatching; hence the SoC is the only parameter of the BESS that is reflected in its cost function.

2.2 Real-Time Control Problem Formulation

subject to the BESSs' constraints⁵.

$$\begin{aligned} & \min_{\mathbf{x}} C_{tot}(\mathbf{x}|\hat{\mathbf{u}}) \\ & s.t. \mathbf{x}_i \in \mathcal{A}_i, i = 1, \dots, N_B \\ & \text{and power flow equations} \end{aligned} \quad (2.6)$$

$$C_{tot}(\mathbf{x}|\mathbf{u}) = \sum_{i=1}^{N_B} C_i(\mathbf{x}_i|S_i, SoC_i) + J(\mathbf{x}|\mathbf{u}) \quad (2.7)$$

where $\{\hat{\cdot}\}$ denotes the forecast of the prosumption for $t + T$. In this formulation, hard grid constraints concerning nodal-voltage deviations, ampacity limits, or power factors can be relaxed to soft constraints and be expressed via appropriate cost functions [82], as shown in Section 2.3. There are two reasons why we decided to use only soft constraints. First, soft constraints reduce the computational complexity of the problem, so it is more likely that it meets the strict time constraints required by certain RT applications (see the discussion in Section 2.1.5). Moreover, soft constraints for the nodal voltages and the branch currents (see Sections 2.3.3 and 2.3.4) penalize the respective values before they hit their limit. This feature gives the control a more robust behavior against fluctuations in the power of stochastic energy resources, as it is more likely that the grid constraints will be satisfied between two computational cycles.

2.2.2 Convexity of the Problem

Because specific applications require fast decisions (within a few seconds or sub-second), the optimization problem of the RT control should be solved efficiently; hence, it should be preferably convex. Concerning the convexity of Problem (2.6), the cost functions of the batteries and their respective constraint sets can easily be designed to be convex.

Regarding the grid objective, we consider that we want to optimize the value of M grid variables $\mathbf{y} = (y_1, y_2, \dots, y_M)$, where y_m can represent a specific nodal injection, nodal voltage, or branch current. For this purpose, we consider grid cost-functions of the following form:

$$J(\mathbf{x}|\mathbf{u}) = \sum_{m=1}^M w_{y_m} J_m(y_m(\mathbf{x}|\mathbf{u})) \quad (2.8)$$

where J_m is the penalty term for the grid variable y_m and $w_{y_m} > 0$ is the respective weight.

The power-flow equations link the complex power injections with the nodal voltages in the following way [83]:

$$\bar{S}_k = \bar{E}_k \sum_{k'=1}^K \underline{Y}_{kk'} \underline{E}_{k'} \quad (2.9)$$

⁵Because the problem is solved over one time step, we omit the time index t in the notation of this section.

Chapter 2. Real-Time Control of Active Distribution Networks

where K is the number of buses in the grid, \bar{E}_k, \bar{S}_k denote the complex voltage and power injection of bus k , \bar{Y} is the nodal admittance matrix and $\{\cdot\}$ indicates the complex conjugate. Because of the form of Equation (2.9), the relation between voltages, currents, and active/reactive power is non-convex. One way to achieve convexity is by linearizing the power flow equations [84]. In this work, we derive a linear approximation of (2.9), using the method of *sensitivity coefficients* [83]. The sensitivity coefficients of grid variable y_m at time t with respect to a given nodal power injection (P, Q) are defined as follows:

$$\begin{aligned} K_P^m(t) &= \frac{\partial y_m}{\partial P}(\mathbf{x}(t-1)|\mathbf{u}(t-1)) \\ K_Q^m(t) &= \frac{\partial y_m}{\partial Q}(\mathbf{x}(t-1)|\mathbf{u}(t-1)) \end{aligned} \quad (2.10)$$

where $\mathbf{x}(t-1)$ and $\mathbf{u}(t-1)$ are the values of the BESS setpoints and the stochastic power injections estimated at time $t-1$. The computation of the partial derivatives as a function of the grid state is given in [83]. Note that this method assumes the full observability of the grid's state to compute the sensitivity coefficients.

Using the notation presented earlier in this section, we can approximate the grid variable y_m at time t as follows:

$$\begin{aligned} y_m(\mathbf{x}|\mathbf{u}) &= y_m^0 + \sum_{i=1}^{N_B} (K_{P,i}^m(P_i - P_i^0) + K_{Q,i}^m(Q_i - Q_i^0)) + \\ &+ \sum_{n=1}^U (K_{\mathcal{P},n}^m(\mathcal{P}_n - \mathcal{P}_n^0) + K_{\mathcal{Q},n}^m(\mathcal{Q}_n - \mathcal{Q}_n^0)), m = 1, \dots, M \end{aligned} \quad (2.11)$$

where y_m^0, P_i^0 and Q_i^0 are the values of y_m, P_i and Q_i respectively at time $t-1$ and $K_{P,i}^m, K_{Q,i}^m$ are the sensitivity coefficients with respect to the BESSs setpoints. Accordingly, $\mathcal{P}_n^0, \mathcal{Q}_n^0$ are the values of the uncontrollable prosumptions at $t-1$ and $K_{\mathcal{P},n}^m, K_{\mathcal{Q},n}^m$ are the respective sensitivity coefficients. This approximation is accurate because the RT control is assumed to run every few seconds. Indeed, it has been observed that in distribution systems, the values of the sensitivities do not change dramatically if they are computed fast enough [83]. This is true under normal operating conditions, and the assumption cannot be made when there are abrupt changes in the system, like faults [3], which cannot be compensated by the control.

The convex formulation of Problem (2.6) is the following:

$$\begin{aligned} \min_{\mathbf{x}} \quad & C_{tot}(\mathbf{x}|\hat{\mathbf{u}}) \\ \text{s.t.} \quad & \mathbf{x}_i \in \mathcal{A}_i, i = 1, \dots, N_B \\ & \text{and (2.11)} \end{aligned} \quad (2.12)$$

2.3 Examples of Cost Functions

In this section, we present examples of cost functions for various objectives. These cost functions, adapted from [85], will be used in Section 2.4 to demonstrate the problem of configuring the controller parameters.

2.3.1 Battery Cost Function

We assume that the RT control receives at time t a target SoC value, SoC_i^{target} , for BESS i by either the day-ahead layer or the intra-day control. For example, the SoC target value could indicate the expected SoC at time t computed by the upper layer. The cost function proposed in [85], so that BESS i achieves this target SoC, is the following:

$$C_i(P_i, Q_i | S_i, SoC_i) = w_i \frac{|\Delta SoC_i|}{3} \left(\frac{P_i^2}{S_i^2} - 2 \operatorname{sgn}(\Delta SoC_i) \frac{P_i}{S_i} \right) \quad (2.13)$$

where $\Delta SoC_i = SoC_i - SoC_i^{target}$ is the difference between the SoC of the BESS and the target value normalized in the interval $[-1, 1]$. $w_i > 0$ is the weight placed on the objective of BESS i , which is to be configured by the user. The cost function is divided by 3 to be normalized in the interval $[-1, 1]$.

2.3.2 ADN Slack Cost Function

The primary purpose of the RT control is to track the dispatch plan computed by the scheduling layer at the slack bus. Moreover, the controller usually tries to limit the reactive power exchange with the main grid. These two objectives can be expressed with the following cost functions:

$$J_{P_s}(\mathbf{x} | \mathbf{u}) = (P_s(\mathbf{x} | \mathbf{u}) - P^{DP})^2 \quad (2.14)$$

$$J_{Q_s}(\mathbf{x} | \mathbf{u}) = Q_s^2(\mathbf{x} | \mathbf{u}) \quad (2.15)$$

where (P_s, Q_s) are the active and reactive powers at the ADN slack bus, and P^{DP} is the active power tracking value at the PCC computed by the dispatcher.

2.3.3 ADN Voltage Cost Function

In addition to dispatching, the RT control should ensure that all nodal voltages V_k are kept within a given hard tolerance β_{hard} from the nominal value V_n , as dictated by industry standards, such as the EN 50160 [86] in Europe. Unlike the slack cost, we should not use a quadratic function for this objective because we want the cost to take very large values when

$|V_k - V_n| > \beta_{hard}$. An appropriate cost function, inspired by [85], is the following:

$$J_{V_k}(\mathbf{x}|\mathbf{u}) = \begin{cases} \frac{(V_k(\mathbf{x}|\mathbf{u}) - V_{nom})^2}{\beta_{hard}^2 - (V_k(\mathbf{x}|\mathbf{u}) - V_{nom})^2} & |V_k - V_{nom}| \leq \beta_{hard} - \epsilon \\ a_V(V_k(\mathbf{x}|\mathbf{u}) - V_{nom})^2 + b_V(V_k(\mathbf{x}|\mathbf{u}) - V_{nom}) & V_k - V_{nom} > \beta_{hard} - \epsilon \\ a_V(V_k(\mathbf{x}|\mathbf{u}) - V_{nom})^2 - b_V(V_k(\mathbf{x}|\mathbf{u}) - V_{nom}) & V_k - V_{nom} < -(\beta_{hard} - \epsilon) \end{cases} \quad (2.16)$$

where $0 < \epsilon \ll \beta_{hard}$ is a constant that prevents the function from taking infinite values when approaching the hard constraint. The values of a_V and b_V are computed such that $J_V(V_k)$ and its derivative $J'_V(V_k)$ are both continuous at $V_k = V_{nom} \pm (\beta_{hard} - \epsilon)$. The function is drawn in Fig. 2.7 for $\beta_{hard} = 0.05\text{pu}$ and $\epsilon = 10^{-3}$. The benefits of this function are that (i) it is convex, (ii) it is continuous and differentiable everywhere, and (iii) it takes very large values as the voltage approaches or exceeds the hard constraint.

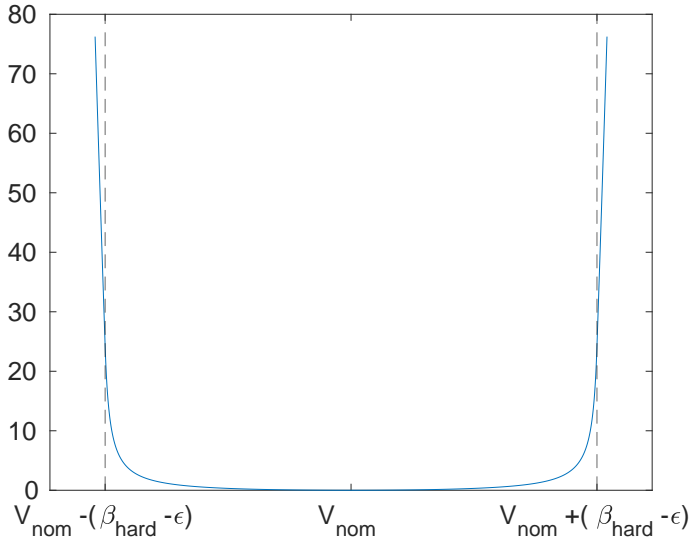


Figure 2.7: Voltage cost function.

2.3.4 ADN Branch Current Cost Function

In addition to voltage regulation, the control should satisfy strict thermal constraints in the branches. These constraints, which are dictated again by industry standards, such as the IEC 60287 [87], are usually expressed by a maximum current flow in branch l , I_l^{max} , called the ampacity of the branch. Unlike the voltage magnitudes, however, the magnitude of the branch current cannot be accurately approximated as a linear function of nodal powers in a large power range. Instead, a better choice would be to use a linear approximation for the complex current phasor \bar{I}_l , as in [88]. Because, in the end, we need to construct real cost functions, we can approximate the constraint

$$|\bar{I}_l| = \sqrt{(\Re(\bar{I}_l))^2 + \Im((\bar{I}_l))^2} \leq I_l^{max} \quad (2.17)$$

2.4 Configuring the Weights of the Controller

where $\Re(\cdot)$, $\Im(\cdot)$ indicate the real and imaginary part, using the following two constraints

$$\begin{aligned} -I_l^{max} &\leq I_l^+ \leq I_l^{max} \\ -I_l^{max} &\leq I_l^- \leq I_l^{max} \end{aligned} \quad (2.18)$$

where $I_l^+ = \frac{\Re(\bar{I}_l) + \Im(\bar{I}_l)}{\sqrt{2}}$ and $I_l^- = \frac{\Re(\bar{I}_l) - \Im(\bar{I}_l)}{\sqrt{2}}$. We can then represent Constraints (2.18) using two penalty terms per line, with a cost function inspired again by [85]:

$$J_{I_l^+}(\mathbf{x}|\mathbf{u}) = \begin{cases} \frac{(I_l^+(\mathbf{x}|\mathbf{u}))^2}{(I_l^{max})^2 - (I_l^+(\mathbf{x}|\mathbf{u}))^2} & |I_l^+| \leq (1-\epsilon)I_l^{max} \\ a_I \left(\frac{I_l^+(\mathbf{x}|\mathbf{u})}{I_l^{max}}\right)^2 + b_I \left(\frac{I_l^+(\mathbf{x}|\mathbf{u})}{I_l^{max}}\right) & I_l^+ > (1-\epsilon)I_l^{max} \\ a_I \left(\frac{I_l^+(\mathbf{x}|\mathbf{u})}{I_l^{max}}\right)^2 - b_I \left(\frac{I_l^+(\mathbf{x}|\mathbf{u})}{I_l^{max}}\right) & I_l^+ < -(1-\epsilon)I_l^{max} \end{cases} \quad (2.19)$$

$$J_{I_l^-}(\mathbf{x}|\mathbf{u}) = \begin{cases} \frac{(I_l^-(\mathbf{x}|\mathbf{u}))^2}{(I_l^{max})^2 - (I_l^-(\mathbf{x}|\mathbf{u}))^2} & |I_l^-| \leq (1-\epsilon)I_l^{max} \\ a_I \left(\frac{I_l^-(\mathbf{x}|\mathbf{u})}{I_l^{max}}\right)^2 + b_I \left(\frac{I_l^-(\mathbf{x}|\mathbf{u})}{I_l^{max}}\right) & I_l^- > (1-\epsilon)I_l^{max} \\ a_I \left(\frac{I_l^-(\mathbf{x}|\mathbf{u})}{I_l^{max}}\right)^2 - b_I \left(\frac{I_l^-(\mathbf{x}|\mathbf{u})}{I_l^{max}}\right) & I_l^- < -(1-\epsilon)I_l^{max} \end{cases} \quad (2.20)$$

The values of a_I and b_I are chosen such that $J_I(I_l^{+/-})$ and $J'_I(I_l^{+/-})$ are both continuous at $I_l^{+/-} = (1-\epsilon)I_l^{max}$. Just like the voltage function, this function is designed to take very large values as the current approaches or exceeds the ampacity of the branch.

2.3.5 Total Grid Cost Function

Given the individual cost functions defined in Sections 2.3.2-2.3.4 and the form of the generalized grid cost defined in Equation (2.8), an example for the total grid cost function is the following:

$$\begin{aligned} J(\mathbf{x}|\mathbf{u}) &= w_s(J_{P_s}(\mathbf{x}|\mathbf{u}) + J_{Q_s}(\mathbf{x}|\mathbf{u})) + \\ &+ \frac{w_V}{K} \sum_{k=1}^K J_{V_k}(\mathbf{x}|\mathbf{u}) + \frac{w_I}{L} \sum_{l=1}^L J_{I_l^+}(\mathbf{x}|\mathbf{u}) + J_{I_l^-}(\mathbf{x}|\mathbf{u}) \end{aligned} \quad (2.21)$$

where K is the number of buses, L is the number of branches and $w_s, w_V, w_I > 0$ are user-defined weights.

2.4 Configuring the Weights of the Controller

To complete the formulation of Problem (2.6), we need to choose the weights of each battery cost-function in Equation (2.13) and the weights of the individual grid cost-functions in Equation (2.21). The choice is usually not straightforward. As already discussed in Section 2.1.4, most works in the literature seem to use what we call the ‘‘oracle-based approach’’ to configure the weights. This method consists of running multiple simulations with different sets of weights until a set with a satisfactory performance is found.

Chapter 2. Real-Time Control of Active Distribution Networks

This method is impractical for the following reasons

1. It assumes that the realizations of the stochastic prosumption are known in advance (hence the name “oracle-based”).
2. It is not always clear from the simulation results why one set of weights is better than another.
3. The optimal set of weights typically depends on the system’s topology. Therefore, if one of the characteristics of the energy resources changes, the process of choosing the weights would need to be repeated.

The rest of this section uses an example to demonstrate the oracle-based approach’s problems better.

2.4.1 Simulation Setup

Topology

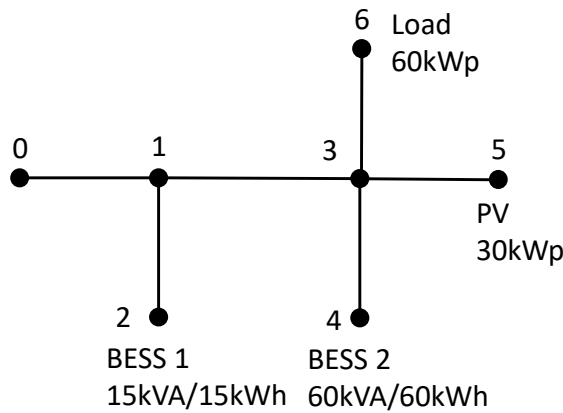


Figure 2.8: Microgrid topology. Bus 0 is the slack bus.

We consider the microgrid of Fig. 2.8. Its branch parameters are copied from the CIGRE benchmark microgrid and can be found in [89]. The topology is composed of two uncontrollable prosumers, namely a PV plant of 30 kWp and a load of 60 kWp, both of which have a power factor of 0.9. It also contains two controllable BESSs, BESS 1, rated at 15 kVA/15 kWh, and BESS 2, rated at 60 kVA/60 kWh.

We use the two-layer control approach of Fig. 2.4. To study an interesting case, we start the computation of the dispatch plan at noon, when the PV production is high. The scheduling layer receives as an input (i) the SoC of the two BESSs at the beginning of the day, which is assumed to be 0.6 for both BESSs, and (ii) two scenarios for the PV generation and load

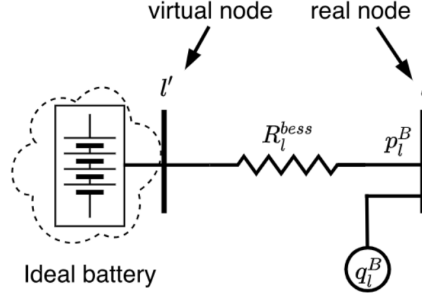


Figure 2.9: Equivalent circuit diagram of BESS

consumption at a 5-minute resolution for a horizon of 24 hours, or 288 intervals. We take all combinations of the PV and load scenarios, leading to 4 scenarios in total.

Dispatch Plan Computation

To compute the dispatch plan, we solve an optimization problem based on the simplified DistFlow approximation [90]. It constructs a convex approximation of the power flow problem by assuming that the branch power losses and the shunt elements are negligible.

The node at the top of branch l is indicated by $up(l)$, while the node at the bottom is indicated simply by l . $z_l = r_l + jx_l$ is the impedance of branch l . For every branch $l = 1, \dots, L$, scenario $d = 1, \dots, 4$, and time $\kappa = 1, \dots, 288$, we define the following quantities: $S_{l,\kappa}^d = P_{l,\kappa}^d + jQ_{l,\kappa}^d$ is the apparent power entering the branch from the top, $V_{l,\kappa}^d$ is the voltage magnitude and $s_{l,\kappa}^d = p_{l,\kappa}^d + jq_{l,\kappa}^d$ is the total power injected at bus l (including the power injected by the BESSs). \mathbf{G} denotes the adjacency matrix.

For every BESS $i = 1, \dots, N_B$ ($N_B = 2$ in this case) and for every scenario d and time κ , we define the following: $s_{i,\kappa}^{B,d} = p_{i,\kappa}^{B,d} + jq_{i,\kappa}^{B,d}$ is the power injected by the BESS into the grid⁶ and $SoC_{i,\kappa}^d$ is its SoC, normalized by its energy capacity E_i^{max}

We use the equivalent diagram of Fig. 2.9 to model the losses inside a BESS, which is inspired by [91]. Assuming a BESS at node l , we represent the losses of the BESS with a virtual branch l' with series resistance R_l^{bess} between node l and a virtual node l' . The BESS's power $s_l^B = p_l^B + jq_l^B$ is injected at bus l , while an ideal, lossless BESS is placed at bus l' .

The constraints of the problem are the following:

1. Power flow $\forall \kappa, d, l$

$$P_{l,\kappa}^d = \sum_{n:G_{ln}=1} P_{n,\kappa}^d + p_{l,\kappa}^d \quad (2.22)$$

⁶Positive power indicates discharging.

Chapter 2. Real-Time Control of Active Distribution Networks

$$Q_{l,\kappa}^d = \sum_{n:G_{ln}=1} Q_{n,\kappa}^d + q_{l,\kappa}^d \quad (2.23)$$

$$V_{l,\kappa}^d = V_{up(l),\kappa}^d - 2(r_l P_{l,\kappa}^d + x_l Q_{l,\kappa}^d) \quad (2.24)$$

2. Voltage constraints $\forall \kappa, d, l$

$$V_{up(1),\kappa} = 1 \quad (2.25)$$

$$0.95 \leq V_{l,\kappa}^d \leq 1.05 \quad (2.26)$$

3. BESS Constraints $\forall \kappa, d, i$

$$SoC_{i,1}^d = SoC_i^{initial} \quad (2.27)$$

$$SoC_{i,\kappa+1}^d = SoC_{i,\kappa}^d - \frac{T p_{i,\kappa}^{B,d}}{E_i^{max}} \quad (2.28)$$

$$0.2 \leq SoC_{i,\kappa}^d \leq 0.9 \quad (2.29)$$

$$|SoC_{i,1}^d - SoC_{i,288}^d| \leq 0.1 \quad (2.30)$$

$$p_{i,\kappa}^{B,d}, q_{i,\kappa}^{B,d} \in \left[-\frac{\sqrt{2}}{2} S_i, \frac{\sqrt{2}}{2} S_i\right] \quad (2.31)$$

where $SoC_i^{initial}$ is the measured SoC at the beginning of the day, and $T=5$ min is the time period of the dispatch plan discretization. The purpose of Constraint (2.30) is to ensure that the BESSs have enough energy at the end of the day for the following day.

The optimization problem that computes the dispatch plan, adapted from [91], is the following:

$$\min_{P_\kappa^{DP}, SoC_{i,\kappa}^d} \sum_{\kappa=1}^{288} \left\{ \sum_d \left[1000 |P_\kappa^{DP} - P_{0,\kappa}^d| + |SoC_{1,\kappa}^d - SoC_{2,\kappa}^d| \right] \right\} \quad (2.32)$$

s.t. (2.22)-(2.31)

where P_κ^{DP} is the dispatch plan at time κ and $P_{0,\kappa}^d$ is the power of the slack bus for time κ and scenario d . The first term of the cost function, with a weight of 1000, aims to compute a dispatch plan that can be tracked at the PCC as much as possible for every scenario. The second term, with a weight of 1, aims to compute a fair solution between the two BESSs.

Real-Time control

We consider the time slice 12:00-12:05 after the computation of the dispatch plan. The target SoC trajectory of the two BESSs, used in Cost Function (2.13), is equal to the median trajectory computed by the dispatcher over all scenarios. The RT control solves Problem (2.12) every 10 s, using the cost functions of Section 2.3. Because the control period is fast, i.e., similar to the system's dynamics, we can use a persistent forecaster for the presumption of the PV and the load at the next time step, as shown in Fig. 2.10.

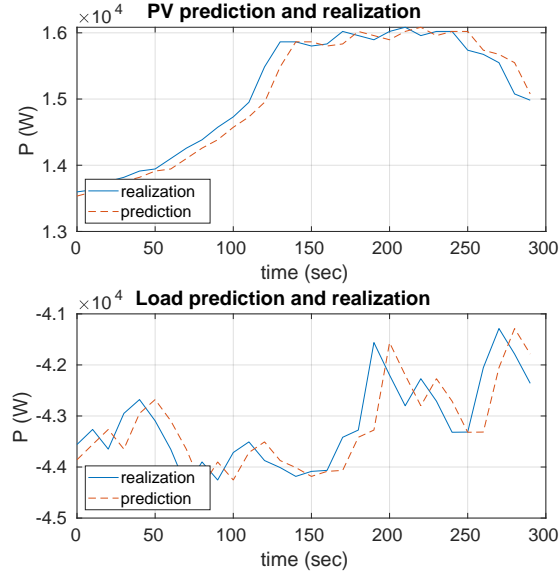


Figure 2.10: Short-term predictions and realizations of the stochastic power injections in the microgrid of Fig. 2.8.

The constraint set of the BESSs' power-electronics converters, required in Problem (2.6) is approximated by the following box constraints:

$$P_i, Q_i \in \left[-\frac{\sqrt{2}}{2} S_i, \frac{\sqrt{2}}{2} S_i\right] \quad (2.33)$$

Note that this inner-box approximation of the capability curve of a BESS is accurate, as we cannot usually exploit the full nominal power of the BESS, and the capability curve typically resembles a rectangle [92]. Finally, the hard voltage bound is $\beta_{hard} = 0.05$.

We perform a simulation in MATLAB and solve the optimization problem using the interior-point method implemented by the *fmincon* function.

2.4.2 First Scenario - The Oracle-Based Approach

As already explained, it is up to the user to properly choose the weights of the objectives. We first consider using the same weight for all objectives: $w_s = w_V = w_I = w_1 = w_2 = 1$. Looking at the simulation results shown in Fig. 2.11, we notice that the slack can neither track the dispatch plan (see active power plot) nor effectively control its reactive power (green line in the reactive power plot), even though there is enough controllability in the BESSs to do so. Indeed, the powers and SoCs of the BESSs, as well as the nodal voltages and branch currents, are all well within their respective bounds. In particular, voltage magnitudes are within 4% of the nominal value, and all currents are below 60% of the respective line ampacities. Looking at the SoC graph, we notice that the two SoCs follow a different trajectory, even though they have

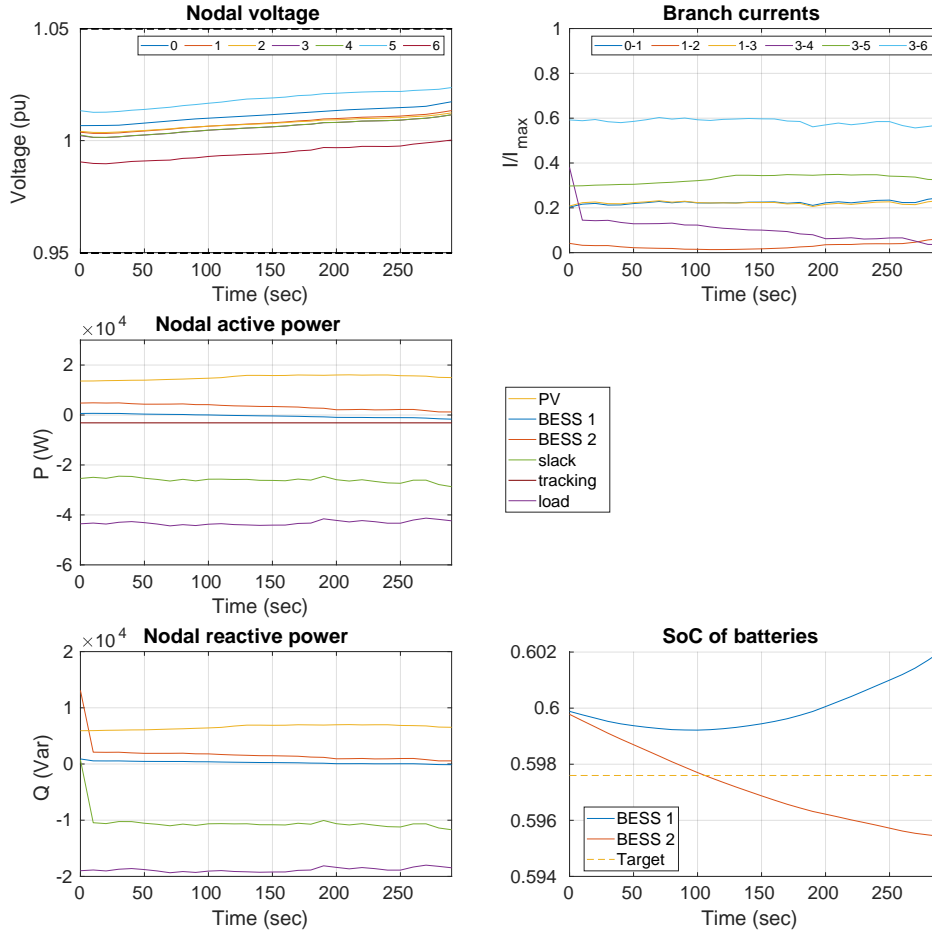


Figure 2.11: Simulation results of the first scenario with equal weights for all objectives. The bottom-right graph shows the target trajectory for the SoC of the BESSs that was computed by the dispatcher.

the same target. If we compare the achieved active power at the slack bus with the target value, we see that the BESSs should provide energy to the main grid in order to track the dispatch plan. However, BESS 1 charges, and BESS 2 does not discharge at a fast enough rate to provide the required energy. The reason is that the controller tries to overcompensate for the voltage deviations by instructing the BESSs to absorb energy. This means that the weight w_s is too small compared to the weight w_V , as we will verify next.

This simulation indicates that the chosen cost functions do not lead to a balanced satisfaction of the objectives. For the next simulation, we consider adapting the weights of the objectives, to achieve a more balanced control. The choice is made as follows: we first fix the slack weight $w_s = 1$. Then, we run simulations with varying weights for the rest of the objectives,

2.4 Configuring the Weights of the Controller

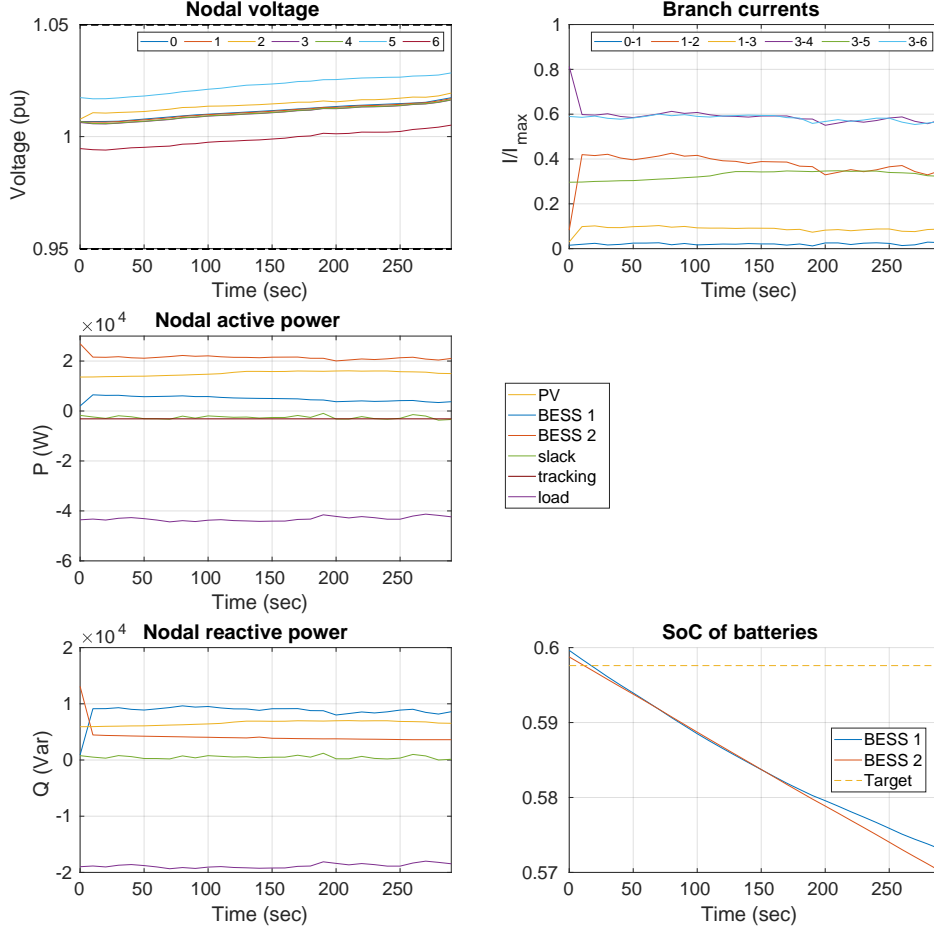


Figure 2.12: Simulation results of the first scenario with manually picked weights: slack weight $w_s = 1$, voltage weight $w_V = 10^{-6}$, current weight $w_I = 10^{-5}$, battery weights $w_1 = w_2 = 10^{-4}$

such that (i) the slack tracks the dispatch plan with acceptable accuracy, (ii) the controller's reaction to the voltage deviations is less significant, and (iii) the BESSs' SoCs follow a similar trajectory. After a series of simulations, we settle with the weights $w_s = 1$, $w_V = 10^{-6}$, $w_I = 10^{-5}$, $w_1 = w_2 = 10^{-4}$.

The simulation results are shown in Fig. 2.12. First of all, all voltages and currents are still kept within their respective bounds. However, there are certain major improvements to be observed compared to Fig. 2.11. Concerning the active power, the controller does a much better job at tracking the dispatch plan, while the reactive power injection to the external grid is kept close to 0. Regarding the SoC graph, we observe a more fair regulation between the two BESSs, as now both BESSs discharge at the same rate, to provide the required energy to the main grid. More specifically, the maximum relative deviation between the two SoC trajectories

is 0.51%, as opposed to 1.1% in Fig. 2.11.

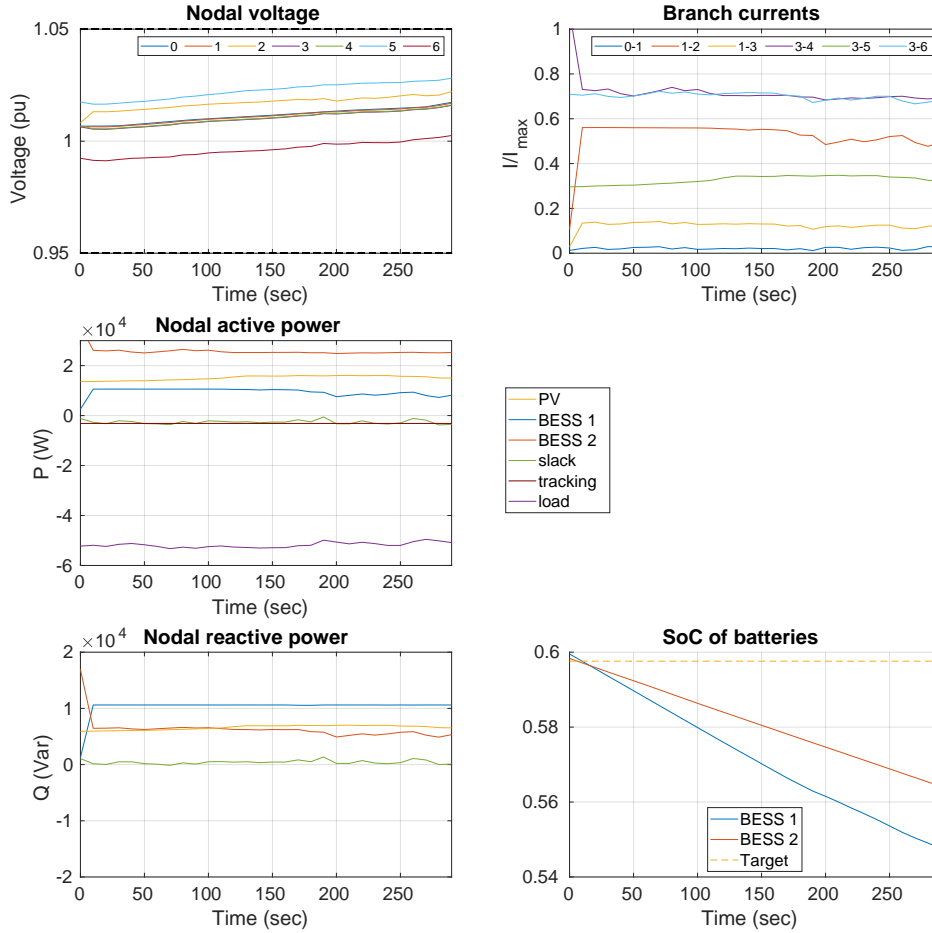


Figure 2.13: Simulation results of the second scenario, with higher load consumption, with weights: slack weight $w_s = 1$, voltage weight $w_V = 10^{-6}$, current weight $w_I = 10^{-5}$, battery weights $w_1 = w_2 = 10^{-4}$

2.4.3 Second Scenario - Larger Load Consumption

We now study a simulation of the same day, but we assume that the production of the load is 20% larger than before. The dispatch plan is computed with the same PV and load scenarios as before and is identical to the one in Section 2.4.2. However, the new realization of the load consumption is closer to the scenario of the highest consumption without exceeding it. We use the same weights for the objectives that were manually selected in the previous scenario, namely $w_s = 1$, $w_V = 10^{-6}$, $w_I = 10^{-5}$, $w_1 = w_2 = 10^{-4}$.

The simulation results are shown in Fig. 2.13. The higher load requires the BESSs to provide

2.4 Configuring the Weights of the Controller

more energy to track the dispatch plan successfully. This causes an increase in the current flowing through branch 3-4, which is very close to the ampacity of the branch at the beginning of the simulation, as we can see in the branch-currents plot in Fig. 2.13. Therefore, the controller instructs BESS 2 to slow discharging to satisfy the ampacity limit. At the same time, BESS 1 has to increase its production to track the dispatch plan with acceptable accuracy. This causes a mismatch between the two SoCs of up to 3% at the end of the simulation.

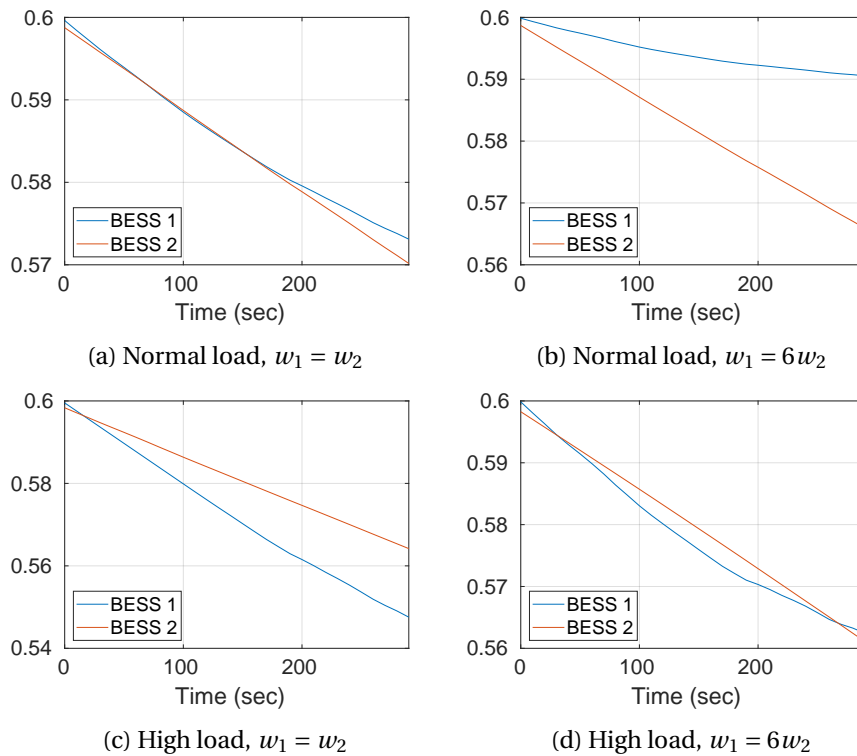


Figure 2.14: SoC of BESSs for two different load profiles and sets of weights.

To fix the mismatch, we could increase the weight of the objective of BESS 1 so that its SoC is closer to the target. We thus increase the weight w_1 until the two SoC trajectories are as close as possible throughout the simulation. In Fig. 2.14, we plot the two SoC trajectories for the first and second scenarios (normal and high load, respectively) for two sets of weights, namely $w_1 = w_2 = 10^{-4}$ and $w_1 = 6w_2 = 6 \cdot 10^{-4}$. It can be inferred from these graphs that there is no fixed set of weights that will achieve the same SoC trajectory for the BESSs irrespective of the scenario. Also, SoC fairness should not be the only criterion for choosing the weights, as fairness might not be possible if there is a binding constraint. Therefore, we conclude that the optimal choice of weights is not always obvious and that a formal method is required instead of trial and error.

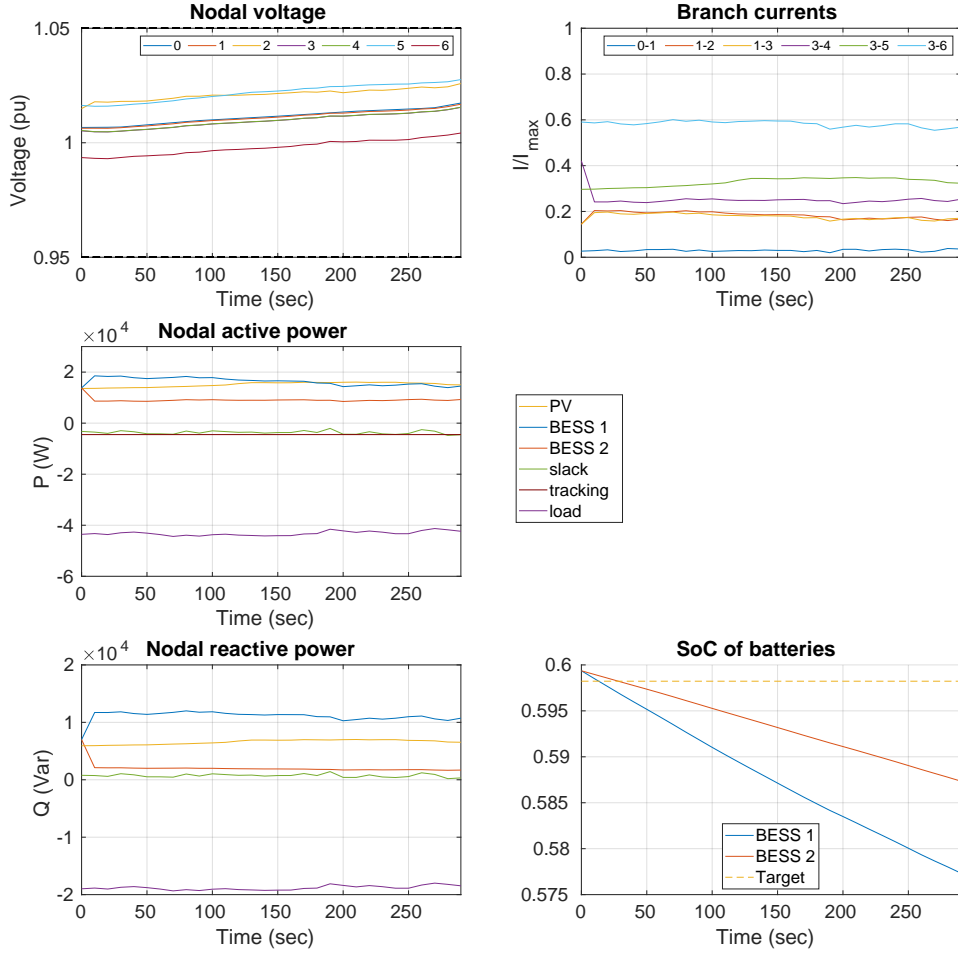


Figure 2.15: Simulation results for the third scenario, with normal load consumption and a bigger BESS 1 at 60 kVA/60 kWh. The weights are the same as in the first scenario.

2.4.4 Third Scenario - Change In the Topology

We now consider the following scenario to demonstrate further the need for a formal method to compute the controller's weights. The grid operator purchases a new BESS with the same specifications as BESS 2, i.e., 60 kVA/60 kWh, and replaces the old BESS 1 with this new BESS. The line between B1-B2 is also reinforced with a new one with four times the ampacity to ensure it can withstand the current drawn by the new BESS. Because there is a change in the grid, the first step is to re-compute the dispatch plan. We assume that the grid operator has already computed the weights from the first scenario, i.e., $w_s = 1$, $w_V = 10^{-6}$, $w_I = 10^{-5}$, $w_1 = w_2 = 10^{-4}$, so they consider using the same ones for this new grid.

We re-run the first scenario of Section 2.4.2, with the same load consumption and PV produc-

tion, after the change in topology. The results are shown in Fig. 2.15. The main difference compared to Fig. 2.12 can be observed in the SoC trajectories of the two BESSs. Indeed, the maximum difference has now increased to 1.7% and is expected to increase more if we run the simulation for a longer period. This means that the weights computed in Section 2.4.1 are no longer ideal for this new scenario.

2.4.5 Discussion

The examples of Sections 2.4.2-2.4.4 were used to showcase that the optimal set of weights is typically scenario and grid-dependent. This means that finding a set of weights that achieve acceptable performance for every possible realization of the stochastic energy resources would require running simulations for different scenarios of the stochastic prosumptions. Moreover, each change in the grid would require repeating the weight-tuning process anew, which can be tedious and time-consuming, especially in larger grids. In addition, a grid operator would have to execute the same process for each grid they operate in case they are responsible for multiple grids. Finally, even if the weights are tuned every time manually, the control might be biased because there is not a clear definition of what fair or unbiased control means.

To address the problems with the oracle-based approach, we need to define what fair control means in the context of RT control and then formalize a method to construct the cost functions in Equation (2.7) so that fairness is achieved without the need to configure any parameters a posteriori. We will address this problem again in Chapter 4, where we propose a method to design cost-functions for all the objectives defined in this section and to compute their weights intuitively, to achieve a fair control of BESSs.

But first, we will study the problem of quantifying the uncertainty of stochastic prosumption in ultra-short-term time in Chapter 3. This will prove helpful in computing the weights, as in many cases, fairness and grid constraints should be guaranteed in the presence of uncertainty.

3 Quantification of Ultra-Short-Term Uncertainty of Heterogeneous Resources in Active Distribution Networks

3.1 Purpose of Chapter

As already discussed in the state-of-the-art in Section 2.1.5, accurate forecasts of the stochastic power injections are crucial for the reliable operation of ADNs. For example, in the problem demonstrated in Section 2.4, both point and interval predictions are necessary for the function of the controller. On the one hand, accurate point predictions of the stochastic prosumptions in the Optimization Problem (2.12) may ensure accurate tracking of the dispatch plan, and on the other hand, the estimation of prediction intervals (PIs) are useful to ensure that the hard voltage and current constraints are satisfied for the worst-case scenario.

Even though the example studied in the previous chapter requires forecasts at a horizon of 10 seconds, we have discussed that other time-critical applications, such as the transition of a microgrid from a grid-connected to an islanded operation, require much faster, sub-second control decisions. Although computing point predictions in such fast time scales is a relatively easy task, for example, using a persistent forecast, estimating PIs is more complicated. We have already discussed the existing literature on electricity prosumption forecasting and found that the common techniques are inadequate to compute prediction intervals at such short time scales.

To address the issues with existing methods, we propose a non-parametric machine-learning method (published in [93]) for computing ultra short-term PIs of the power prosumption of generic electrical-distribution networks. The method first groups historical observations into clusters according to the values of influential variables, such as the power level and time of day. Two variants are discussed, one where the original time series is considered (model A) and another where the differentiated time series is considered (model B). The clusters are considered statistically representative pools of future realizations of the power prosumption or its derivative (depending on the model used). They are used to determine empirical PDFs (Probability Density Functions) and, by extracting the quantiles, to deliver PIs for respective arbitrary confidence levels. Finally, the estimated PDFs are continuously updated in real-time as new measurements become available without the need to keep past measurements in

memory. The models are validated a posteriori by conducting a performance analysis that uses experimentally observed power-prosumption for different types of prosumers, allowing for choosing the optimal values for the algorithm's parameters.

3.2 Computation of Prediction Intervals

The problem we target in this chapter is the computation of PIs, i.e., we want to predict, with a given confidence level, the interval where the future power-prosumption realization is expected to lie. Denoting the PI at the target confidence level α as the couple $(P^{\downarrow\alpha}, P^{\uparrow\alpha})$ composed by the lower and upper bound of the interval, we address the problem that consists in finding the one-step-ahead PI as a function of a sequence of n historical power-prosumption measurements until the time instant i , specifically:

$$\left(P_{i+1|i}^{\downarrow\alpha}, P_{i+1|i}^{\uparrow\alpha} \right) = f(P_i, \dots, P_{i+1-n}) \quad (3.1)$$

where i is the current time interval, and f is a PI estimation model.

As it will be exhaustively described in the rest of this section, the estimation methodology for PIs consists in grouping historical power-prosumption measurements into clusters according to the value of selected influential variables. When delivering a PI, the values of the influential variables are determined, thus allowing for the selection of the appropriate cluster that is finally used as the empirical PDF of the next realization. The algorithm is designed to deliver a PI in rolling RT with a minimum report rate equal to the measurement period, i.e., 20 ms. This lower bound is given by the fundamental frequency of a 50 Hz system and it corresponds to the measurement report rate of phasor measurement units (PMUs). Longer values are also considered when evaluating the algorithm's performance.

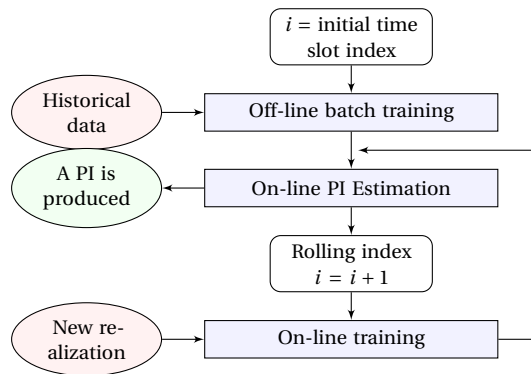


Figure 3.1: Operation sequence of the PI estimation models. The batch training is performed off-line, whereas the PIs computation and on-line training are performed in rolling RT. Ellipses denote the input and output of each phase.

The algorithm operation sequence is sketched in Fig. 3.1. The first phase, called batch training, consists of the off-line training of the estimation model that uses historical data to construct

an empirical PDF. In the second phase, the one-step-ahead PI is delivered. Finally, in the third phase, the new progressively available measurements are used for the on-line model training to update the estimated PDF. As the algorithm only needs an estimation of the PDF to compute the PIs, the on-line training can be performed without keeping past data in memory. This methodology is applied in two flavors, specifically on the original and differentiated time series, as discussed in the following two sections.

3.2.1 PI Model A

Off-Line Batch Training

We consider n historical power-prosumption measurements P_{i+1-n}, \dots, P_i and the respective time stamp t_{i+1-n}, \dots, t_i . Power-prosumption measurements are discretized in time and amplitude with user-defined discretization steps ΔT and ΔP , respectively. We define c as the operator that determines a non-negative integer l , said *label*, according to the power-prosumption value and timestamp in the following way:

$$l_j = c(P_j, t_j), \quad l_j \in \{0, 1, \dots, L-1\}. \quad (3.2)$$

where j is a generic time slot, and L is the total number of labels. The process used to operate the classification c is described in detail in Section 3.2.3. The label in (3.2) is utilized to group the historical power-prosumption measurements P_j into L clusters, denoted as $\mathbb{G}_i^0, \dots, \mathbb{G}_i^{L-1}$. Each cluster contains all the historical power-prosumption measurements for which the previous observation was of the respective given label. For example, the cluster \mathbb{G}_i^0 contains the measurements until the time slot i for which the respective previous realization was with label 0, \mathbb{G}_i^1 those for which the respective previous realization was with label 1, and so on. Formally, the clusters are defined as:

$$\mathbb{G}_i^l = \{P_{j+1} : c(P_j, t_j) = l, j = i-n, \dots, i-1\}, \quad (3.3)$$

$$l = 0, \dots, L-1.$$

Let $\mathcal{G}_i^0, \dots, \mathcal{G}_i^{L-1}$ be the normalized histogram of each cluster computed as

$$\mathcal{G}_i^l(x) = \frac{1}{|\mathbb{G}_i^l|} \sum_{p \in \mathbb{G}_i^l} \delta(x-p), \quad l = 0, \dots, L-1 \quad (3.4)$$

where $|\cdot|$ denotes the set cardinality (i.e., the number of elements it contains) and δ is the Dirac measure:

$$\delta(x) = \begin{cases} 1 & x = 0 \\ 0 & \text{otherwise.} \end{cases} \quad (3.5)$$

Chapter 3. Quantification of Ultra-Short-Term Uncertainty of Heterogeneous Resources in Active Distribution Networks

As the power prosumption is bounded, say between P_{\min} and P_{\max} , histograms in (3.4) are defined over a finite domain. Specifically, the domain is as:

$$x \in \mathbb{X} = \{P_{\min}, P_{\min} + \Delta P, P_{\min} + 2\Delta P, \dots, P_{\max}\}. \quad (3.6)$$

The value of ΔP is chosen as a trade-off between accuracy and computational efficiency. Indeed, the smaller the ΔP is, the more accurate the prediction of the PI is. This aspect is made clear below. However, choosing a very small step will require more memory to store all the measurements, thus resulting in a slower computation of the PI.

On-Line PI Estimation

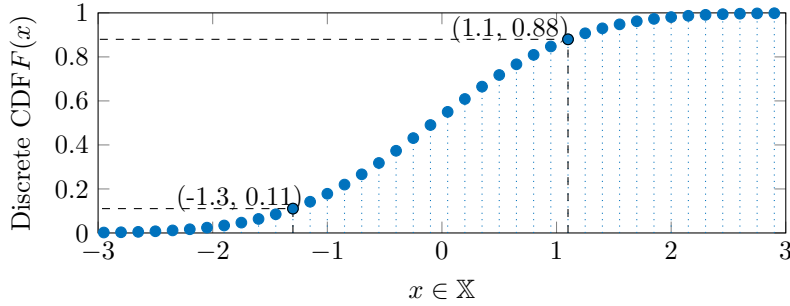


Figure 3.2: Exemplification of the procedure (3.10)-(3.11) to approximate the quantiles for (3.8)-(3.9) for a normal distribution. In this case, the target confidence level α is 80%.

At time i , the objective of the PI estimator is to determine the PI for the time slot $i + 1$ at a given arbitrary target confidence level, said α . The underlying idea is to assume the clusters (3.3) as a statistically representative pool of possible realizations of the one-step-ahead power-prosumption realization. Therefore, the normalized histograms (3.4) are assumed to be discrete PDFs and used to extract the symmetric quantiles corresponding to the α confidence level. Let

$$l_i = c(P_i, t_i) \quad (3.7)$$

be the label calculated with the information at the current time instant. The PI lower and upper bounds are determined as

$$P_{i+1|i}^{\downarrow\alpha} = (1 - \alpha)/2 \text{ quantile of } \mathcal{G}_i^{l_i}, \quad (3.8)$$

$$P_{i+1|i}^{\uparrow\alpha} = (1 + \alpha)/2 \text{ quantile of } \mathcal{G}_i^{l_i}. \quad (3.9)$$

For the sake of clarity, the lower and upper quantiles in the expressions above are approximated by, respectively:

$$\inf_{x \in \mathbb{X}} \{x : F(x) \geq (1 - \alpha)/2\} \quad (3.10)$$

and

$$\sup_{x \in \mathbb{X}} \{x : F(x) \leq (1 - \alpha)/2\}, \quad (3.11)$$

where F denotes the discrete CDF (cumulative distribution function) of \mathcal{G}_i^l calculated by computing its cumulative sum. An example of the PI estimation is shown in Fig.3.2 for a normal distribution.

There are two advantages to this approach. First, histograms carry the complete information over the empirical PDFs, thus allowing for computing PIs at arbitrary confidence levels by training only one model. Therefore, we do not need to train another model if the performance requirements change. Second, it overcomes the problem of quantile crossing that arises, for example, in [78], from treating the bounds at a given confidence level as two different time series. As a matter of fact, quantile crossing produces a mistake in the model that has to be handled by a suitable correction mechanism in the controller. However, in time-critical applications where high reliability is desired, such as the islanding maneuver, the controller needs to ensure the validity of its decisions and should not make any assumptions about the causes of the quantile crossing.

On-Line Training

As time passes, new measurements become available and can be included to improve future PI estimates. Once the outcome P_{i+1} is known, the normalized histogram associated with the label l_i is updated with the new information, and the other histograms stay the same. Formally, the training procedure is as follows:

$$\mathcal{G}_{i+1}^l(x) = \begin{cases} \phi \mathcal{G}_i^l(x) + (1 - \phi) \delta(x - P_{i+1}) & l = l_i \\ \mathcal{G}_i^l(x) & l \neq l_i, \end{cases} \quad (3.12)$$

where

$$\phi = \frac{T_\phi / T}{T_\phi / T + 1} \quad (3.13)$$

is called the *forgetting factor*, T is the measurement period and T_ϕ is called the *forgetting time constant*. The forgetting factor controls how much past measurements influence the computation of PIs. Specifically, each new measurement has the same weight in the computation as all the measurements in the past T_ϕ seconds. The adoption of such a forgetting factor is important in order to track changes in the composition of prosumers' load/generation patterns.

3.2.2 PI Model B

Off-Line Batch Training

We apply the same principles described for Model A but on the once differentiated power-prosumption training data-set. The differentiated time series is denoted as:

$$B_j = P_j - P_{j-1}, \quad j = i - n + 1, \dots, i. \quad (3.14)$$

The observations clusters are now calculated as follows:

$$\begin{aligned} \mathbb{H}_i^l = \{B_{j+1} : c(P_j, t_j) = l, j = i - n + 1, \dots, i - 1\}, \\ l = 0, \dots, L - 1, \end{aligned} \quad (3.15)$$

and are used to determine the normalized histograms of the differentiated power prosumption time series, which are denoted as $\mathcal{H}_i^0, \dots, \mathcal{H}_i^{L-1}$.

On-Line PI Estimation

The one-step-ahead PI bounds are computed as:

$$P_{i+1|i}^{\downarrow\alpha} = P_i + (1 - \alpha)/2 \text{ quantile of } \mathcal{H}_i^{l_i}, \quad (3.16)$$

$$P_{i+1|i}^{\uparrow\alpha} = P_i + (1 + \alpha)/2 \text{ quantile of } \mathcal{H}_i^{l_i}, \quad (3.17)$$

i.e., the current power-prosumption plus two back-off terms representing the expected power prosumption variation with respect to the current realization P_i .

On-Line Training

Once the prosumption P_{i+1} is known and the power difference B_{i+1} is computed, the normalized histogram corresponding to the current label l_i is updated by adding the new differenced value, whereas the others stay the same, i.e.,

$$\mathcal{H}_{i+1}^l(x) = \begin{cases} \phi \mathcal{H}_i^l(x) + (1 - \phi) \delta(x - B_{i+1}) & l = l_i \\ \mathcal{H}_i^l(x) & l \neq l_i. \end{cases} \quad (3.18)$$

3.2.3 Classification According to Influential Variables

The assignment performed through the function $c(\cdot)$ in (3.2) is realized by first clustering the historical measurements into groups based on similarities with respect to chosen influential variables and, then, assigning a cluster label to each new measurement. Needless to say, influential (or explanatory) variables are quantities that have an influence on the power prosumption. In general, they can be discovered using numerical methods (like principal

component analysis (PCA), analysis of variance, correlation analysis, or other procedures [94]) or identified by exploiting any empirical knowledge on the observed process (in our case the structure of prosumption of a given node).

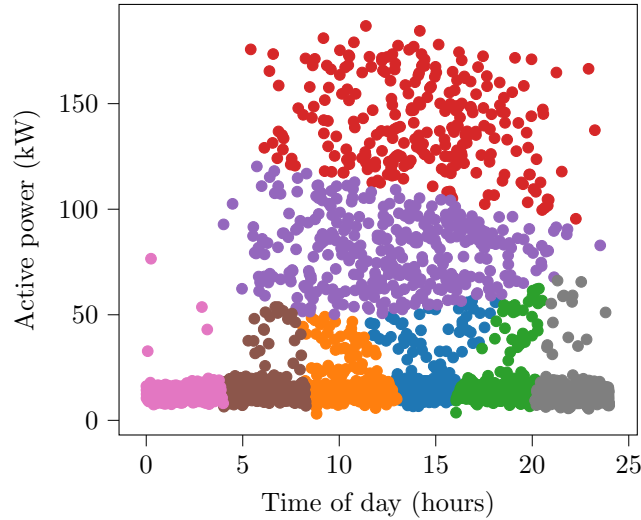


Figure 3.3: Visualization of k-means clustering for a node with an EV charging station with 8 clusters and using the power level and the time of day as influential variables. Positive power is consumption.

In this work, influential variables are chosen by adopting the latter approach. The chosen variables are (i) power magnitudes and (ii) time of day (in seconds). The first variable accounts that, in a limited capacity feeder, prosumption variations depend on the same power-prosumption magnitude. For example, when the consumption is large, a load disconnection is more likely than a load insertion because many loads are already active, and vice-versa. The second variable is supposed to capture the different power-prosumption patterns that might occur during the day.

The historical measurements are grouped, by using a k-means approach, into L clusters, according to the values of the influential variables. The clusters are initialized using the greedy k-means++ algorithm and the clustering is performed in batches of 65536 data points (mini-batch k-means). An example of the clustering method is shown in Fig. 3.3 for a node with an office building and a level-3 EV charging station. The k-means algorithm was trained with two weeks of historical measurements by using both the power level and the time of day as influential variables and by grouping the measurements into $L = 8$ clusters, each of which is labeled with a different color in the figure. In this example, the measurements of the node when there are no connected EVs, which is the most frequent case, have been split into 6 clusters, dividing the day into 6 time periods. The rare occasions of an EV connection, which is characterized by a total consumption larger than 50 kW, have been split into two clusters depending on the power level (50-100 kW and 100-200 kW approximately). The value of L is chosen by the user and is fixed a priori. Its influence on the algorithm's performance is studied

Chapter 3. Quantification of Ultra-Short-Term Uncertainty of Heterogeneous Resources in Active Distribution Networks

in Section 3.3.

During the off-line and on-line training phases of the algorithm, the label of measurement (P_i, t_i) is computed as follows:

$$l_i = \arg \min_{l=0, \dots, L-1} d(e(P_i, t_i), c_l) \quad (3.19)$$

where $e(P_i, t_i)$ is the point in the $m-d$ space whose coordinates are the m influential variables chosen in the classification scheme, c_l is the center of cluster l and $d(\cdot, \cdot)$ is the Euclidean distance between two points.

The different classification schemes are introduced with the objective of performing an a-posteriori validation of the selection process of influential variables and the number of clusters. Indeed, as stated earlier in this section, influential variables are assigned by exploiting the empirical knowledge of the process: By comparing the performance of different classification schemes (in Section 3.3), it is possible to infer whether the progressively more complex classification schemes are meaningful or not.

3.2.4 Implementation Aspects and Complexity

The main design requirement of the proposed algorithm is to deliver PIs in RT in order to, for example, activate enough capacity in inertia-less microgrids or to assist in the decision process of setting the droop controller of slack generators in the islanding maneuver. Given the large PIs reporting rate, computational complexity is a central aspect and hence is addressed in this section. The batch-training phase does not have RT requirements because it is performed off-line. This consists in labeling each observation of the training data-set by applying the discussed classification algorithm. As the number of labels L is fixed by design, the overall complexity of the classification procedure, given by Equation (3.19), for one observation is constant time, or $O(1)$. Iterating it over a set of N training data is an operation with linear time complexity, or $O(N)$.

The computation of the PIs and the on-line training are performed in rolling RT. The former operation requires computing the label in (3.7), which is $O(1)$, and the PI bounds by (3.9)-(3.11), which involve a minimum and maximum search over the set \mathbb{X} , a problem with log time complexity with respect to the set cardinality, $O(\log_2 |\mathbb{X}|)$, e.g., using a binary search that can exploit the monotonicity of the discrete CDFs. However, as the cardinality of \mathbb{X} is fixed by design in (3.6), the complexity of the problem can be regarded as constant time. Therefore, delivering PIs and performing on-line training are procedures whose complexities do not scale with the size of the problem.

The training data and progressively incoming measurements are encoded in L normalized histograms. Each of them is stored using $2 \times |\mathbb{X}|$ doubles, specifically the height and value of each bin. For example, assuming a discretization of 1024 levels (10 bit), preserving the

information for a 1 year at 20 ms of resolution with the proposed method requires 128 kB per label (considering a double representation of 64-bit), while storing the individual values would require approximately 14 Gb.

3.3 Performance Evaluation

3.3.1 A real case application: university buildings

To test the performance of the proposed models, we consider four sequences of power-prosumption measurements that were recorded from different points inside the MV distribution network of the EPFL campus. The first three prosumers are very different regarding maximum power and power variations and were chosen to test our algorithm in the most challenging case for forecasting models: the lowest aggregation level. The first one consists of an office building with a maximum consumption of 80 kW and is equipped with a 30 kVA roof PV; the second one includes an office load with a maximum consumption of 30 kW and a 150 kW level 3 EV charging station; and the third one is a heat pump with a maximum consumption of 3 MW. Finally, to evaluate the algorithm at a higher aggregation level, we have considered the measurements on a primary substation supplying 8 MV feeders interfacing 20 heterogeneous prosumers, which comprise about half of the EPFL campus. The prosumption includes multiple office buildings, 1 MWp of PV production, and two heat pumps with a total maximum consumption of 4 MW. Even though the rated power of the primary substation transformer is 40 MVA, the maximum active power flow observed in the concerned period was 8 MW, which is the value we consider as P_{\max} in the implementation of the algorithm (Equation (3.6)). Fig. 3.4 shows the PDFs of the four prosumptions that were estimated in a given period of 30-45 days and of the respective differentiated time series.

The measurements are with a resolution of 20 ms and are provided by a PMU-based metering infrastructure that has been deployed on the university campus (see [95]). For the first three prosumers, we consider 45 days of historical power-prosumption measurements that span the period of September-October 2022, whereas for the MV feeders, we consider 30 days in January-February 2024. In each case, we consider two weeks of training data; they are used to construct the clusters (as explained in Section 3.2.3) and to perform the off-line training of the algorithm. Then, the proposed PI estimation models are operated for the rest of the available measurements (with on-line training), and the estimated PIs are validated against the latter data-set, at 20 ms resolution. Each month consists of approximately 130 million data points. The evaluation is performed in a simulated environment coded in C++. The simulations are executed in a Windows Server with 128 GB RAM and an Intel Xeon Gold 6130 CPU at 2.10 GHz.

3.3.2 Performance Metrics

We introduce the following metrics to allow for a quantitative comparison between the performance of models and classification schemes. The first is the PI normalized averaged width

Chapter 3. Quantification of Ultra-Short-Term Uncertainty of Heterogeneous Resources in Active Distribution Networks

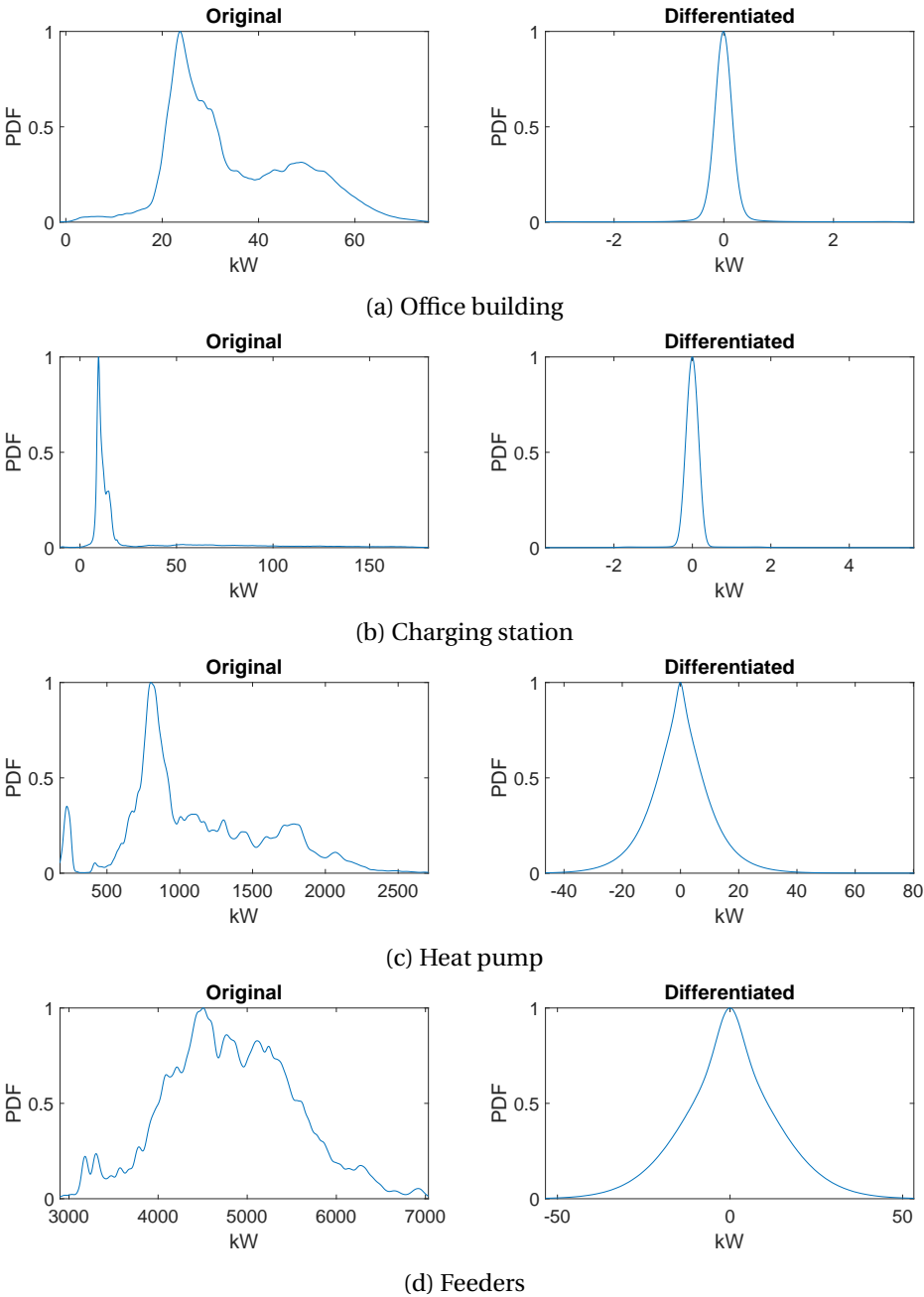


Figure 3.4: Normalized PDF of power prosumption for the studied prosumers. To aid readability, the x-axis has been limited to a 99.9% confidence level.

(PINAW), which is as follows:

$$\text{PINAW} = \frac{1}{N} \sum_{j=1}^N (P_j^{\uparrow\alpha} - P_j^{\downarrow\alpha}) / P_{\max}. \quad (3.20)$$

The second metric is the PI coverage probability (PICP), i.e., the percentage of power-prosumption realization that falls inside the predicted PI. It is as follows:

$$\text{PICP} = \frac{1}{N} \sum_{j=1}^N b_j^\alpha \quad (3.21)$$

where

$$b_j^\alpha = \begin{cases} 1, & P_j^{\downarrow\alpha} \leq P_j \leq P_j^{\uparrow\alpha} \\ 0, & \text{otherwise.} \end{cases} \quad (3.22)$$

Because there is a trade-off between the width of the PI and the accuracy of the model, it is imperative that we define a third metric to quantify it. The metric we chose for this purpose is a modification of the coverage width-based criterion (CWC) proposed in [96] and is defined as follows:

$$\text{CWC} = \text{PINAW} \max(1, e^{-\mu \frac{\text{PICP} - \alpha}{1 - \alpha}}) \quad (3.23)$$

where μ is a user-defined parameter that quantifies the trade-off between PICP and PINAW. For our experiments, we chose $\mu = \frac{\log(10)}{10}$. This means that a deviation of one order of magnitude in the error rate penalizes the width of the interval by 10 times. The same result can be achieved with a linear penalty with slope 0.9, as can be seen in Fig. 3.5. The x -axis is the percentage deviation of the error rate from the target error rate, whereas the y -axis is the ratio $\frac{\text{CWC}}{\text{PINAW}}$. We observe that the exponential function penalizes less severely the error rates within one order of magnitude in comparison to the linear function. However, with our choice, higher error rates are more penalized.

3.3.3 Clustering Using Power Levels

We consider four target confidence levels α to evaluate the algorithm, namely 99, 99.9, 99.99, and 99.999%. The chosen confidence levels are particularly high because the time resolutions are very short and because we want to test the limits of our algorithm. For example, a 1% error rate at 20 ms would result in an average of one error every 2 seconds. The parameters to be analyzed are (i) the model A or B, (ii) the number of clusters L , and (iii) the forgetting factor ϕ or, equivalently, the forgetting constant T_ϕ . Each combination of model, L and T_ϕ is called a *configuration*. To choose the best configuration for each prosumer, we run the algorithm for both models A and B, with all possible combinations of values of L in the set

Chapter 3. Quantification of Ultra-Short-Term Uncertainty of Heterogeneous Resources in Active Distribution Networks

Table 3.1
PERFORMANCE EVALUATION FOR THE OFFICE BUILDING AT 20 MS RESOLUTION (5 BEST CONFIGURATIONS)

| Model | L | T_ϕ (sec) | PINAW | PICP | CWC |
|-------|------|----------------|----------|---------|----------|
| B | 8 | 604800 | 0.021477 | 0.99129 | 0.021477 |
| B | 1 | 604800 | 0.021479 | 0.99021 | 0.021479 |
| B | 256 | 86400 | 0.021582 | 0.9916 | 0.021582 |
| B | 1024 | 21600 | 0.021645 | 0.99166 | 0.021645 |
| B | 512 | 21600 | 0.02175 | 0.99178 | 0.02175 |

(a) $\alpha = 0.99$

| Model | L | T_ϕ (sec) | PINAW | PICP | CWC |
|-------|------|----------------|----------|---------|----------|
| B | 1 | 604800 | 0.030539 | 0.99909 | 0.030539 |
| B | 8 | 604800 | 0.030844 | 0.99913 | 0.030844 |
| B | 1024 | 21600 | 0.031535 | 0.99924 | 0.031535 |
| B | 256 | 86400 | 0.031546 | 0.99924 | 0.031546 |
| B | 1024 | 86400 | 0.031795 | 0.99924 | 0.031795 |

(b) $\alpha = 0.999$

| Model | L | T_ϕ (sec) | PINAW | PICP | CWC |
|-------|------|----------------|----------|---------|---------|
| B | 1 | 604800 | 0.0495 | 0.99978 | 0.11225 |
| B | 8 | 604800 | 0.050864 | 0.99976 | 0.11787 |
| B | 256 | 86400 | 0.051083 | 0.99976 | 0.11876 |
| B | 512 | 21600 | 0.051254 | 0.99976 | 0.11926 |
| B | 1024 | 21600 | 0.051295 | 0.99976 | 0.11981 |

(c) $\alpha = 0.9999$

| Model | L | T_ϕ (sec) | PINAW | PICP | CWC |
|-------|-----|----------------|----------|---------|---------|
| B | 1 | 604800 | 0.097604 | 0.99999 | 0.19928 |
| B | 8 | 604800 | 0.087544 | 0.99996 | 0.2362 |
| B | 64 | 86400 | 0.086138 | 0.99996 | 0.25202 |
| B | 256 | 86400 | 0.085014 | 0.99996 | 0.25275 |
| B | 256 | 21600 | 0.085897 | 0.99996 | 0.25565 |

(d) $\alpha = 0.99999$

3.3 Performance Evaluation

Table 3.2
PERFORMANCE EVALUATION FOR THE CHARGING STATION AT 20 MS RESOLUTION (5 BEST CONFIGURATIONS)

| Model | L | T_ϕ (sec) | PINAW | PICP | CWC |
|-------|------|----------------|-----------|---------|-----------|
| B | 8 | 86400 | 0.0070666 | 0.99068 | 0.0070666 |
| B | 64 | 86400 | 0.0078829 | 0.99058 | 0.0078829 |
| B | 256 | 21600 | 0.0081288 | 0.99077 | 0.0081288 |
| B | 512 | 3600 | 0.0093646 | 0.9923 | 0.0093646 |
| B | 1024 | 3600 | 0.0093689 | 0.99139 | 0.0093689 |

(a) $\alpha = 0.99$

| Model | L | T_ϕ (sec) | PINAW | PICP | CWC |
|-------|-----|----------------|----------|---------|----------|
| B | 8 | 86400 | 0.019295 | 0.99868 | 0.039879 |
| B | 1 | 86400 | 0.019835 | 0.9988 | 0.040468 |
| B | 256 | 86400 | 0.019518 | 0.99832 | 0.041887 |
| B | 64 | 86400 | 0.02061 | 0.99875 | 0.042265 |
| B | 512 | 21600 | 0.020008 | 0.99847 | 0.042272 |

(b) $\alpha = 0.999$

| Model | L | T_ϕ (sec) | PINAW | PICP | CWC |
|-------|-----|----------------|----------|---------|----------|
| B | 8 | 86400 | 0.032019 | 0.99958 | 0.093142 |
| B | 64 | 86400 | 0.03352 | 0.99956 | 0.099959 |
| B | 256 | 21600 | 0.033447 | 0.99953 | 0.10298 |
| B | 64 | 21600 | 0.034654 | 0.99955 | 0.10403 |
| B | 256 | 86400 | 0.032912 | 0.99951 | 0.10529 |

(c) $\alpha = 0.9999$

| Model | L | T_ϕ (sec) | PINAW | PICP | CWC |
|-------|-----|----------------|----------|---------|---------|
| B | 8 | 86400 | 0.051835 | 0.99992 | 0.27484 |
| B | 64 | 86400 | 0.054395 | 0.9999 | 0.35737 |
| B | 64 | 21600 | 0.053203 | 0.9999 | 0.3654 |
| B | 256 | 21600 | 0.05643 | 0.9999 | 0.42839 |
| B | 1 | 86400 | 0.061909 | 0.9999 | 0.4564 |

(d) $\alpha = 0.99999$

Chapter 3. Quantification of Ultra-Short-Term Uncertainty of Heterogeneous Resources in Active Distribution Networks

Table 3.3
PERFORMANCE EVALUATION FOR THE HEAT PUMP AT 20 MS RESOLUTION (5 BEST CONFIGURATIONS)

| Model | L | T_ϕ (sec) | PINAW | PICP | CWC |
|-------|-----|----------------|-----------|---------|----------|
| B | 1 | 60 | 0.0094042 | 0.98832 | 0.019179 |
| A | 1 | 1 | 0.010129 | 0.98714 | 0.020948 |
| B | 64 | 60 | 0.0092479 | 0.97969 | 0.020973 |
| B | 8 | 1 | 0.0087772 | 0.9754 | 0.021062 |
| B | 64 | 604800 | 0.0086629 | 0.97348 | 0.021334 |

(a) $\alpha = 0.99$

| Model | L | T_ϕ (sec) | PINAW | PICP | CWC |
|-------|-----|----------------|----------|---------|----------|
| B | 1 | 60 | 0.012571 | 0.99709 | 0.032104 |
| B | 64 | 60 | 0.012433 | 0.99495 | 0.044051 |
| B | 8 | 3600 | 0.019926 | 0.9973 | 0.049417 |
| B | 1 | 3600 | 0.020044 | 0.99733 | 0.049491 |
| B | 8 | 604800 | 0.020017 | 0.99723 | 0.050086 |

(b) $\alpha = 0.999$

| Model | L | T_ϕ (sec) | PINAW | PICP | CWC |
|-------|------|----------------|----------|---------|---------|
| A | 1 | 3600 | 0.15949 | 0.99945 | 0.61341 |
| B | 8 | 86400 | 0.035472 | 0.99868 | 0.61803 |
| B | 8 | 604800 | 0.034094 | 0.99865 | 0.63687 |
| B | 64 | 604800 | 0.027909 | 0.99855 | 0.64976 |
| B | 1024 | 21600 | 0.03545 | 0.99864 | 0.67909 |

(c) $\alpha = 0.9999$

| Model | L | T_ϕ (sec) | PINAW | PICP | CWC |
|-------|-----|----------------|----------|---------|---------|
| A | 1 | 3600 | 0.18531 | 0.99996 | 0.59946 |
| A | 1 | 21600 | 0.38217 | 0.99994 | 1.5316 |
| A | 1 | 86400 | 0.59664 | 0.99994 | 2.6857 |
| A | 1 | 604800 | 0.68619 | 0.99984 | 22.893 |
| B | 512 | 604800 | 0.088159 | 0.99949 | 9480.1 |

(d) $\alpha = 0.99999$

3.3 Performance Evaluation

Table 3.4
PERFORMANCE EVALUATION FOR THE MV FEEDERS AT 20 MS RESOLUTION (5 BEST CONFIGURATIONS)

| Model | L | T_ϕ (sec) | PINAW | PICP | CWC |
|-------|------|----------------|-----------|---------|-----------|
| B | 8 | 21600 | 0.0043777 | 0.99021 | 0.0043777 |
| B | 256 | 3600 | 0.0045151 | 0.99053 | 0.0045151 |
| B | 512 | 3600 | 0.0045814 | 0.99118 | 0.0045814 |
| B | 64 | 21600 | 0.0046129 | 0.99066 | 0.0046129 |
| B | 1024 | 3600 | 0.0046549 | 0.99179 | 0.0046549 |

(a) $\alpha = 0.99$

| Model | L | T_ϕ (sec) | PINAW | PICP | CWC |
|-------|------|----------------|-----------|---------|-----------|
| B | 64 | 21600 | 0.0061943 | 0.999 | 0.0061943 |
| B | 256 | 21600 | 0.0062623 | 0.99908 | 0.0062623 |
| B | 512 | 21600 | 0.0062895 | 0.99911 | 0.0062895 |
| B | 1024 | 21600 | 0.0063163 | 0.99912 | 0.0063163 |
| B | 64 | 86400 | 0.0063793 | 0.99911 | 0.0063793 |

(b) $\alpha = 0.999$

| Model | L | T_ϕ (sec) | PINAW | PICP | CWC |
|-------|-----|----------------|-----------|---------|-----------|
| B | 64 | 21600 | 0.0080307 | 0.9999 | 0.0080307 |
| B | 256 | 21600 | 0.0081893 | 0.99991 | 0.0081893 |
| B | 64 | 86400 | 0.0082057 | 0.99991 | 0.0082057 |
| B | 64 | 604800 | 0.0082915 | 0.99991 | 0.0082915 |
| B | 512 | 21600 | 0.0082942 | 0.99991 | 0.0082942 |

(c) $\alpha = 0.9999$

| Model | L | T_ϕ (sec) | PINAW | PICP | CWC |
|-------|-----|----------------|----------|---------|----------|
| B | 1 | 86400 | 0.018185 | 0.99999 | 0.018185 |
| B | 8 | 604800 | 0.018747 | 0.99999 | 0.018747 |
| B | 1 | 604800 | 0.018985 | 0.99999 | 0.018985 |
| B | 64 | 86400 | 0.019238 | 0.99999 | 0.019238 |
| B | 64 | 604800 | 0.020687 | 0.99999 | 0.020687 |

(d) $\alpha = 0.99999$

Chapter 3. Quantification of Ultra-Short-Term Uncertainty of Heterogeneous Resources in Active Distribution Networks

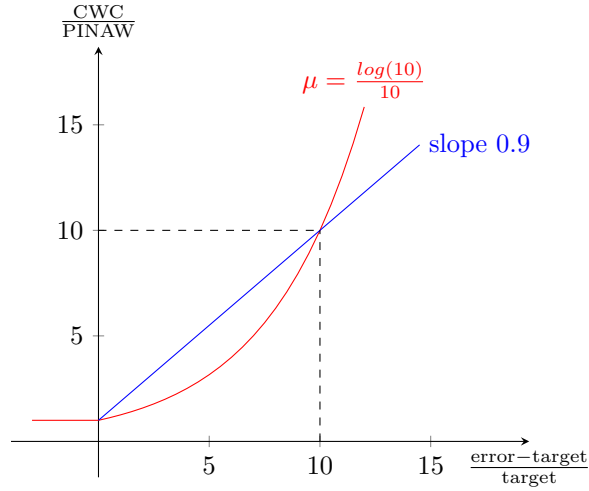


Figure 3.5: Visual representation of the CWC. $\text{error} = 1 - \text{PICP}$ is the error rate of the algorithm, and $\text{target} = 1 - \alpha$ is the target error rate. The red line indicates Equation (3.23) with the chosen value of μ , and the blue line indicates a linear penalty.

{1, 8, 64, 256, 512, 1024} and T_ϕ in the set {1, 60, 3600, 21600, 86400, 604800} seconds¹. For all the experiments, the value of the quantization step ΔP was chosen such that the size of the domain \mathbb{X} (see Equation (3.6)) is equal to 2000 points. It was experimentally observed that the values of PIs computed using larger domains did not change within three significant digits. Also, the average time needed to compute the PI and do one cycle of on-line training was around 50 μs ; thus, the method meets the RT requirements.

For each combination of models, of a number of clusters, and time constants, and for each confidence level α , we compute the three metrics PINAW, PICP, and CWC. Tables 3.1, 3.2, 3.3, and 3.4 show the top 5 configurations, i.e., those that achieve the smallest CWC, for each target confidence level, for the four prosumers, respectively.

Concerning the office building and the one hosting the EV charging station, model B outperforms model A for every confidence level. Also, for confidence levels up to 99.9%, the algorithm is able to achieve the target confidence. For higher confidence levels, however, the algorithm misses the target confidence by at most one order of magnitude. Given our choice of the parameter μ , this means that the computed CI is penalized by a maximum factor of 10 in the computation of CWC.

Regarding the optimal configuration, fewer clusters, together with larger forgetting time constants, are better choices. More specifically, the optimal number of clusters L does not need to be larger than 8, whereas a value of T_ϕ between one day and one week is the optimal choice. By taking a closer look at Tables 3.1 and 3.2, we observe a trade-off between the values of L and T_ϕ in the performance of the algorithm. If we focus on Table 3.1a, for example, we

¹The values correspond to 1 second, 1 minute, 1 hour, 6 hours, 1 day and 1 week respectively.

notice that we could choose, without affecting the value of CWC by more than 1%, either a combination of 8 clusters and a forgetting time constant of one week, or 256 clusters and one day, or 1024 clusters and 6 hours. In fact, this table showcases that the choice of L and T_ϕ has a minor effect on the computation of PIs for the office building. The performance of the algorithm is mainly influenced by the differentiation of the measurements performed by model B. For the charging station, however, more clusters perform up to 30% worse compared to the optimal case of only 8 clusters.

The results are quite different for the heat pump in Table 3.3. First of all, the algorithm can only approach the target confidence levels within one order of magnitude. Unlike the other two buildings, the optimal results are achieved by a combination of few clusters (ideally only one) and a small forgetting time constant (less than an hour). This implies that the consumption of the heat pump changes more rapidly than that of the office building and the charging station, and that the measurements older than one hour do not influence the computation of PIs. We also observe that model A outperforms model B for large confidence levels. Even though the value of PINAW computed by model A is up to 5 times larger than the one computed by model B, model B fails to achieve the target confidence level by up to two orders of magnitude, which results in an exponential increase in the metric CWC.

Finally, the algorithm performs better when applied to the large heterogeneous aggregated prosumption of the EPFL campus (see Table 3.4) than the three individual prosumers. The algorithm can achieve all four target confidence levels, and the relative widths of the PIs are around 5 times smaller than the respective ones for the office building, which was the best-performing case of the first three prosumers. This result showcases that it is easier to forecast electrical prosumption at higher aggregation levels and that the proposed PI computation method can be reliably applied to different prosumers' aggregated levels.

Overall, we conclude that the optimal choice of model, L and T_ϕ depends on the characteristics of the prosumer. Nodes with low volatility, such as an office building, benefit from a long memory of up to one week, whereas nodes characterized by rapid power changes require the use of short memory. The clustering of power measurements seems to benefit mainly nodes with clearly distinct power levels, such as those at a charging station. But in any case, the number of clusters does not need to be more than 8. Finally, the differentiation of power (i.e., model B) improves the computation of PIs, provided that the power differentials have low volatility, as is the case for the office building and the charging station.

3.3.4 Clustering Using Power Levels and Time of Day

In this section, we consider whether adding the time of day (TOD) as a feature of the algorithm, in addition to the power level (P), would improve the performance of the algorithm. The idea is that the clustering based on TOD will capture the patterns that the prosumption exhibits during the day and that this might affect the computation of the PIs. We re-run the experiments of the previous section, with the addition of the TOD. The best configuration is again the one

Chapter 3. Quantification of Ultra-Short-Term Uncertainty of Heterogeneous Resources in Active Distribution Networks

Table 3.5
BEST CONFIGURATION AT 20 MS RESOLUTION - CLUSTERING BASED ON POWER (P) AND POWER+TIME OF DAY (P+TOD)

| α | Model | | L | | T_ϕ (sec) | | PINAW | | PICP | | CWC | |
|----------|-------|-------|---|-------|----------------|--------|---------|---------|---------|---------|---------|---------|
| | P | P+TOD | P | P+TOD | P | P+TOD | P | P+TOD | P | P+TOD | P | P+TOD |
| 0.99 | B | B | 8 | 8 | 604800 | 86400 | 0.02148 | 0.02127 | 0.99129 | 0.99038 | 0.02148 | 0.02127 |
| 0.999 | B | B | 1 | 1 | 604800 | 604800 | 0.03054 | 0.03054 | 0.99909 | 0.99909 | 0.03054 | 0.03054 |
| 0.9999 | B | B | 1 | 1 | 604800 | 604800 | 0.04950 | 0.04950 | 0.99978 | 0.99978 | 0.11455 | 0.11455 |
| 0.99999 | B | B | 1 | 1 | 604800 | 604800 | 0.09760 | 0.09760 | 0.99999 | 0.99999 | 0.19992 | 0.19992 |

(a) OFFICE BUILDING

| α | Model | | L | | T_ϕ (sec) | | PINAW | | PICP | | CWC | |
|----------|-------|-------|---|-------|----------------|-------|---------|---------|---------|---------|---------|---------|
| | P | P+TOD | P | P+TOD | P | P+TOD | P | P+TOD | P | P+TOD | P | P+TOD |
| 0.99 | B | B | 8 | 8 | 86400 | 86400 | 0.00707 | 0.00749 | 0.99068 | 0.99138 | 0.00707 | 0.00749 |
| 0.999 | B | B | 8 | 8 | 86400 | 21600 | 0.01930 | 0.01843 | 0.99868 | 0.99848 | 0.04008 | 0.03918 |
| 0.9999 | B | B | 8 | 8 | 86400 | 86400 | 0.03202 | 0.03233 | 0.99958 | 0.99957 | 0.09942 | 0.10076 |
| 0.99999 | B | B | 8 | 8 | 86400 | 86400 | 0.05183 | 0.05399 | 0.99992 | 0.99992 | 0.32993 | 0.29896 |

(b) CHARGING STATION

| α | Model | | L | | T_ϕ (sec) | | PINAW | | PICP | | CWC | |
|----------|-------|-------|---|-------|----------------|-------|---------|---------|---------|---------|---------|---------|
| | P | P+TOD | P | P+TOD | P | P+TOD | P | P+TOD | P | P+TOD | P | P+TOD |
| 0.99 | B | B | 1 | 1 | 60 | 60 | 0.00940 | 0.00940 | 0.98832 | 0.98832 | 0.01918 | 0.01918 |
| 0.999 | B | B | 1 | 1 | 60 | 60 | 0.01257 | 0.01257 | 0.99709 | 0.99709 | 0.03210 | 0.03210 |
| 0.9999 | A | A | 1 | 1 | 3600 | 3600 | 0.15949 | 0.15949 | 0.99945 | 0.99945 | 0.61341 | 0.61341 |
| 0.99999 | A | A | 1 | 1 | 3600 | 3600 | 0.18531 | 0.18531 | 0.99996 | 0.99996 | 0.59946 | 0.59946 |

(c) HEAT PUMP

| α | Model | | L | | T_ϕ (sec) | | PINAW | | PICP | | CWC | |
|----------|-------|-------|----|-------|----------------|-------|---------|---------|---------|---------|---------|---------|
| | P | P+TOD | P | P+TOD | P | P+TOD | P | P+TOD | P | P+TOD | P | P+TOD |
| 0.99 | B | B | 8 | 256 | 21600 | 21600 | 0.00438 | 0.00465 | 0.99021 | 0.99078 | 0.00438 | 0.00465 |
| 0.999 | B | B | 64 | 256 | 21600 | 21600 | 0.00619 | 0.00625 | 0.99900 | 0.99908 | 0.00619 | 0.00625 |
| 0.9999 | B | B | 64 | 64 | 21600 | 21600 | 0.00803 | 0.00804 | 0.99990 | 0.99990 | 0.00803 | 0.00804 |
| 0.99999 | B | B | 1 | 1 | 86400 | 86400 | 0.01818 | 0.01818 | 0.99999 | 0.99999 | 0.01818 | 0.01818 |

(d) MV FEEDERS

that achieves the smallest value of CWC for each target confidence level. The comparison between the two cases, specifically (i) using only power level (P) and (ii) using power level and the time of day (P+TOD), is shown on Table 3.5.

We observe that the best configuration for the two clustering strategies is the same in most cases. For the office building and the MV feeders, the introduction of the TOD does not affect the value of CWC by more than 1%, which confirms once again that the clustering method does not affect the algorithm's performance. For the charging station, the value of CWC differs by 5-10% between the two clustering methods. However, introducing the new feature could either improve or worsen the performance, depending on the confidence level. Therefore, we cannot conclude whether it consistently performs better. As far as the heat pump is concerned, the usage of the TOD in the clustering does not affect the performance because the algorithm performs better when all measurements are put in one cluster. The results indicate that this feature does not play a critical role in the computation of PIs. Perhaps other features, apart from the power level and the time of day, could influence the algorithm's performance. The effect of additional features could be studied in future research.

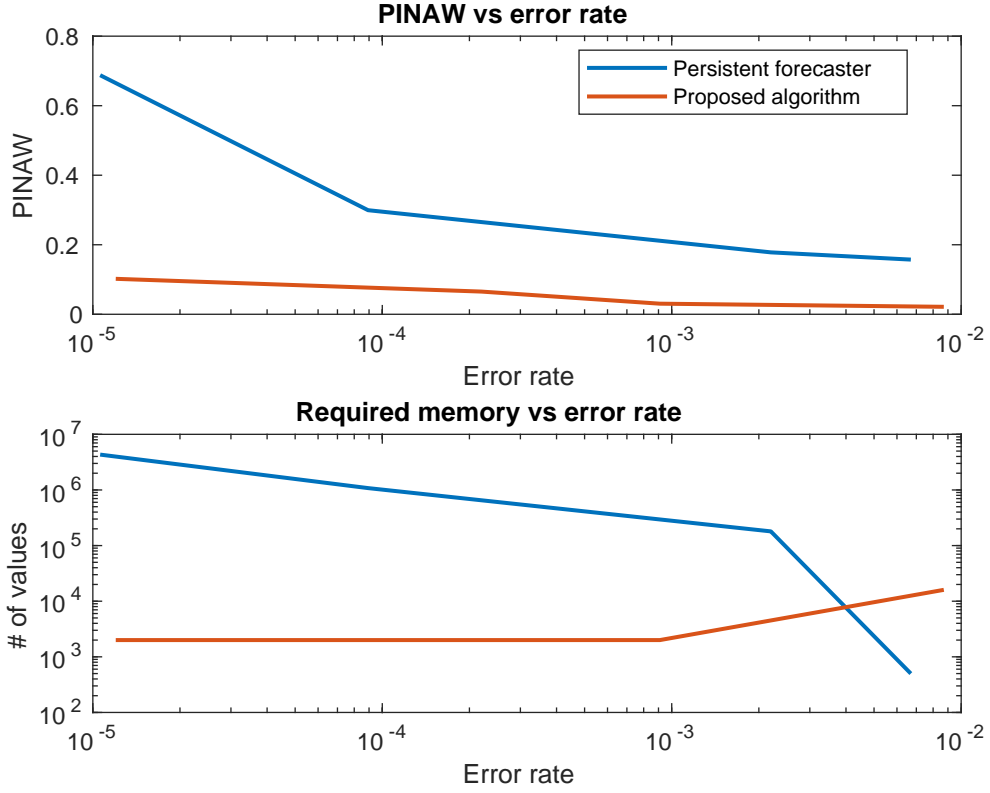


Figure 3.6: Comparison between our algorithm and a persistent forecaster for the office building.

3.3.5 Comparison with a Persistent Forecaster

To further justify the benefits of our method, we compare it with a modified version of a persistent forecaster, which has been adapted to compute PIs. We keep a history of all the measurements $\{P_{i+1-50 \cdot T_{hist}}, \dots, P_i\}$ in the past T_{hist} seconds at 20ms resolution, with T_{hist} ranging from 10s to a full day. Then, the upper and lower bounds of the PI are computed as follows:

$$P_{i+1}^l = \min \{P_{i+1-50 \cdot T_{hist}}, \dots, P_i\}, \quad (3.24)$$

$$P_{i+1}^u = \max \{P_{i+1-50 \cdot T_{hist}}, \dots, P_i\} \quad (3.25)$$

The comparison between this approach and our proposed algorithm is shown in Fig. 3.6 for the office building. Each data point shown for the persistent forecaster corresponds to the choice of T_{hist} that achieves similar values of PICP compared to those achieved by our algorithm according to the best configuration shown in Table 3.1. We notice that our algorithm achieves smaller values of PINAW for the same PICP, thus outperforming the persistent forecaster.

Moreover, our algorithm requires much less memory compared to the persistent forecaster for

high confidence levels (low error rates). This is because our algorithm only needs to store in memory the heights of the bins of each histogram. The number of bins is fixed at 2000 bins per cluster in our simulations, so the required memory does not increase for higher confidence levels. On the other hand, the persistent forecaster needs to store many more measurements if a high confidence level is desired. Notice that our algorithm requires more memory for low confidence levels, as it benefits from using more clusters for low confidence levels, according to Table 3.1. However, the clustering yields much smaller values of the PINAW, as the range of the measurements that fall within a given cluster is smaller.

3.3.6 Effect of the Measurement Period

A crucial objective of this work is to find out how the proposed algorithm scales as the measurement period increases. To test the algorithm on different measurement periods, we integrate the available data-set. In particular, given the measurements P_j^{20} , $j = 1..N$ at 20 ms resolution, the measurements at resolution T (ms) are recomputed as:

$$P_i^T = \frac{20}{T} \sum_{j=(i-1)\frac{T}{20}+1}^{i\frac{T}{20}} P_j^{20}, i = 1.. \frac{20}{T}N \quad (3.26)$$

where T is assumed to be a multiple of 20 ms. The forgetting factor ϕ is scaled according to T , as in Equation (3.13). For this and the following section, we do clustering based only on the power level.

We perform simulations again with varying cluster numbers L and forgetting time constants T_ϕ for different confidence levels. In Fig. 3.7, we plot the values of PINAW and PICP as a function of the measurement period from 20 ms up to 300 s for the three buildings considered. Each point on the graphs corresponds to a different configuration (the one that achieves the smallest CWC), as shown in Table 3.6.

The graph for the office building showcase that the algorithm performs well even for larger measurement periods provided that the target confidence level is less than 99.99%. Indeed, for low confidence levels, the error rate is kept below the target, and the average width of the PI is less than 20% of the nominal value.

For larger confidence levels, however, the algorithm fails because either the target level is not achieved or the width of the PI is so high that it becomes useless for grid control. It is worth noting that at a resolution of five minutes, the result of the algorithm is identical for all target confidence levels above 99.99%. This implies we might need a larger history to meet high confidence levels when the measurements are sparse. The same results can be deduced for the MV feeders but with much smaller relative PI widths than the office building.

Similar observations can be made for the charging station. The main difference is that the maximum measurement period with an acceptable performance depends on the target confidence

3.3 Performance Evaluation

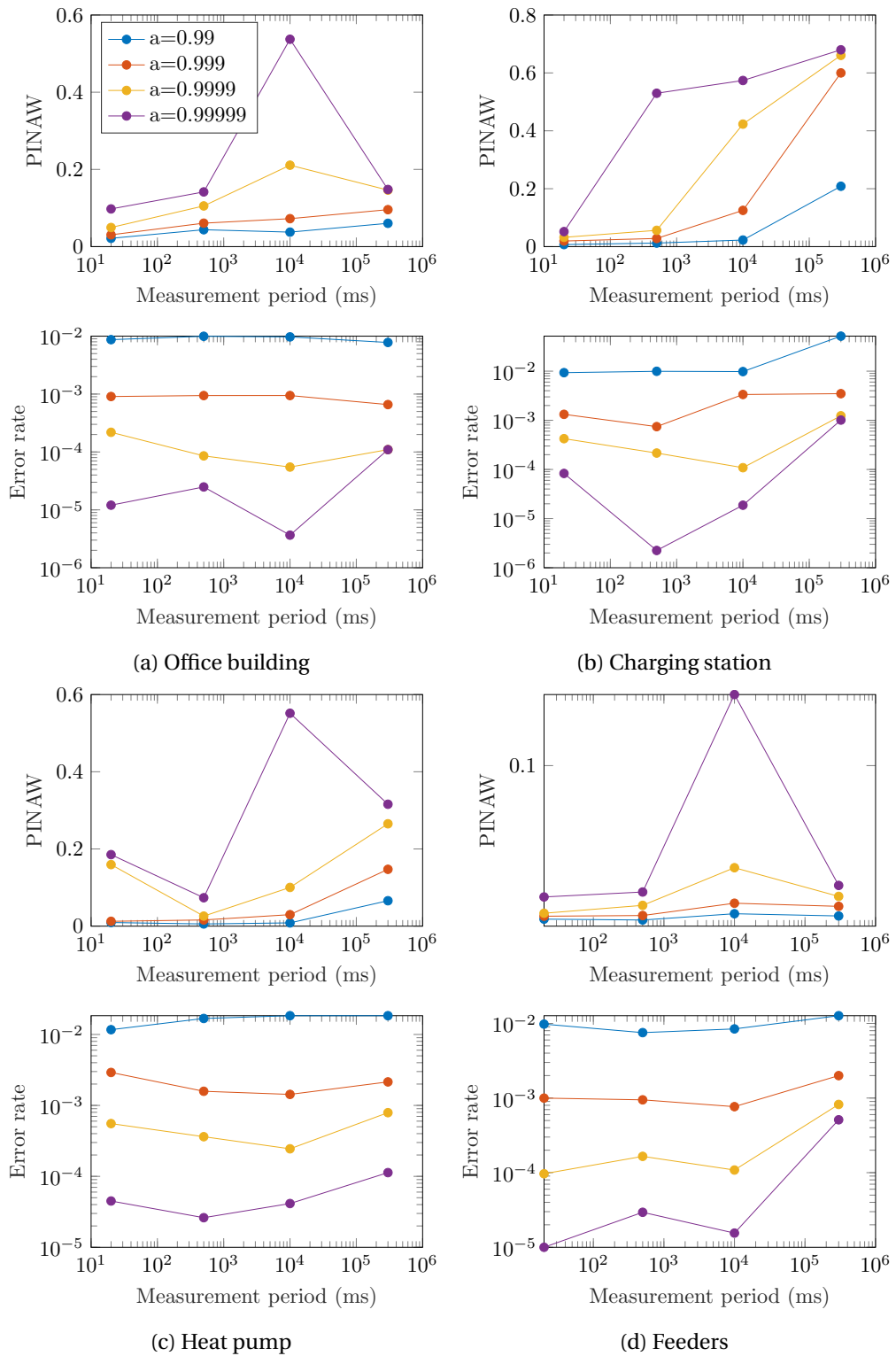


Figure 3.7: Performance evaluation as a function of the measurement period

Chapter 3. Quantification of Ultra-Short-Term Uncertainty of Heterogeneous Resources in Active Distribution Networks

Table 3.6
BEST CONFIGURATION AS A FUNCTION OF THE MEASURING PERIOD

| $T(ms)$ | α | Model | L | $T_\phi(sec)$ | $T(ms)$ | α | Model | L | $T_\phi(sec)$ |
|---------|----------|-------|-----|---------------|---------|----------|-------|-----|---------------|
| 20 | 0.99 | B | 8 | 604800 | 20 | 0.99 | B | 8 | 86400 |
| | 0.999 | B | 1 | 604800 | | 0.999 | B | 8 | 86400 |
| | 0.9999 | B | 1 | 604800 | | 0.9999 | B | 8 | 86400 |
| | 0.99999 | B | 1 | 604800 | | 0.99999 | B | 8 | 86400 |
| 500 | 0.99 | B | 1 | 21600 | 500 | 0.99 | B | 1 | 86400 |
| | 0.999 | B | 1 | 604800 | | 0.999 | B | 1 | 604800 |
| | 0.9999 | B | 1 | 86400 | | 0.9999 | B | 8 | 86400 |
| | 0.99999 | B | 1 | 21600 | | 0.99999 | A | 1 | 604800 |
| 10000 | 0.99 | B | 64 | 86400 | 10000 | 0.99 | B | 1 | 604800 |
| | 0.999 | B | 8 | 86400 | | 0.999 | B | 8 | 604800 |
| | 0.9999 | B | 1 | 604800 | | 0.9999 | B | 1 | 604800 |
| | 0.99999 | B | 1 | 604800 | | 0.99999 | B | 1 | 604800 |
| 300000 | 0.99 | B | 1 | 604800 | 300000 | 0.99 | B | 1 | 3600 |
| | 0.999 | B | 1 | 604800 | | 0.999 | B | 1 | 604800 |
| | 0.9999 | B | 1 | 604800 | | 0.9999 | B | 1 | 604800 |
| | 0.99999 | B | 8 | 604800 | | 0.99999 | B | 1 | 604800 |

(a) OFFICE BUILDING

(b) CHARGING STATION

| $T(ms)$ | α | Model | L | $T_\phi(sec)$ | $T(ms)$ | α | Model | L | $T_\phi(sec)$ |
|---------|----------|-------|-----|---------------|---------|----------|-------|-----|---------------|
| 20 | 0.99 | B | 1 | 60 | 20 | 0.99 | B | 8 | 21600 |
| | 0.999 | B | 1 | 60 | | 0.999 | B | 64 | 21600 |
| | 0.9999 | A | 1 | 3600 | | 0.9999 | B | 64 | 21600 |
| | 0.99999 | A | 1 | 3600 | | 0.99999 | B | 1 | 86400 |
| 500 | 0.99 | B | 1 | 60 | 500 | 0.99 | B | 1 | 604800 |
| | 0.999 | B | 1 | 3600 | | 0.999 | B | 1 | 86400 |
| | 0.9999 | B | 1 | 3600 | | 0.9999 | B | 1 | 3600 |
| | 0.99999 | B | 1 | 604800 | | 0.99999 | B | 1 | 604800 |
| 10000 | 0.99 | B | 8 | 604800 | 10000 | 0.99 | B | 1 | 604800 |
| | 0.999 | B | 1 | 604800 | | 0.999 | B | 1 | 604800 |
| | 0.9999 | B | 8 | 604800 | | 0.9999 | B | 1 | 604800 |
| | 0.99999 | B | 1 | 604800 | | 0.99999 | B | 1 | 604800 |
| 300000 | 0.99 | B | 1 | 21600 | 300000 | 0.99 | B | 1 | 86400 |
| | 0.999 | B | 1 | 86400 | | 0.999 | B | 1 | 604800 |
| | 0.9999 | B | 1 | 604800 | | 0.9999 | B | 1 | 604800 |
| | 0.99999 | B | 1 | 604800 | | 0.99999 | B | 1 | 604800 |

(c) HEAT PUMP

(d) MV FEEDERS

level. With target confidence of 99%, the algorithm computes a low PI width for measurement periods up to 10 s; whereas, with 99.9-99.999%, it has acceptable performance but only when the resolution is sub-second. For higher confidence, the algorithm cannot predict accurate PIs for periods larger than 20 ms.

Looking at the results for the heat pump in Fig. 3.7, we notice a break in the trend of increasing PINAW. To understand why this happens, we look at Table 3.6c. The best configuration for confidence levels 99.99-99.999% changes from using model A at 20 ms resolution to model B at higher resolutions. Model A has been shown in Section 3.3.3 to generate, in general, larger PIs than model B. This increase in the width results in a lower error rate, which in turn might reduce the value of CWC, which is the sole metric used to compare configurations to one another. The value of CWC ultimately depends on the choice of the parameter μ , which might affect the trends in the graphs of Fig. 3.7.

3.3.7 Confidence Level Uncertainty

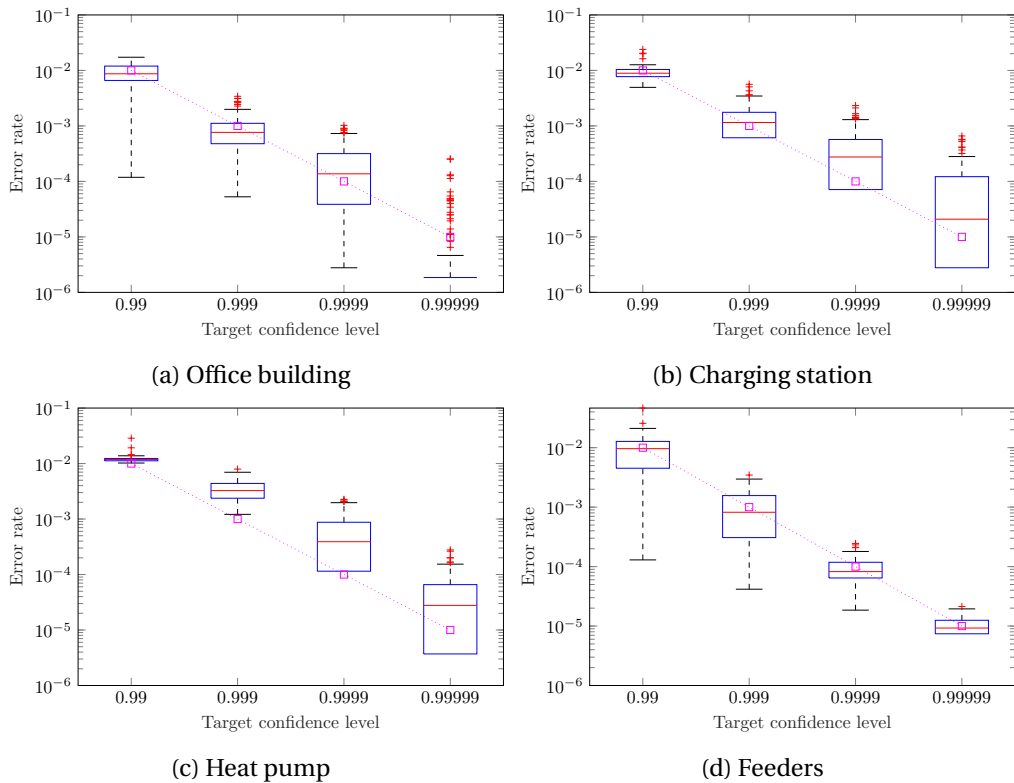


Figure 3.8: Box plot of model accuracy versus target confidence level at 20 ms resolution

The metrics of Section 3.3.2 evaluate the algorithm’s average performance over the full one-month period. However, it would be interesting to see how the algorithm performs over time. For this purpose, we split the one-month evaluation period (15 days for the MV feeders) into six-hour windows and compute the error rate the algorithm achieves in each window. Hence,

Chapter 3. Quantification of Ultra-Short-Term Uncertainty of Heterogeneous Resources in Active Distribution Networks

we compute a estimations 60 for the MV feeders) of the error rate for each confidence level. We then depict the statistical measures of the histograms using the box plots of Fig. 3.8. The blue box indicates the 25th and 75th percentiles, the red line is the median, the red crosses are outliers, and the small square indicates the target error rate. We computed the box plots only for the best configuration for each building and for confidence level at resolution, which are shown in Table 3.6.

If the algorithm is consistent in predicting accurate PIs, then the median of the box plot should be close to the target error-rate. We see that this is indeed the case for the office building. Our algorithm performs even better than expected for the largest confidence level, albeit with many outliers. The performance of the charging station is sometimes worse than expected, but the target error-rate is nevertheless contained within the box plot's 25th and 75th percentile. This is not always the case for the heat pump, hence the algorithm cannot consistently estimate accurate PIs if there is high volatility in the measurements. Finally, the case of the MV feeders is once again the best-performing out of the four, as the median of all box plots is very close to the target level.

The results showcase that our algorithm computes accurate PIs, irrespective of the prosumer, provided that the target confidence level is less than 99.9%. The performance is still acceptable for higher confidence levels, but the predictions' consistency depends on the node's dynamics.

3.4 Conclusion

Motivated by the requirements of ADNs real-time control, we have presented a non-parametric method for computing ultra-short-term PIs of the power prosumption in generic ADNs. The method's performance was tested for different types of prosumers using experimental measurements from an MV distribution network. The performance analysis enabled us to make an a-posteriori selection of the algorithm's parameters. The algorithm was shown to compute relatively narrow PIs for the studied prosumers, for time resolutions from 20 ms up to a few minutes in some cases, provided that the target confidence level is below 99.9%.

In the rest of the thesis, we exploit the proposed algorithm to compute PIs for various control frameworks. In Chapter 4, we revisit the problem of objective balancing introduced in Chapter 2 and propose a method for designing cost functions of RT optimization problems. The method adaptively computes the weights of the various grid objectives (see Sections 2.2 and 2.3) according to the measured grid state and the uncertainties in the grid. In particular, the weights of objectives that reflect hard grid constraints on the nodal voltages and branch currents are adapted to the uncertainty of the respective voltage or current to ensure that the constraint will be satisfied in the worst case.

In Chapter 5, we use our proposed PI-computation algorithm in two control frameworks. In Section 5.2, we use the COMMELEC framework proposed in [7, 8] to achieve RT dispatch-plan tracking in a utility-scale grid. COMMELEC is designed to make decisions as fast as every

100 ms, which makes it the ideal application for our proposed PI-computation algorithm. Finally, in Section 5.3, we propose a two-layer control approach for the fair control of BESSs, which uses the cost functions of Chapter 4 and the algorithm of this chapter to ensure dispatch tracking, grid safety and SoC fairness in the long-run. The proposed framework is experimentally validated in a subset of the EPFL smart-grid platform.

4 Design of Cost Functions for the Fair Control of Battery Energy Storage Systems

4.1 Purpose of Chapter

As we have seen in Chapter 2, the decisions made by the RT layer depend on the configuration of the weights of the controller in Problem (2.12). We have shown that determining such a configuration is an issue, as there is no good choice that fits all operating conditions.

In this chapter, we propose a method (published in [97]) to automatically compute the weights of the various objectives to achieve a balanced satisfaction of the objective, irrespective of the scenario and the topology to which it is applied. The method removes the weights entirely by constructing appropriate cost functions or translates them into parameters that can be configured intuitively, thus removing the trial-and-error method used in other approaches.

We propose guidelines for choosing cost functions for two types of objectives, namely battery and grid objectives, as defined in Section 2.2.1. In Section 4.2, we give a proposed design goal for the RT control leading to a generalized battery objective form. The goal is to ensure a fair regulation of the BESS's SoCs under normal operating conditions. In Section 4.3, we give the properties that the generalized grid cost-function defined in (2.8) should meet, and we derive an algorithm to compute the respective weights. The proposed algorithm requires specific parameters as input that the user can configure intuitively.

The value of the proposed method is demonstrated via simulations in the examples of Section 2.4. Our method yields results similar to the oracle-based approach, with the added benefit of being scenario and topology-independent. The method is finally employed in another use case in the literature to showcase its applicability.

4.2 Battery Cost Function

4.2.1 Fair Control of Batteries

The battery objectives should be chosen in such a way that fair control among them is achieved in order to follow the grid objective. To achieve fairness, we first need to choose a proper fairness criterion. As discussed in Section 2.1.4, fairness in RT control of BESSs means that their SoCs should be as close as possible to each other, as long as the grid's operational constraints allow it. However, achieving long-term SoC balance with the RT control is not easy because of the short optimization horizon. Therefore, our definition of fairness should apply to the short-term objectives considered. Moreover, the chosen fairness condition should be satisfied without tuning weights to avoid the problems of the oracle-based approach. These requirements lead us to the following methodology for choosing a proper battery cost-function.

BESS Design Goal and Preference of BESSs

As already explained in Section 2.4.1, a BESS's capability curve can typically be approximated by a rectangle. We assume that a higher layer of control has computed a point for BESS i within this capability curve, called the *preference* of the BESS, as follows:

$$\mathbf{x}_i^*(SoC_i) = (P_i^*(SoC_i), Q_i^*(SoC_i)) \in \left[-\frac{S_i}{\sqrt{2}}, \frac{S_i}{\sqrt{2}}\right] \times \left[-\frac{S_i}{\sqrt{2}}, \frac{S_i}{\sqrt{2}}\right]$$

It is the point that the BESS should implement if the grid does not impose any other constraints. Taking the example studied in Section 2.4, the preference would be the power setpoint that brings the SoC of the BESS as close to the target value as possible.

However, because there might be conflicting objectives on the grid, the BESSs might not be able to implement their preference simultaneously. The deviation of a BESS's implementation from its preference can be measured using its *preference ratios* that, with respect to P and Q , are defined as:

$$\begin{aligned} r_{P,i} &:= \frac{P_i^{opt} - P_i^*}{S_i} \\ r_{Q,i} &:= \frac{Q_i^{opt} - Q_i^*}{S_i} \end{aligned} \tag{4.1}$$

where (P_i^{opt}, Q_i^{opt}) is the solution of the convex Optimization Problem (2.12) for BESS i .

Because the energy capacities of the BESSs are typically proportional to their rated power and assuming that the preferences of the BESSs relative to their rated power are designed to be equal, equal preference ratios would maintain SoC balance. Therefore, a possible choice for a fairness condition for the RT control would be an equal preference ratio for all BESSs, as is achieved, for example, in [55].

However, the primary goal of the BESSs is to follow the grid objective, which means the impact of the BESSs on the grid objective should also be considered in our fairness criterion. In particular, BESSs with a higher impact in controlling the grid objective should be used for this purpose even if that contradicts their preference. For example, BESSs in nodes further away from the feeder have a higher impact on the nodal voltages, so they should be used more for voltage control. If instead, we aimed for perfect SoC balance in this case, then the voltage control would not be as effective, because the flexibility of the control would be limited.

Considering these desirable features, we define as *fairness* the condition where the preference ratio of a BESS is proportional to the effect this BESS has on minimizing the grid objective. Formally, our fairness condition is $\forall i = 1, \dots, N_B$:

$$\begin{aligned} r_{P,i} &= \lambda_P \frac{\partial J(\mathbf{x}^{opt} | \hat{\mathbf{u}})}{\partial P_i} \\ r_{Q,i} &= \lambda_Q \frac{\partial J(\mathbf{x}^{opt} | \hat{\mathbf{u}})}{\partial Q_i} \end{aligned} \quad (4.2)$$

where the coefficients λ_P and λ_Q are the same for all BESSs.

This means that BESSs that can easily affect the grid objective should be exploited for this purpose, assuming that this is achievable by the BESS's capabilities, even if this contradicts their own preference. Whereas, if the choice of the power setpoint for a specific BESS does not affect the grid objective, then we can freely choose to satisfy the preference of the BESS (both sides of Equations (4.2) are 0).

Note that this definition of fairness does not contradict the definition we have discussed so far, which is equivalent to SoC balancing. The RT control gives higher priority to the grid objective, whereas SoC balancing is a secondary objective, which is achieved provided that the impacts of the BESSs on the grid objective are the same. This is typically the case where the voltage and current constraints are not binding, as we will verify in the simulations of Section 4.4.2.

4.2.2 General Form of a Battery Cost Function

We assume that each BESS has two separate objectives, specifically (i) satisfy its own preference and (ii) minimize the internal losses of the hardware interface that interconnects the BESS with the grid. The first objective can be met by steering the stationary point of the cost, whereas the second can be achieved with the addition of a quadratic penalty function of the active and reactive powers. Therefore, we consider the following cost function for BESS i :

$$C_i(P_i, Q_i | S_i, SoC_i) = a_P \left(\frac{P_i^2}{4S_i} - \frac{P_i^*(SoC_i)}{2S_i} P_i \right) + a_Q \left(\frac{Q_i^2}{4S_i} - \frac{Q_i^*(SoC_i)}{2S_i} Q_i \right) + c \quad (4.3)$$

Chapter 4. Design of Cost Functions for the Fair Control of Battery Energy Storage Systems

where a_P, a_Q are strictly positive so that the function is strictly convex and c is any arbitrary constant¹. By defining the function this way, one can verify that the point that minimizes it is precisely the preference of the BESS. Theorem 4.1 shows that this cost function satisfies our definition of fairness under certain conditions.

Theorem 4.1. *We consider the unconstrained variant of Problem (2.6), i.e. with $\mathcal{A}_i = \mathbb{R}^2, i = 1, \dots, N_B$ where the cost function for all N_B BESSs is defined in (4.3). Then the optimal solution of the problem satisfies Conditions (4.2) with $\lambda_P = -\frac{2}{a_P}$ and $\lambda_Q = -\frac{2}{a_Q}$.*

Proof. Because the optimization problem is assumed to be unconstrained, the optimal solution would be a stationary point of the cost function. This means that for every BESS i we should have:

$$\frac{\partial C_t(\mathbf{x}^{opt}|\hat{\mathbf{u}})}{\partial P_i} = \frac{\partial C_t(\mathbf{x}^{opt}|\hat{\mathbf{u}})}{\partial Q_i} = 0 \quad (4.4)$$

From the form of the total Cost-Function (2.7) and the battery Cost-Function (4.3), we have the following set of equations $\forall i = 1, \dots, N_B$:

$$\begin{aligned} \frac{\partial C_t(\mathbf{x}^{opt}|\hat{\mathbf{u}})}{\partial P_i} &= a_P \frac{r_{P,i}}{2} + \frac{\partial J(\mathbf{x}^{opt}|\hat{\mathbf{u}})}{\partial P_i} \\ \frac{\partial C_t(\mathbf{x}^{opt}|\hat{\mathbf{u}})}{\partial Q_i} &= a_Q \frac{r_{Q,i}}{2} + \frac{\partial J(\mathbf{x}^{opt}|\hat{\mathbf{u}})}{\partial Q_i} \end{aligned} \quad (4.5)$$

where $r_{P,i}$ is defined in (4.1). Given the sets of Equations (4.4) and (4.5), we get Equations (4.2) with $\lambda_P = -\frac{2}{a_P}$ and $\lambda_Q = -\frac{2}{a_Q}$, which is the statement of the theorem. \square

Theorem 4.1 states that fairness is guaranteed provided that the BESSs have unconstrained setpoints. We now study how much we can deviate from ideal fairness, when the BESS constraints are involved, in the following scenario: we consider two BESSs $i, j \in \{1, \dots, N_B\}$ that (i) have the same preference, normalized by the rated power:

$$\frac{\mathbf{x}_i^*(SoC_i)}{S_i} = \frac{\mathbf{x}_j^*(SoC_j)}{S_j} \quad (4.6)$$

and (ii) have the same constraints, normalized by the rated power, which are in the following form, for $m \in \{i, j\}$:

$$\begin{aligned} \frac{P_m}{S_m} &\in [(\frac{P}{S})_{min}, (\frac{P}{S})_{max}] \\ \frac{Q_m}{S_m} &\in [(\frac{Q}{S})_{min}, (\frac{Q}{S})_{max}] \end{aligned} \quad (4.7)$$

It should be noted that it is reasonable to assume that Conditions (4.6) and (4.7) are satisfied simultaneously because (i) the capability curves of BESSs can be accurately approximated by a rectangle [92], (ii) BESSs that have the same constraints should have the same objective, and

¹It should be noted that the value of c does not affect the solution of the Optimization Problem (2.12)

(iii) the preference can be designed in such a way that the conditions are satisfied. Theorem 4.2 is a generalization of Theorem 4.1, when the binding constraints of the BESSs are considered.

Theorem 4.2. *We consider Problem (2.6), where the cost function for all N_B BESSs is defined in (4.3). We also consider two BESSs $i, j \in \{1, \dots, N_B\}$, for which Conditions (4.6) and (4.7) are true. Then the solution of Optimization Problem (2.6) satisfies the following conditions:*

$$|r_{P,i} - r_{P,j}| \leq \frac{2}{a_P} \left| \frac{\partial J(\mathbf{x}^{opt} | \hat{\mathbf{u}})}{\partial P_i} - \frac{\partial J(\mathbf{x}^{opt} | \hat{\mathbf{u}})}{\partial P_j} \right| \quad (4.8)$$

$$|r_{Q,i} - r_{Q,j}| \leq \frac{2}{a_Q} \left| \frac{\partial J(\mathbf{x}^{opt} | \hat{\mathbf{u}})}{\partial Q_i} - \frac{\partial J(\mathbf{x}^{opt} | \hat{\mathbf{u}})}{\partial Q_j} \right| \quad (4.9)$$

where $r_{P,m}, r_{Q,m}, m \in \{i, j\}$ are defined in (4.1). The upper bound is achieved under the assumptions of Theorem 4.1.

The proof of the theorem is in the appendix. Theorem 4.2 states that the conditions of Theorem 4.1 are sufficient to achieve the upper bound of the differences $|r_{P,i} - r_{P,j}|$ and $|r_{Q,i} - r_{Q,j}|$. This means that adding constraints to the problem will definitely reduce the difference in the preference ratios compared to the unconstrained case. Because the upper bounds of Conditions (4.8) and (4.9) correspond to our definition of fairness (Condition (4.2)), the worst case, in terms of fairness, is the one where the preference ratios are equal. Therefore, Cost Function (4.3) always achieves a state between our fair condition and the one used in [55]. Moreover, the theorem gives some intuition on the effect that the coefficients a_P, a_Q have on the fairness between the two BESSs. It shows, in particular, how increasing the weights of the cost terms causes an inversely proportional decrease in the difference between the respective preference ratios.

Regarding the value of the coefficients a_P, a_Q , when choosing the weights of the various cost functions, we first need to choose the weights of one cost arbitrarily. Moreover, because conditions 4.2 need to be satisfied independently for the active and reactive power, we can freely choose these coefficients at $a_P = a_Q = 1$. The weights for the rest of the objectives are chosen according to the method presented in Section 4.3.

It should be noted that Theorem 4.2 applies only under the assumption that the constraint set of a BESS is a box in the P-Q plane. Although this is a limiting factor of the provided analysis, the mathematical formulation is still useful for practical applications, because (i) BESSs should not typically operate on the boundary of their constraints (hence the assumptions of Theorem 4.2 are valid) and (ii) the constraint sets of realistic BESSs can be efficiently approximated by a box.

4.3 Grid Objective

The purpose of the grid objective is to achieve a target grid state. Assuming grid cost-functions in the form of Equation (2.8), we define the *preference* y_m^* of grid variable y_m , as $y_m^* := \arg \min_{y_m} J_{y_m}(y_m)$. In many practical applications, a deviation Δy_m from the target value y_m should be penalized the same as a deviation $-\Delta y_m$. In this case, we require that J_{y_m} is in the following form:

$$J_{y_m}(y_m) = J_{y_m}^*(y_m - y_m^*) \quad (4.10)$$

where $J_{y_m}^*(y)$ is a strictly convex, even function of y .

4.3.1 Computing the Weights w_{y_m}

We propose a method for choosing the weight w_{y_m} of objective J_{y_m} that is independent of the state of the BESSs connected to the grid. We assume that we use a cost function in the form of Equation (4.3) for every BESS. As we saw in Section 2.4.2, we first need to fix one weight in the controller and then compute the rest relative to it. Because we started by defining the battery objective, and the active and reactive power objectives are independent, we can freely choose $a_P = a_Q = 1$.

Grid Design-Goal

A typical purpose of any grid objective J_{y_m} would be to keep the difference of grid variable y_m from its target value y_m^* within a specified bound $d_{max,m}^*$. Therefore, the weight w_{y_m} should be chosen, such that

$$|y_m^{opt} - y_m^*| \leq d_{max,m}^* \quad (4.11)$$

where $y_m^{opt} = y_m(\mathbf{x}^{opt} | \hat{\mathbf{u}})$ is the value of y_m when the optimal solution of Problem (2.6) is implemented. Lemma 4.1 computes an upper bound for $|y_m^{opt} - y_m^*|$ as a function of the weight w_{y_m} , which will be proven useful in achieving Condition (4.11).

Lemma 4.1. *We assume a grid cost-function of the form: $J(\mathbf{x}|\mathbf{u}) = w_{y_m} J_{y_m}(y_m(\mathbf{x}|\mathbf{u}))$ where $J_{y_m}(y_m)$ is a strictly convex function of the grid variable y_m expressed in the form of Equation (2.11). We also assume that the constraints of the BESSs are in the form $x_i \in [x_{i,min}, x_{i,max}]$, $\forall i = 1, \dots, N_B$, where $x_i = \{P_i, Q_i\}$. We define the following functions:*

$$K_t(w_{y_m}, d) = \frac{1}{w_{y_m} J'_{y_m}(y_m^* + d)} \quad (4.12)$$

$$h(K) = |y_m^* - y_m^{inf}| + \sum_{|K_{x_i}^m| < K} |K_{x_i}^m| |x_{i,max} - x_{i,min}| \quad (4.13)$$

$$g(w_{y_m}, d) = \max\{d, h(K_t(w_{y_m}, d))\} \quad (4.14)$$

$$f(w_{y_m}) = \min_{d>0} g(w_{y_m}, d) \quad (4.15)$$

where w_{y_m} is the weight of objective $J_{y_m}(y_m)$, $J'_{y_m}(y_m)$ is the derivative of J_{y_m} with respect to y_m and y_m^{inf} is the point that minimizes J_{y_m} within its domain², i.e. $y_m^{inf} := \underset{y_m \in [y_m^{min}, y_m^{max}]}{\operatorname{argmin}} J_{y_m}(y_m)$.

Then, the function $f(w_{y_m})$ is an upper bound of $|y_m^{opt} - y_m^*|$.

The proof of the lemma is in the appendix. It should be noted that functions K_t , h and g defined in (4.12), (4.13) and (4.14) respectively are just auxiliary functions that help in the proofs of the theorems and the visualization of the upper bound, as will be shown in Section 4.3.3. K_t can be interpreted as a threshold, under which the values of the sensitivities are negligible in computing the upper bound for $|y_m^{opt} - y_m^*|$.

Lemma 4.1 gives an upper bound for the quantity $|y_m^{opt} - y_m^*|$ as a function of the weight w_{y_m} . However, the actual realization y_m^{real} will differ from the optimal value y_m^{opt} , because of the uncertainty in the system, as follows:

$$y_m^{real} = y_m^{opt} + \Delta y_m \quad (4.16)$$

$$\Delta y_m = \sum_{n=1}^U (K_{\mathcal{P},n}^m \Delta \mathcal{P}_n + K_{\mathcal{Q},n}^m \Delta \mathcal{Q}_n) \quad (4.17)$$

where $\Delta \mathcal{P}_n$, $\Delta \mathcal{Q}_n$ are the uncertainties of prosumption n , i.e., the difference between the forecast value and the respective realization, and $K_{\mathcal{P},n}^m$, $K_{\mathcal{Q},n}^m$ are the sensitivity coefficients of y_m with respect to the nodal prosumption (see Section 2.2.2 and [83]).

For certain grid variables, we are interested in computing a more robust upper bound that would consider the maximum uncertainty in the grid. This is highly important, especially when considering constraints in nodal voltages and branch currents, as those should be strictly kept within some given bounds. The idea is that if there is high forecast uncertainty for a given grid variable, the weight of the respective objective should be increased to ensure that the variable will be kept within the desired bounds for any future realization of the stochastic power injections³. For this purpose, Theorem 4.3 extends the statement of Lemma 4.1 by computing an upper bound for the quantity $|y_m^{real} - y_m^*|$ as a function of the objective's weight w_{y_m} .

Theorem 4.3. *Given the same assumptions as Lemma 4.1 and Equation (4.16), then*

$$|y_m^{real} - y_m^{opt}| \leq f(w_{y_m}) + |\Delta y_m|_{max} \triangleq f_u(w_{y_m}) \quad (4.18)$$

where $|\Delta y_m|_{max} = \max_{\mathcal{P}_n, \mathcal{Q}_n} |\Delta y_m|$ is the maximum absolute uncertainty of y_m due to the forecast errors and $f(w_{y_m})$ is given by (4.15).

²In contrast, y_m^* is the value that minimizes the function J_{y_m} assuming y_m is unconstrained, i.e., $y_m^* := \underset{y_m \in [-\infty, \infty]}{\operatorname{argmin}} J_{y_m}(y_m)$

³This is equivalent to a robust optimization problem.

Chapter 4. Design of Cost Functions for the Fair Control of Battery Energy Storage Systems

Proof. By taking Definition (4.16) and applying the triangle inequality we get

$$\begin{aligned} |y_m^{real} - y_m^*| &= |y_m^{opt} - \Delta y_m - y_m^*| \leq \\ &\leq |y_m^{opt} - y_m^*| + |\Delta y_m| \leq \\ &\leq |y_m^{opt} - y_m^*| + |\Delta y_m|_{max} \end{aligned} \quad (4.19)$$

and from Lemma 4.1, we have

$$|y_m^{opt} - y_m^*| \leq f(w_{y_m}) \quad (4.20)$$

Combining the above two conditions, we get the statement of the theorem. \square

Now that we have computed an upper bound for $|y_m^{real} - y_m^{opt}|$ as a function of the weight w_{y_m} , we need to address the reverse problem. That is, given a desired upper bound $d_{max,m}^*$, we need to compute:

$$\min w_{y_m} > 0 \text{ such that } f_u(w_{y_m}) \leq d_{max,m}^* \quad (4.21)$$

Even though numerical methods can be used to approximate the solution of Problem (4.21), we demonstrate below that we can find an analytical solution to the problem. To do this, we need to use the following properties of $f_u(w_{y_m})$.

1. It is a decreasing function of w_{y_m} . This makes sense as increasing the weight should result in a lower upper bound for the objective satisfaction.
2. It has an upper bound given by:

$$f_{UB} = |y_m^* - y_m^{inf}| + \sum_{\forall i} |K_{x_i}^m| |x_{i,max} - x_{i,min}| + |\Delta y_m|_{max}$$

This means that if the desired upper bound $d_{max,m}^*$ is larger than f_{UB} , then the weight could take any value

3. It has a lower bound given by:

$$f_{LB} = |y_m^* - y_m^{inf}| + |\Delta y_m|_{max}$$

Therefore, there is a limit on the tolerance of the objective, as the desired upper bound cannot be arbitrarily small.

4. If $f_{LB} \neq 0$, then:

$$f_u(w_{y_m}) = f_{LB}, \forall w_{y_m} \geq \frac{1}{|K^m|_{min} |J'_{y_m}(y_m^{inf})|}$$

where $|K^m|_{min} = \min_{x_i} |K_{x_i}^m|$. This gives an upper bound for the choice of the weight w_{y_m} as larger values would not decrease the upper bound guarantee any further.

The statement of Theorem 4.4 is used to analytically find the solution of Problem (4.21).

Theorem 4.4. We consider the following two problems, **Problem 1** given by (4.21) and **Problem 2** given by (4.22):

$$\begin{aligned} \min w_{y_m} > 0 \text{ such that} \\ g(w_{y_m}, d_{max,m}^* - |\Delta y_m|_{max}) \leq d_{max,m}^* - |\Delta y_m|_{max} \end{aligned} \quad (4.22)$$

If $w_{y_m}^*$ is the solution to Problem 2 (if it exists), then it is also the solution to Problem 1.

The proof of the theorem is in the appendix. Theorem 4.4 states that to find the solution of the original Problem 1, we could instead solve the equivalent Problem 2. The value of this statement lies in the fact that the constraint of Problem 2 can be easily evaluated, unlike the constraint of Problem 1. Indeed, given the definitions of functions g and h one can see that the function $g(w_{y_m}, d_{max,m}^* - |\Delta y_m|_{max})$ is a step-value function of w_{y_m} , while on the other hand $f_u(w_{y_m})$ is a complicated, smooth function. This means that only a finite number of evaluations is needed to compute the optimal weight. Considering Theorem 4.4 and the properties of $f(w_{y_m})$ given above, we have the following formula for computing w_{y_m} :

$$w_{y_m} = \begin{cases} 0 & \text{if } d_{max,m}^* > f_{UB} \\ \frac{1}{|K^m|_{min} |J'_{y_m}(y_m^{inf})|} & \text{if } d_{max,m}^* < f_{LB} \\ \frac{1}{K_t^m |J'_{y_m}(y_m^* + d_{max,m}^* - |\Delta y_m|_{max})|} & \text{else} \end{cases} \quad (4.23)$$

where $K_t^m = \max K$ such that $h(K) < d_{max,m}^*$. The explanation is the following: if the desired upper bound $d_{max,m}^*$ is larger than the upper bound of f_u , then we can freely choose $w_{y_m} = 0$, as any weight would satisfy the desired upper bound. Whereas, if it is lower than the lower bound of f_u , then Problems 1 and 2 cannot be solved, so we choose the maximum possible value of the weight. In any other case, Theorem 4.4 applies, so we can compute the weight by solving Problem 2. The solution is trivial as $g(w_{y_m}, d)$ takes only a finite number of values for a given d .

Concerning the complexity of computing the weight, Formula (4.23) requires at most evaluating the function J'_{y_m} at a given point and computing either the minimum or the maximum value of the sensitivity coefficients of grid variable y_m . The number of sensitivities of one grid variable scales linearly with the number of buses, so the complexity of the method for one grid objective is $\mathcal{O}(K)$, where K is the number of buses in the grid. If M grid variables are considered, then the complexity of the method is $\mathcal{O}(M \cdot K)$.

The properties of $f_u(w_{y_m})$ also give a rule for choosing $d_{max,m}^*$. According to the definition of $f_u(w_{y_m})$, it is obvious that $d_{max,m}^*$ should not be smaller than $|\Delta y_m|_{max}$, otherwise Problem (4.21) will be infeasible. Therefore, we should ensure that $d_{max,m}^* > |\Delta y_m|_{max}$. In low-voltage grids, we can assume that in the absence of abrupt changes (e.g., faults), the values of the sensitivities do not change significantly. Therefore, we can approximate the value of $|\Delta y_m|_{max}$ by using the values of the sensitivities computed every few minutes.

4.3.2 Application to Specific Grid Objectives

We now examine how the weight computation method presented in Section 4.3.1 can be applied to the grid objectives defined in Section 2.3. All grid cost-functions considered so far (see Section 2.3) can be expressed in the form of Equation (4.10), hence their weights can be computed using Theorems 4.3 and 4.4.

The target values of the slack objectives (2.14) and (2.15) are $P_s^* = P^{DP}$ and $Q_s^* = 0$. The respective desired upper bounds, used to compute the weights w_{P_s} and w_{Q_s} , can be interpreted as $d_{max, P_s}^* = |P_s - P^{DP}|_{max}$ and $d_{max, Q_s}^* = |Q_s|_{max}$, i.e. they are the maximum desired dispatch tracking difference and maximum slack reactive power respectively.

Concerning the voltage objective (2.16), we define, in addition to the hard voltage constraint β_{hard} , the soft voltage constraint β_{soft} . The soft voltage constraint guarantees that V_k will not deviate more than β_{soft} from the nominal voltage V_n , assuming that the assumptions of Theorem 4.3 are true. Therefore, it can be used to compute the weight of the objective with $V_k^* = V_{nom}$ and $d_{max, V_k}^* = \beta_{soft}$. Intuitively, the controller is expected to react to voltage deviations larger than β_{soft} . The reaction will be more drastic as the voltage approaches β_{hard} . For example, as long as all voltages are well within β_{soft} units from the nominal value, then the controller will guarantee dispatching with the desired tolerance. However, as some voltage deviation approaches β_{soft} dispatching might be compromised to ensure grid safety.

Similarly, for the current objective, we define the soft current constraint for line l as $I_l^{soft} = \gamma_{soft} I_l^{max}$, where $\gamma_{soft} \in (0, 1 - \epsilon)$, $\epsilon > 0$ is a given constant that defines a soft upper bound for each line. This bound can be used to compute the weights w_{I_l} , with $(I_l^{+/-})^* = 0$ and $d_{max, I_l^{+/-}}^* = I_l^{soft}$. The intuition of γ_{soft} is the same as β_{soft} for the voltages, meaning that the controller will start reacting when a branch current I_l gets close to $\gamma_{soft} I_l^{max}$.

It should be noted that the method can be used to design other grid objectives, for example, to minimize the system's losses. For each objective needed, it is up to the user to configure the target value and the desired tolerance according to the desired behavior. We hope the examples provided in this section will be useful for designing other objectives in the future.

4.3.3 Visual Representation of the Computed Upper Bound

To help us visualize the results from the past sections, we consider an instance of the grid shown in Fig 2.8. The preference of each BESS is $\mathbf{x}_i^* = (S_i (W), 0 (Var))$, $i = \{1, 2\}$ and the coefficients of the battery cost-function are $a_P = a_Q = 1$. We assume that Cost Function (2.14) is the single grid-cost so that the assumptions of Theorem 4.3 are valid, with a target value $y_m^* = P^{DP} = -20$ kW. The forecast power to be generated by the PV is $\hat{\mathcal{P}}_{pv} = 30$ kW, the forecast consumption of the load is $\hat{\mathcal{P}}_{load} = -15$ kW, and their reactive power is assumed to be 0. The uncertainty in the slack power is assumed to be equal to the maximum value $\Delta y_m = |\Delta y_m|_{max} = 2$ kW.

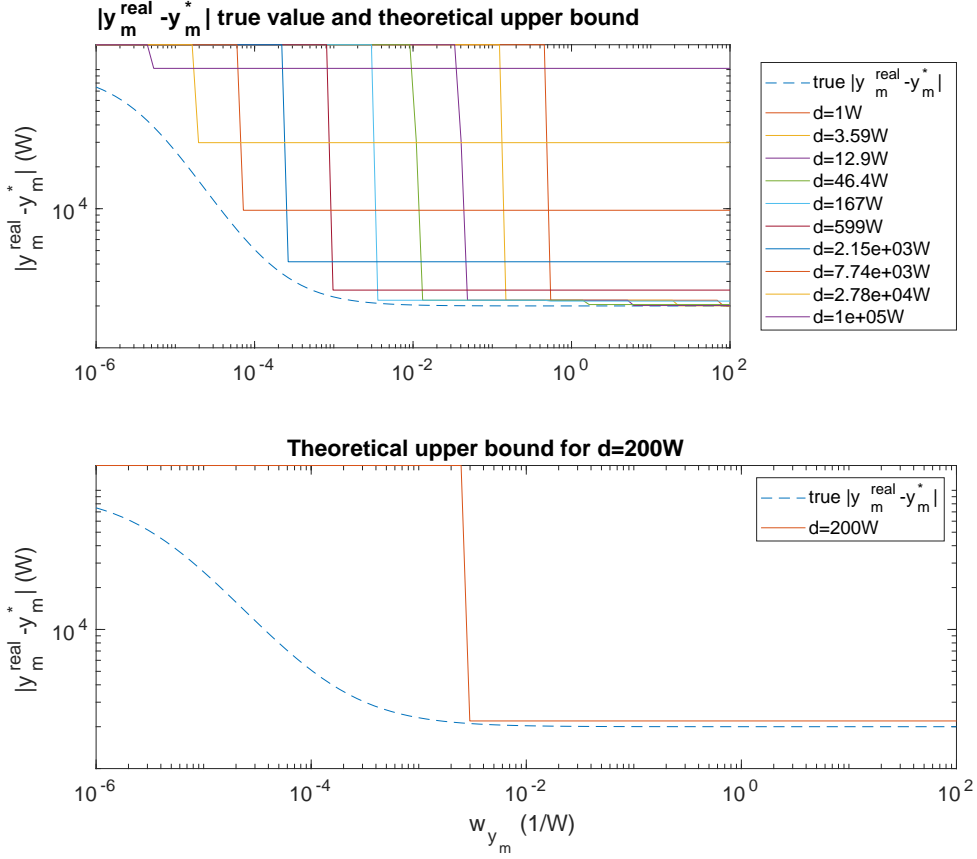


Figure 4.1: True value of $|y_m^{\text{real}} - y_m^*|$ and theoretical upper bound as a function of the weight w_{y_m} , for different values of d . The curve corresponding to the desired upper bound is the one for $d = d_{\text{max},m}^* - \Delta|y_m|_{\text{max}} = 200$ W and is shown in the bottom plot.

Fig. 4.1 shows the value of $|y_m^{\text{real}} - y_m^*|$ obtained by solving the linearized optimization problem and the theoretical upper bound computed from Theorem 4.3 as a function of the weight w_{y_m} for different values of d taken from a logarithmic space between 1 W and 100 kW. Each continuous line represents one function $g(w_{y_m}, d)$, as defined in (4.14).

Now we assume that the desired upper bound for the tracking difference $|P_s - P^{DP}|$ is $d_{\text{max},P_s}^* = 2.2$ kW (larger than $|\Delta y_m|_{\text{max}}$). According to Theorem 4.4, to compute the optimal weight, we need to consider only the function $g(w_{y_m}, d_{\text{max}}^* - |\Delta y_m|_{\text{max}})$, as shown separately in Fig. 4.1 (bottom graph). The optimal weight is the smallest one that gives $g(w_{y_m}, 200 \text{ W}) = 200 \text{ W} + |\Delta y_m|_{\text{max}}$, as computed by (4.23). In this graph, the optimal weight is the one for which the step occurs in the orange line in the bottom graph, i.e., approximately $3 \cdot 10^{-3}$.

4.3.4 Multiple Objectives

The method presented in Section 4.3.1 is only useful when the grid objective reflects a single grid variable. Practical applications, however, would typically involve multiple of such objectives. In the problem studied in this thesis, the computation of the total grid objective is based on certain heuristics. The individual objectives are the following: (i) slack-active-power cost, (ii) slack-reactive-power cost, (iii) average voltage cost of nodes, and (iv) average current cost of lines.

The first heuristic concerns costs (iii) and (iv). The idea is that adding a node or line to the grid should not affect, on average, the value of costs (iii) and (iv), respectively. To fulfill this purpose, we could compute costs (iii) and (iv) either as the weighted average of the costs J_{V_k} , $k = 1, \dots, K$ and $J_{I_l^{\pm}}$, $l = 1, \dots, L$ respectively or as their maximum value. The latter case results in a more conservative treatment of the grid constraints. The weights are computed individually for each objective by using Formula (4.23).

The second heuristic is the following: if objectives (ii), (iii) and (iv) are equal to zero, then the upper bound computed from Theorem 4.3 should be true for objective (i). This reflects the normal operating conditions in which there are no binding constraints; therefore, the accuracy of dispatch tracking should only be limited by the uncertainty of the system. Similarly, if objective (i) equals zero, then the upper bound should hold for objective (ii). These two heuristics lead us to one of the following grid cost functions. If we take the average of the grid constraints, we get the following cost:

$$\begin{aligned}
 J(\mathbf{x}|\mathbf{u}) &= w_{P_s} J_{P_s}(\mathbf{x}|\mathbf{u}) + w_{Q_s} J_{Q_s}(\mathbf{x}|\mathbf{u}) + \\
 &+ \frac{1}{K} \sum_{k=1}^K w_{V_k} J_{V_k}(\mathbf{x}|\mathbf{u}) + \\
 &+ \frac{1}{L} \sum_{l=1}^L w_{I_l^+} J_{I_l^+}(\mathbf{x}|\mathbf{u}) + w_{I_l^-} J_{I_l^-}(\mathbf{x}|\mathbf{u})
 \end{aligned} \tag{4.24}$$

and if we take the maximum, we get the following cost:

$$\begin{aligned}
 J(\mathbf{x}|\mathbf{u}) &= w_{P_s} J_{P_s}(\mathbf{x}|\mathbf{u}) + w_{Q_s} J_{Q_s}(\mathbf{x}|\mathbf{u}) + \\
 &+ \max_{k=1, \dots, K} \{w_{V_k} J_{V_k}(\mathbf{x}|\mathbf{u})\} + \\
 &+ \max_{l=1, \dots, L} \{w_{I_l^+} J_{I_l^+}(\mathbf{x}|\mathbf{u}) + w_{I_l^-} J_{I_l^-}(\mathbf{x}|\mathbf{u})\}
 \end{aligned} \tag{4.25}$$

where the weights w_{P_s} , w_{Q_s} , w_{V_k} , $w_{I_l^+}$, $w_{I_l^-}$ are computed by Formula (4.23) as if each objective was the single grid objective.

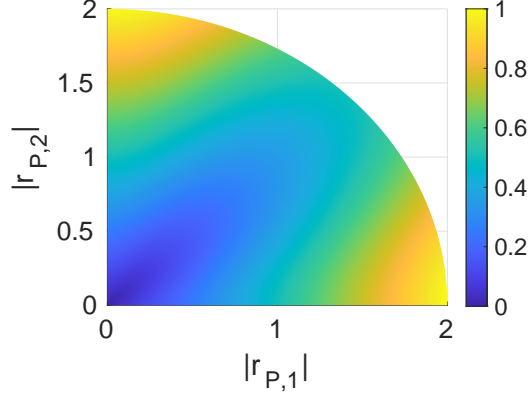


Figure 4.2: Evaluation metric for the batteries objective.

4.3.5 Discussion of the Limitations of the Method

In the formulation of the optimization problem we have provided in the thesis, Constraint 4.11 is a soft one, meaning that it is achieved via an appropriate cost function. We could have also achieved this condition by simply applying hard constraints for certain grid variables, such as the nodal voltages and branch currents. This could eliminate the need to choose weights for certain objectives. However, the theoretical results of Section 4.3.1 are derived under the assumption that there are no hard constraints in the problem, besides the BESSs' capabilities. This means that the statements of the theorems cannot be trusted if there are other hard constraints in the problem. The statements of the theorems could perhaps be generalized to consider both soft and hard constraints. This could be the topic of future research.

4.4 Numerical Validation of the Proposed Method

4.4.1 Evaluation Metrics

To compare our method with the "oracle" presented in Section 2.4.1, we define certain metrics that can be computed a posteriori for a given run time $[\tau, \tau + \Delta T]$. The metrics are chosen such that lower values indicate better performance. Specifically, a value greater than 1 indicates the worst performance.

For grid objectives, the metric is chosen so that the value is < 1 when $|y_m^{real}(t) - y_m^*(t)| < d_{max,m}^*(\tau)$. The value of $d_{max,m}^*(\tau)$ is assumed to be computed once for the whole time interval.

$$m_{y_m} = \frac{1}{\Delta T} \int_{t=\tau}^{\tau+\Delta T} \frac{|y_m^{real}(t) - y_m^*(t)|}{d_{max,m}^*(\tau)} dt \quad (4.26)$$

For BESSs, the metric needs to evaluate two things, specifically (i) the satisfaction of each individual battery objective and (ii) the fairness between the two objectives. Assuming only two BESSs, we can construct the metric given the vectors $\vec{r}_P = (|r_{P,1}|, |r_{P,2}|)$ and $\vec{r}_Q = (|r_{Q,1}|, |r_{Q,2}|)$

Chapter 4. Design of Cost Functions for the Fair Control of Battery Energy Storage Systems

where $r_{P,i}, r_{Q,i}$ are the preference ratios of BESS i defined in (4.1).

$$m_{P_B} = \frac{1}{\Delta T} \int_{t=\tau}^{\tau+\Delta T} |\vec{r}_P(t)| \frac{\cos(4\angle\vec{r}_P(t)) + 3}{8} dt \quad (4.27)$$

$$m_{Q_B} = \frac{1}{\Delta T} \int_{t=\tau}^{\tau+\Delta T} |\vec{r}_Q(t)| \frac{\cos(4\angle\vec{r}_Q(t)) + 3}{8} dt \quad (4.28)$$

The P metric's value as a function of the two preference ratios is depicted in Fig. 4.2, and a similar plot can be drawn for the reactive power. These metrics are designed to take values in $[0, 1]$, with increasing values indicating worse performance. In particular, the value 0 is taken only when $|\vec{r}_P(t)| = 0$ (similarly when $|\vec{r}_Q(t)| = 0$), which is achieved when both BESSs' preferences are perfectly satisfied. On the other hand, the value 1 is achieved when one BESS setpoint matches its respective preference, and the other differs from its own as much as possible; this indicates the most unfair scenario. Given that the maximum absolute value of a preference ratio is 2 (according to its definition), this condition is met when either $|r_{P,1}| = 0, |r_{P,1}| = 2$ or when $|r_{P,1}| = 2, |r_{P,1}| = 0$ (similarly for Q).

4.4.2 Evaluation of the Proposed Method in the Scenarios of Section 2.4

We now demonstrate the benefit of proposed method over the "oracle-based" approach, by applying it to the scenario of Section 2.4. We consider again the grid of Fig. 2.8 and use the same dispatch plan computed in Section 2.4.1. The RT control solves again the Optimization Problem (2.12) every 10 seconds. However, the cost functions used are different than those used in Section 2.4.

Concerning the battery objective, we assume again the same target SoC that the BESSs have received from the dispatcher, and we adapt the Cost Function (2.13) to satisfy the general form of (4.3). The preference of BESS i is computed as follows:

$$P_i^*(\Delta SoC, \epsilon_i) = \begin{cases} -\frac{S_i}{\sqrt{2}} & \Delta SoC_i \leq -\epsilon_i \\ \frac{\Delta SoC_i}{\epsilon_i} \frac{S_i}{\sqrt{2}} & -\epsilon_i < \Delta SoC_i < \epsilon_i \\ \frac{S_i}{\sqrt{2}} & \Delta SoC_i \geq \epsilon_i \end{cases} \quad (4.29)$$

With this formula, if the SoC of a BESS is higher than the respective target value, then the BESS would prefer to discharge (P^* is positive); otherwise, it would charge (P^* is negative). The purpose of ϵ_i is to prevent the preference from oscillating between the two bounds when $\Delta SoC \approx 0$. An appropriate condition for this purpose is $\epsilon_i \gg \frac{S_i T}{E_{max,i}}$, where $E_{max,i}$ is the energy capacity of the BESS and $T = 10$ s is the time interval between two computation cycles. For this experiment, we consider $\epsilon_1 = \epsilon_2 = \frac{S_i \cdot 300 \text{ s}}{E_{max,i}} = 1/12$, where 300 s is the period of the dispatch plan. The coefficients a_P, a_Q in the battery cost are $a_P = a_Q = 1$.

For the grid objective, we use the general Form (2.8). The weights of each individual objective are computed according to Theorem 4.3. The theorem allows for considering the uncertainty

4.4 Numerical Validation of the Proposed Method

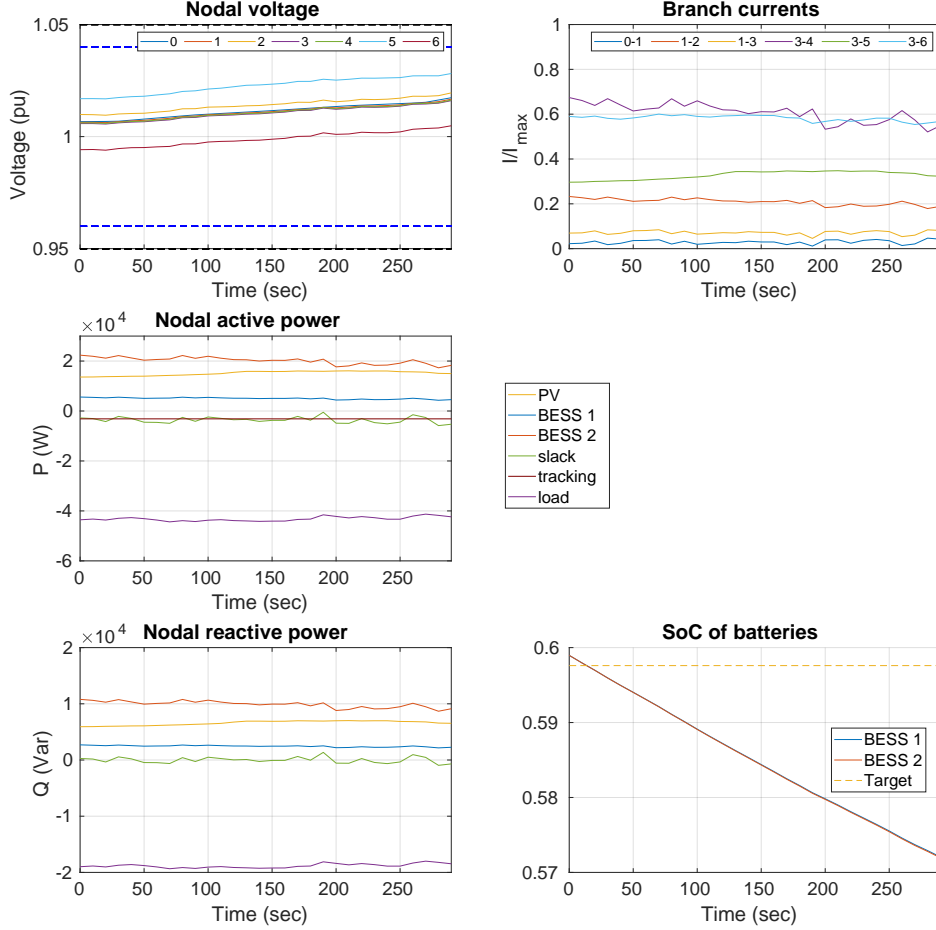


Figure 4.3: Simulation results for the scenario of Section 2.4.2 with our proposed weight-computation method.

in the grid as well, which can be computed with Formula (4.17). To estimate the uncertainties of the stochastic power injections, we could use the method presented in Chapter 3. However, for simplicity, we can use the results obtained in this chapter, which indicate that the method can achieve an uncertainty bound of around 5% with a confidence level of 99% and for time resolutions in the order of 10 s. Therefore, we will use a fixed uncertainty of 5% for the PV generation and the load consumption in the simulations. In Chapter 5, where we do an experimental validation of the proposed control framework, we will use the full method of Chapter 3.

We must now choose the soft upper bounds $d_{max,m}^*$ for the various grid objectives as defined in Section 4.3.2. For the voltage objective, the hard upper bound is dictated by regulations, which we assume to be $\beta_{hard} = 0.05$ pu. For the soft upper bound, we want the controller to start

Chapter 4. Design of Cost Functions for the Fair Control of Battery Energy Storage Systems

reacting to voltage tolerances at 90% of the hard upper bound, so we choose $\beta_{soft} = 0.04$ pu. Similarly, for the current objective, we want the controller to react when a branch current approaches 90% of the respective ampacity, and we can choose $\gamma_{soft} = 0.9$. Because these objectives reflect hard grid constraints, we also consider the uncertainty $|\Delta y_m|_{max}$ in the computation of their weights to satisfy the constraints in the worst case.

The two slack objectives, on the other hand, do not reflect hard grid constraints. Therefore, we do not consider the uncertainty $|\Delta y_m|_{max}$ in the weight computation of Theorem 4.4. However, we can incorporate the uncertainty in the soft upper bounds $|P_s - P^{DP}|_{max}$ and $|Q_s|_{max}$. These upper bounds should not be larger than the slack active and reactive power uncertainty, respectively. Otherwise, they cannot be guaranteed. Therefore, we can choose $|P_s - P^{DP}|_{max} = |\Delta P_s|_{max}$ and $|Q_s|_{max} = |\Delta Q_s|_{max}$.

Scenario of Section 2.4.2 - Normal Operating Conditions

For this scenario, the PV generation and the load consumption are shown in Fig. 2.10. We run the simulation with our weight computation method and compare the results shown in Fig. 4.3 with the oracle-based approach of Fig. 2.12. We first observe that both methods can track the dispatch plan and effectively limit the reactive-power exchange with the main grid. The currents and voltages are also approximately the same for the two methods throughout the simulation. With the oracle-based approach, however, there is a reactive power exchange between the two BESSs at the beginning of the simulation, which causes a larger current through branch 3-4. This is not observed with our proposed method, as the weights of the grid objectives are adaptively computed according to the state of the grid. Moreover, our method achieves better SoC regulation as the two SoCs follow the same trajectory. This is the expected behavior because there are no binding grid constraints.

Table 4.1

VALUE OF METRICS FOR THE SCENARIO OF SECTION 2.4.2 WITH THE ORACLE-BASED APPROACH AND THE PROPOSED METHOD.

| Method | m_{P_s} | m_{Q_s} | $\overline{m_{V_k}}$ | $\overline{m_{I_l}}$ | m_{P_B} | m_{Q_B} | Average |
|-----------------|-----------|-----------|----------------------|----------------------|-----------|-----------|---------|
| Same Weights | 9.473 | 7.352 | 0.203 | 0.157 | 0.296 | 0.012 | 2.916 |
| Oracle-based | 0.217 | 0.375 | 0.302 | 0.276 | 0.182 | 0.286 | 0.273 |
| Proposed method | 0.349 | 0.322 | 0.300 | 0.254 | 0.172 | 0.058 | 0.243 |

The evaluation metrics as defined in Section 4.4.1 are shown in Table 4.1 for three cases, namely:

1. For the simulation of Fig. 2.11 which uses the cost functions of Section 2.3 and the same weight for all objectives.
2. For the simulations of Fig. 2.12, which uses the same cost functions, but the weights are tuned a posteriori.

4.4 Numerical Validation of the Proposed Method

3. For the simulations of Fig. 4.3 which uses the cost functions defined in this chapter and our proposed weight-computation method.

For the voltage and current objectives, in particular, we compute the average value of the metric across all nodes and branches, respectively. First, the oracle-based approach and our proposed method achieve much better values for the two slack metrics. The voltage and current control performance is slightly worse, but the two metrics are still much smaller than 1. This verifies that in the first simulation, the controller sacrificed dispatch tracking and reactive power control to limit the voltage deviations and the currents as much as possible, which means that the weights were not configured properly.

We also observe that our method achieves slightly better average metrics values than the manually tuned weights. In particular, our method achieves better values for all metrics except the dispatch-tracking one, which is nonetheless much smaller than 1. Of course, achieving a smaller value for all metrics with one method is impossible, as all objectives compete against each other. However, our method performs similarly to the oracle-based approach, with the benefit of being more practical, as the control parameters do not need to be tuned a posteriori. The value of our method will be more clearly highlighted in the following two examples.

Scenario of Section 2.4.3 - Binding Constraint

Table 4.2
VALUE OF METRICS FOR THE SCENARIO OF SECTION 2.4.3 (HIGHER LOAD CONSUMPTION).

| Method | m_{P_s} | m_{Q_s} | $\overline{m_{V_k}}$ | $\overline{m_{I_l}}$ | m_{P_B} | m_{Q_B} | Average |
|--|-----------|-----------|----------------------|----------------------|-----------|-----------|---------|
| Oracle-based $w_1 = w_2$ | 0.197 | 0.273 | 0.317 | 0.336 | 0.332 | 0.336 | 0.299 |
| Oracle-based $w_1 = 6w_2$ | 0.175 | 0.170 | 0.308 | 0.335 | 0.258 | 0.337 | 0.264 |
| Proposed method with cost-function (4.24) | 0.398 | 0.332 | 0.309 | 0.316 | 0.264 | 0.120 | 0.290 |
| Proposed method with cost-function (4.25) | 0.407 | 0.330 | 0.310 | 0.316 | 0.277 | 0.109 | 0.291 |

We now consider the scenario of Section 2.4.3, in which the consumption of the load is 20% larger than before. As there is a potential binding constraint for the branch currents, we consider the two cost functions for the branch current objective defined in (4.24) and (4.25). The simulation results with our method and the two cost functions are shown in Figs. 4.4 and 4.5, which are to be compared with the results of Figs. 2.13 and 2.14. In Section 2.4.3, we tested two sets of weights, one where the weights of the BESSs are equal ($w_1 = w_2$) and one where $w_1 = 6w_2$. The second set of weights achieved what seems to be a more fair SoC regulation in Fig. 2.14 because the two SoCs are closer to each other. However, this does not comply with our definition of fairness in Section 4.2.1. Indeed, according to our design goal, in a fair situation, the battery objective should give way to the grid objective whenever there is a binding constraint. As we can see in both Figs. 4.4 and 4.5, BESS 2 discharges at a slower

Chapter 4. Design of Cost Functions for the Fair Control of Battery Energy Storage Systems

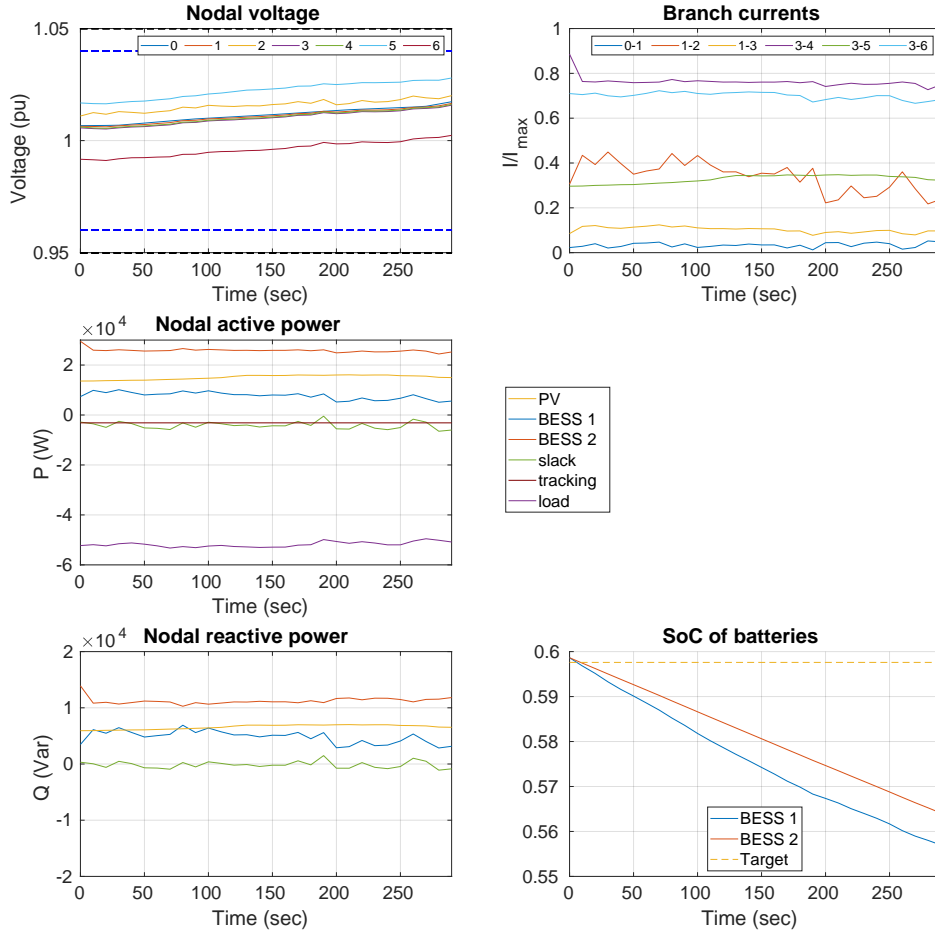


Figure 4.4: Simulation results for the scenario of Section 2.4.3 (higher load consumption) with our proposed weight-computation method and total grid-cost function given by (4.24)

rate with our method as the current in branch 3-4 approaches the soft current constraint (90% of the ampacity). If we compare the SoC graph with graphs (c) and (d) of Fig. 2.14, we observe that the SoC deviation seems to be in-between the two ones achieved with the two candidate sets of the weights selected manually ($w_1 = w_2$ and $w_1 = 6w_2$).

The comparison becomes clear if we examine the values of the evaluation metrics shown in Table 4.2. Indeed, the performance of our method regarding the BESS active-power objective and the average performance is between the two achieved with manually chosen weights. Of course, the choice $w_1 = 6w_2$ is a better choice for this scenario on average, but as we have seen, this choice does not work well for all possible realizations of the load consumption. On the other hand, our method achieves an acceptable performance irrespective of the studied scenario. Finally, choosing between the average branch-current cost of Equation (4.24) and

4.4 Numerical Validation of the Proposed Method

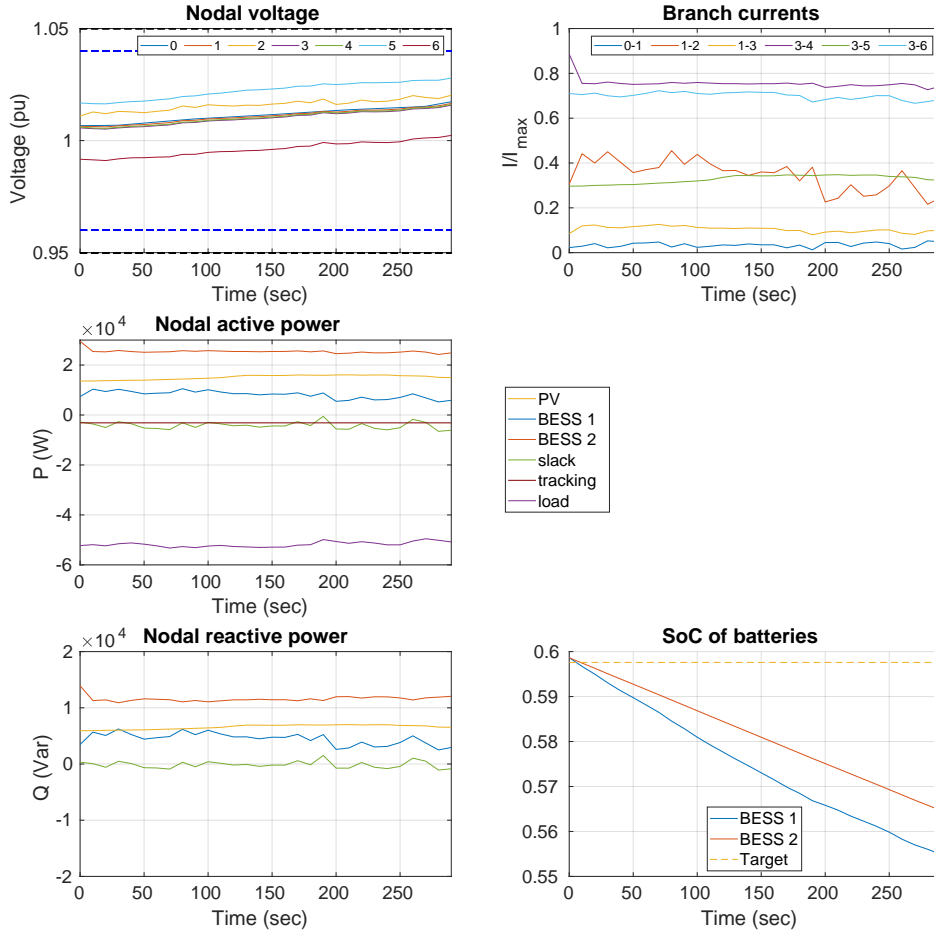


Figure 4.5: Simulation results for the scenario of Section 2.4.3 (higher load consumption) with our proposed weight-computation method and total grid-cost-function given by (4.25).

the maximum one of Equation (4.25) yields similar results.

Scenario of Section 2.4.4 - Change in the Topology

Finally, we consider the scenario of Section 2.4.4, in which BESS 1 is replaced with a bigger one at 60 kVA/60 kWh. We saw before that the weights chosen manually for the scenario of Section 2.4.2 were not appropriate for this new topology, as the fairness between the two SoCs was not achieved despite having no binding constraints (see Fig. 2.15). We run the same simulation using our proposed cost functions and weight-computation method. The results are shown in Fig. 4.6, from which it is clear that the SoC regulation is fair. This can also be verified by looking at the metrics in Table 4.3; our method achieves smaller values for almost all the metrics in this new topology.

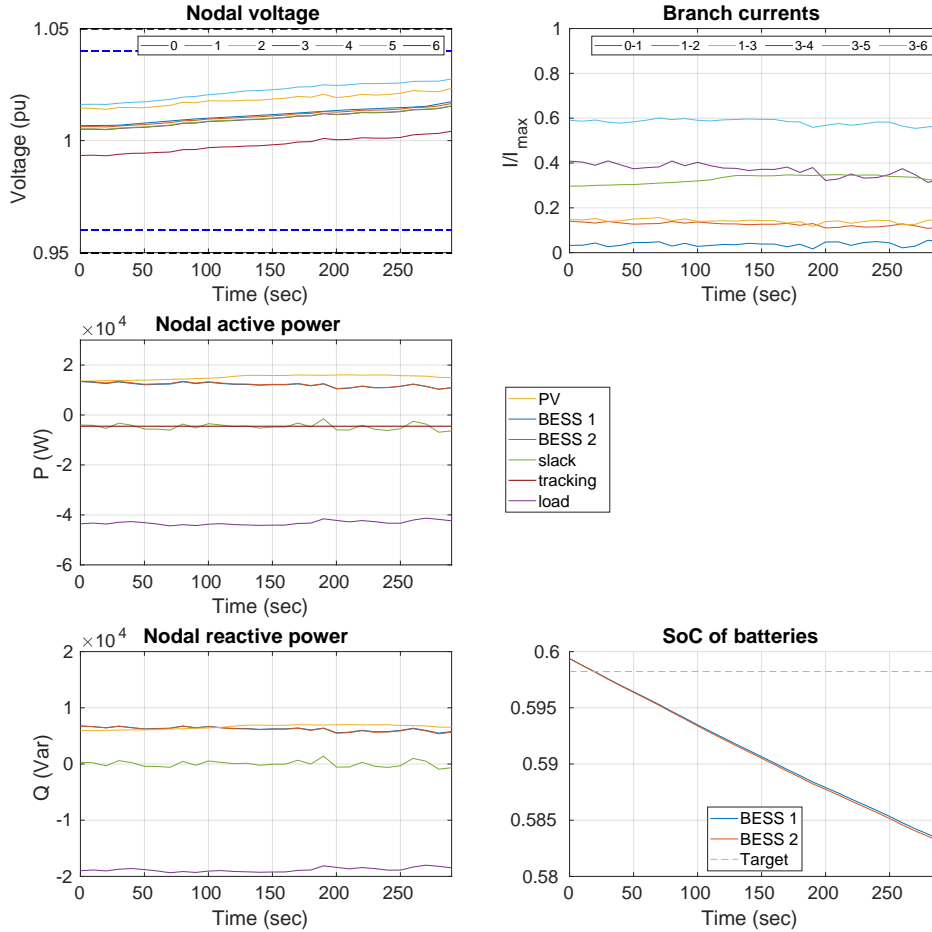


Figure 4.6: Simulation results for the scenario of Section 2.4.4 (bigger BESS 1 at 60 kVA/60 kWh) with our proposed weight-computation method.

4.4.3 Applicability of the Proposed Method in a Different Control Framework

To further justify the merit of the proposed method, we apply it to another case study. Specifically, the work of Borghetti et al. [2]. This case is similar to the one studied in our work, as (i) it considers a multi-layer control approach and (ii) it considers both individual resources and global grid objectives. Moreover, Borghetti et al. do not give insight into how they chose the objectives' weights, implying that they were chosen by some "oracle", as we have explained before.

The control consists of two layers, namely (i) day-ahead and (ii) intra-day. The first layer computes a target power trajectory for each energy resource in the grid to be followed by the second layer. In addition to tracking the power trajectories, the second layer minimizes voltage deviations from the nominal value. Here, we target a simplification of the problem defined in

4.4 Numerical Validation of the Proposed Method

Table 4.3
VALUE OF METRICS FOR THE SCENARIO OF SECTION 2.4.4 (BIGGER BESS 1 AT 60KVA/60KWH).

| Method | m_{P_s} | m_{Q_s} | $\overline{m_{V_k}}$ | $\overline{m_{I_l}}$ | m_{P_B} | m_{Q_B} | Average |
|-----------------|-----------|-----------|----------------------|----------------------|-----------|-----------|---------|
| Oracle-based | 0.276 | 0.542 | 0.330 | 0.216 | 0.149 | 0.088 | 0.267 |
| Proposed method | 0.331 | 0.323 | 0.315 | 0.221 | 0.102 | 0.037 | 0.222 |

[2], where the objective of the higher layer is the simplified distflow used in Section 2.4⁴. We consider again the grid of Fig. 2.8, where the target power trajectory of each BESS was computed by solving the dispatch plan defined in (2.32). This is done by computing the expected power trajectory from the respective SoC trajectory for each BESS. The target objective of the RT control is

$$\min_{P_j} \sum_{j=1}^{N_B} \alpha |P_j - \bar{P}_j| + \sum_{k=1}^K \gamma |V_k - 1| \quad (4.30)$$

where P_j and \bar{P}_j are the computed and target power of BESS j , respectively, and V_k is the voltage of bus k .

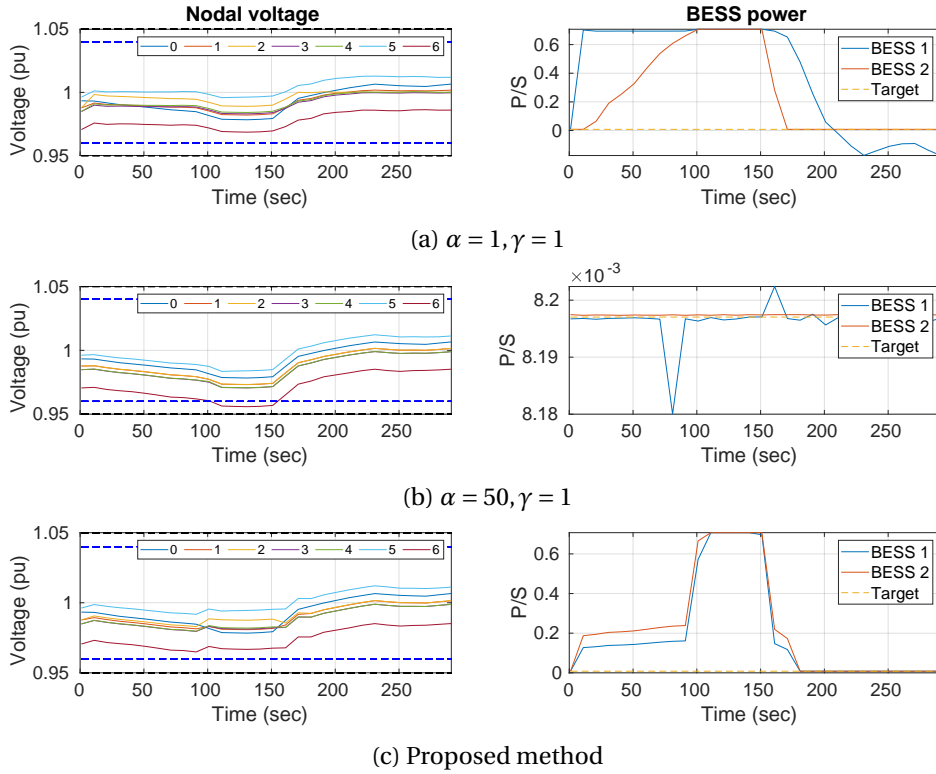


Figure 4.7: Simulation results for the problem defined in [2] for three different weight configurations.

We consider the same scenario for the load and PV as in Fig. 2.10. Because the control is

⁴Borghetti et al. consider more types of dispatchable DERs, each with a given energy cost assigned to it

Chapter 4. Design of Cost Functions for the Fair Control of Battery Energy Storage Systems

supposed to achieve voltage regulation, it would be interesting to study a case where the voltages in the grid are low. For this reason, we consider the slack-voltage profile as shown in Fig. 4.7 (see bus 0 on the graphs on the left).

Borghetti et al. consider two sets of values for the weights α and γ , namely (i) $\alpha = 1, \gamma = 1$ and (ii) $\alpha = 50, \gamma = 1$. Fig. 4.7 shows the evolution of the BESS power trajectories and their respective targets normalized by the rated power of each BESS for these two cases. When the two weights are equal, the controller forces either BESS 1 or both BESSs to produce at their maximum power ($\frac{\sqrt{2}}{2}S$) to compensate for the voltage drop. Whereas, when $\alpha = 50$, the two trajectories match their target value (notice the scale of the P/S axis), meaning that the controller fails at regulating the voltage.

To compare with our method, we must first convert the absolute values in Equation (4.30) to square functions to satisfy our guidelines that the grid cost-functions be convex and differentiable. The results with our method are also shown in Fig. 4.7. Concerning voltage regulation, our method achieves a more fair control than the manual-weight-tuning approach, as the control reacts to voltage deviations and keeps the ratios P/S very close to each other. Also, the powers of the two BESSs deviate from each other more as the voltages get closer to the soft upper bound, which is the expected behavior of our method. We have thus seen how others can apply our method in their RT control with minor modifications.

4.5 Discussion and Limitations of the Proposed Method

In this chapter, we have defined guidelines for designing objectives for the RT control of BESSs and proposed a method for computing their weights. Our method requires only certain parameters as input that can be chosen intuitively and achieves a comparable performance to oracle-based approaches that are usually applied by the existing literature and are not feasible in practice. Because the method is grid-agnostic, we have also shown it can easily be applied to different problems; hence, others can employ it in their work.

Even though we did not thoroughly compare our weight-computation method to other methods in the literature, it is worth discussing briefly some other potential methods that can be used for this purpose. [98] presents a method called “the Analytical Hierarchy Process (AHP)” to compute the weights of actions in decision-making. The method requires the input of judgments to compare the importance of one action over another towards a given objective. The judgments take values from 1 to 9, with the lowest signifying equal importance of actions towards the objective and the highest indicating an extreme importance of one action over another. However, there is no obvious way to choose these judgments. In the case studied in this thesis, it is unclear how the various grid objectives should be compared, because the objectives are different in nature. For example, using the AHP, we would need to judge, on a scale from 1 to 9, the importance of voltage control over SoC balancing. On the other hand, our method is much easier to configure as the weights of the grid objectives are chosen independently. However, it is worth studying more thoroughly how the AHP could be used for RT

4.5 Discussion and Limitations of the Proposed Method

grid control in future research.

Apart from analytical methods, we could also use machine learning (ML) based approaches to compute the weights, such as reinforcement learning (RL). Using RL, we could learn the optimal weights of the controller that maximize a given long-term reward for every possible state of the grid. However, in this case, we would need to choose an appropriate reward function for the RL algorithm, which should not include weights of its own. Moreover, a benefit of our method over ML is that the former gives us an intuition of how the controller would perform a priori, while the results of ML are often hard to interpret.

It is also worth discussing the limitations of our method for designing cost functions. Currently, the method considers that all BESSs have the same objective: to regulate their SoC for dispatchability. The proposed cost functions could still be used with minor adaptations in other cases where all BESSs have the same common objective, such as if they are used for primary frequency control. However, it would also be interesting to study cases where BESSs have different objectives, for example, one BESSs acting as the slack bus. In this case, the design goal of the system will be different, so the form of the battery cost function might need some adaptations. However, the methodology we used in this chapter to derive the cost functions could be followed to design cost functions for different problems in the future.

Another limitation of the proposed design is that the cost functions considered in the simulations were designed with a short-term goal. According to state-of-the-art, fairness, in the long run, is equivalent to having the same SoC regulation for all BESSs, a condition that our method cannot guarantee, especially when binding constraints are present. As explained in Chapter 2, long-term objectives can be accounted for by an intra-day layer, which could give updated instructions to the RT layer, such as a new target SoC trajectory, adapted according to the state of the grid and updated forecasts of the stochastic power injections. In Section 5.3, we propose an intra-day layer and experimentally validate our control framework over a long period.

5 Experimental Validation of the Proposed Control Framework for Battery Energy Storage Systems

5.1 Introduction

In Chapter 2, we introduced a generic framework for the RT control of ADNs. The framework consists of (i) the day-ahead scheduling layer and (ii) the control layer. We discussed different options for the control layer and concluded that an intra-day, together with an RT control, is the optimal structure as it combines the benefit of the two. In Chapters 3 and 4, we discussed two aspects of the design of the RT control layer, namely the computation of ultra-short-term PIs of heterogeneous resources and the design of the cost functions in the optimization problem to be solved by the RT controller. We also discussed in Section 4.4 how the methods developed in the thesis for the PI computation and the design of cost functions can be used in practice to control an ADN. However, the validation was done only with simulations of a short duration. To better evaluate the value of the methods proposed in the thesis, it would be interesting to test them in real experimental settings and for a longer period.

In this respect, this chapter showcases the evaluation of two control frameworks based on the generic framework proposed in Chapter 2 in real experimental settings. Our goal is to highlight the applicability of the methods of Chapters 3 and 4 by showing how they can be adapted to two RT control frameworks to achieve dispatching and fair control of BESSs. In Section 5.2, we use the COMMELEC framework, already proposed in [7, 8], together with our PI-computation algorithm and our proposed cost functions to track a pre-computed dispatch plan for a real MV distribution grid located in Aigle, Switzerland, using a single BESS. In Section 5.3, we use a novel two-layer control framework inspired by similar control frameworks in the literature (e.g., [19]) to achieve a fair control of two BESSs connected in an MV/LV distribution grid at EPFL.

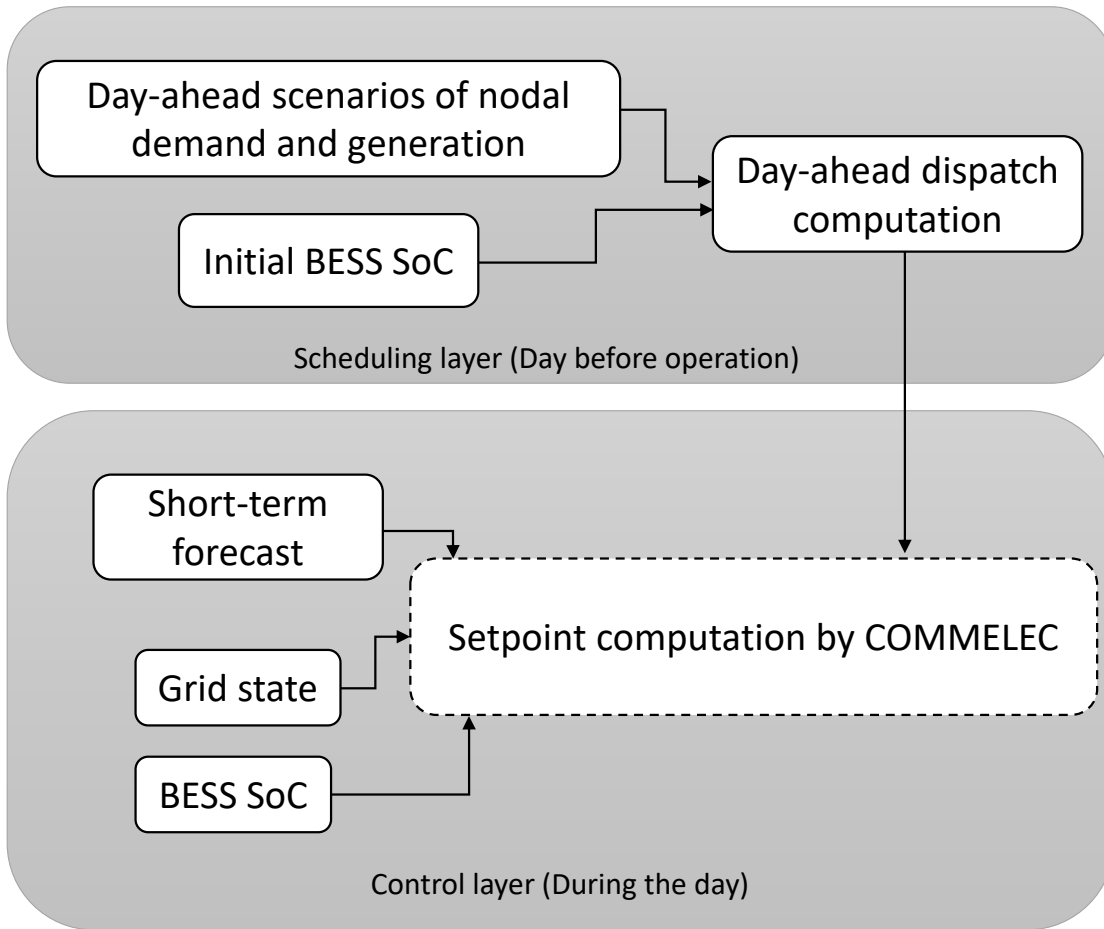


Figure 5.1: Schematic diagram of the control framework using COMMELEC.

5.2 Dispatch Tracking in a Utility-Scale Grid Using the COMMELEC Framework

We assume we want to control a generic ADN with heterogeneous DERs as in Fig. 2.1. For this purpose, we consider the generic two-layer control approach proposed in Chapter 2 and shown in Fig. 2.5. The grid is dispatched by controllable DERs using an RT control to follow a predetermined dispatch plan. The RT control aims to track the dispatch plan and maintain the nodal voltages and branch currents within strict limits.

In this section, we consider using the COMMELEC framework [7] as the RT control. COMMELEC is a framework designed for the RT control of grids with heterogeneous resources that aims to address the issues of the conventional droop-based methods for primary control. It has already been validated in an experimental environment in a test microgrid [99] and was shown to successfully achieve RT dispatchability for the targeted grid and provide primary frequency support or autonomous microgrid operation. However, the past experiments were performed in a test microgrid, whereas we now consider a real MV grid. Due to the large

5.2 Dispatch Tracking in a Utility-Scale Grid Using the COMMELEC Framework

number of prosumers in the considered grid, we must estimate their uncertainty accurately to avoid steering the grid in an undesirable state. In [99], the only uncertain prosumption was that of a 20 kW PV and the method described in [100] was used to forecast its power. However, the grid in question has multiple types of prosumers, combining loads, PVs and hydropower plants (see Section 5.2.3), so a more sophisticated forecasting method is needed. Moreover, the objective used by COMMELEC in [99] defines some weights, the choice of which is not adequately discussed. As we have discussed extensively, this weight choice might not be suitable for our experiments. These limitations, together with COMMELEC's ability to deliver power setpoints as fast as 100 ms, make it an ideal choice to test the methods of Chapters 3 and 4.

By replacing the setpoint computation with COMMELEC, the control approach becomes the one shown in Fig. 5.1. A brief summary of the computation of the dispatch plan is given in Section 5.2.1, whereas the COMMELEC framework is outlined in Section 5.2.2. The experimental results of this section are available in the technical report [101].

5.2.1 Dispatch Plan Computation

At the beginning of the day, the scheduling layer computes a dispatch plan at a 5-minute resolution to be followed by the ADN at the PCC. The dispatcher receives as inputs day-ahead scenarios of the stochastic nodal demand and electricity generation for the following day at a 5-minute resolution and the initial SoC of the BESSs. The forecasting of the stochastic resources is performed with methods presented in [3]. The dispatch plan is computed using the method in [91]. The objective of the dispatcher is to minimize the average dispatch error among scenarios while satisfying the grid's and BESS's constraints for all scenarios and ensuring that the power factor at the PCC remains within the given bounds. This way, the dispatcher computes the best power profile that can be tracked at the PCC, given the grid, the BESSs, and the power factor constraints. Because the thesis focuses mainly on the RT control, the dispatch formulation is omitted, but the interested reader is forwarded to [91] for more details.

5.2.2 The COMMELEC Framework

We give an overview of the COMMELEC framework, which is enough to describe the experiments performed. For more details, the reader is forwarded to the relevant literature [7, 8]. COMMELEC uses a hierarchy of agents to compute explicit active and reactive power setpoints for the energy resources connected to the grid. Each resource is equipped with a resource agent (RA) whose task is to translate the internal state of the resource into a device-independent format (advertisement). The advertisements are collected by the grid agent (GA), which computes the optimal power setpoints that optimize a global objective. The global objective is the weighted sum of various objectives, similar to the ones of Section 2.3, including tracking a predetermined dispatch plan at the slack bus, minimizing the grid's nodal voltage deviations

from the nominal value, limiting the branch currents below the respective ampacities, and achieving target internal states for the resources.

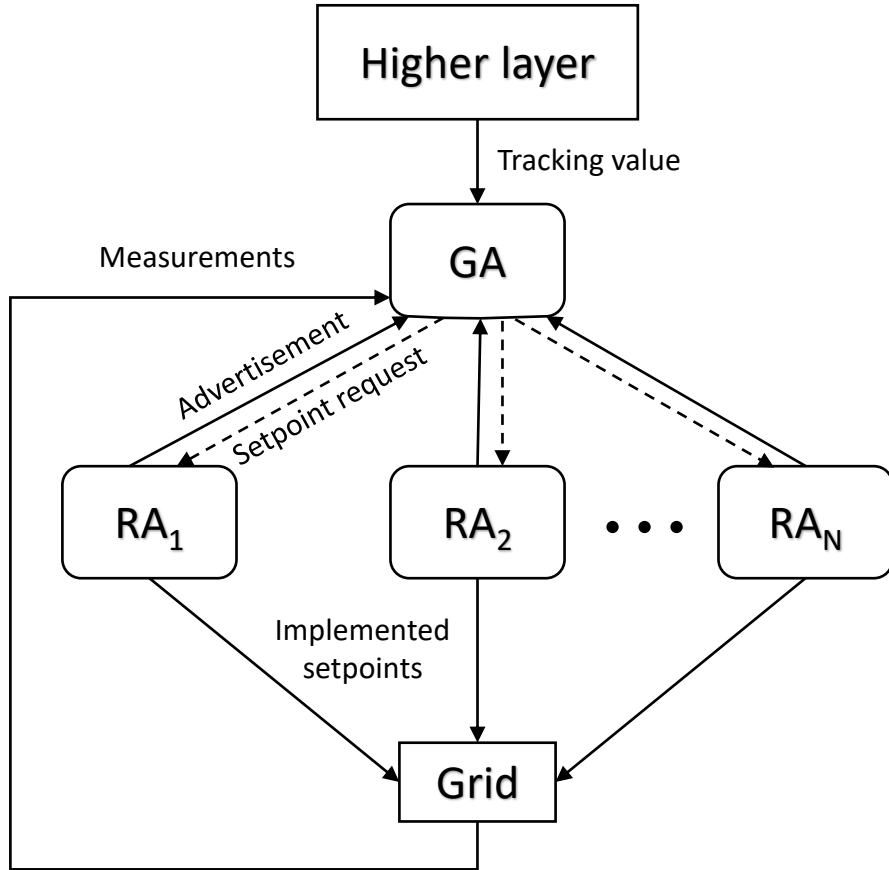


Figure 5.2: Structure of the COMMELEC decision cycle.

Fig. 5.2 shows the decision process of the GA. At each COMMELEC cycle, the GA receives 1) the advertisements from all RAs, 2) an estimation of the state of the grid (nodal voltages and line currents), and optionally, 3) a setpoint to be followed by a higher layer of control. In our experiments, the day-ahead dispatch plan calculates the target setpoint. Then, the GA computes a set of active and reactive power setpoints for all resources that optimize a global objective. The duration of each cycle can be as small as 100 ms, which is larger than the update frequency of the grid state estimation (typically 20 ms if the grid sensing is realized by PMUs).

Each advertisement message consists of three elements:

1. PQ profile: a set of all the (P, Q) points the resource can implement.
2. Cost function: the RA assigns a cost value to each point in its PQ profile to denote the preference of the resource to implement a given point.
3. Belief function: it is a set-valued function that quantifies the uncertainty of the resource.

5.2 Dispatch Tracking in a Utility-Scale Grid Using the COMMELEC Framework

For each point (P, Q) of the PQ profile, the RA advertises a set of all the points (P', Q') the resource might implement if the point (P, Q) is requested by the GA.

In Section 5.2.3, we will give examples of advertisements for the energy resources we use in the experiments.

The objective to be minimized by the GA is similar to the one defined in Equation (2.7) and is the following:

$$C_{GA}(\mathbf{x}) = \sum_{i=1}^{N_r} C_i^r(P_i^r, Q_i^r) + J(\mathbf{x}) \quad (5.1)$$

where N_r is the number of RAs, $\mathbf{x}_i^r = (P_i^r, Q_i^r)$ is the power setpoint of RA i and \mathbf{x} is the set of all nodal power injections in the grid. $C_i^r(P_i^r, Q_i^r)$ is the cost function advertised by RA i and $J(\mathbf{x})$ is the grid objective. In each COMMELEC computation cycle, the GA updates the setpoint for resource i by doing one step of gradient descent (GD) as follows:

$$\hat{\mathbf{x}}_i^r = Pr_{PQ_i} \{ \mathbf{x}_{i,0}^r - s_i \nabla_{\mathbf{x}} C_{GA}(\mathbf{x}) |_{\mathbf{x}=\mathbf{x}_0} \} \quad (5.2)$$

where $\mathbf{x}_{i,0}^r$ is the current setpoint of resource i and \mathbf{x}_0 is the set of the nodal power injections as measured in the grid. $\nabla_{\mathbf{x}}$ is the gradient with respect to the power injections and s_i is the GD step for RA i . After the GD step is performed, the computed setpoint is projected into the PQ profile of RA i , indicated by the operation $Pr_{PQ_i} \{ \cdot \}$ to ensure that the resource can implement the resulting setpoint. More details about the projection can be found in [4].

As a final step of the algorithm, the belief functions of the RAs are also employed to ensure that the computed setpoints will not violate any of the grid's constraints accounting for the uncertainty of the system. This is performed by shrinking the step sizes s_i until the computed setpoints do not violate any constraint for every possible setpoint within the belief functions of all RAs. It should be noted that this optimization algorithm is not guaranteed to result in the global optimum of the Objective Function (5.1) in one cycle. Rather, it is a fast algorithm that can provide approximate solutions to the problem in a few ms, thus being suitable for the real-time control COMMELEC is intended for. Moreover, as long as the state of the grid changes slower than the frequency of the computation cycle, the GA will reach the global optimum of the objective after consecutive GD steps.

5.2.3 Experimental Setup

Grid Topology

The experiments were performed in an MV distribution grid operated by the local DSO Romande-Energie¹ in Aigle, Vaud, Switzerland, which is shown in Fig. 5.3. The grid's nominal voltage is 21 kV. The peak power prosumption at the feeder is 4.2 MWp. Multiple nodes are

¹<https://www.romande-energie.ch/>

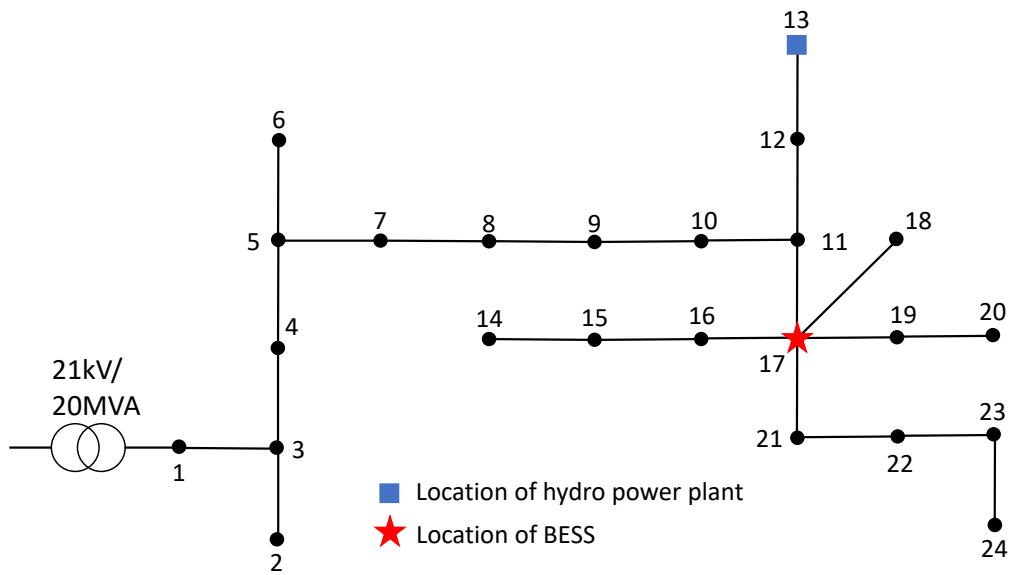


Figure 5.3: Topology of the MV distribution network in Aigle.

equipped with PV installations for a total maximum PV generation of 3.2 MWp. Moreover, node 13 incorporates hydropower plants with a rated power of 3.4 MVA. Node 17 is equipped with a fully controllable (4-quadrants) 1.5 MW/2.5 MWh BESS. The technical specifications of the BESS are shown in Table 5.1.

Metering Infrastructure

COMMELEC needs RT estimation of the grid's state to compute the setpoints for the RAs. For this purpose, the grid is equipped with a state-of-the-art grid-monitoring solution called SynchroGuard². It can estimate the state of the whole grid, including all voltages, currents, and powers, at 50 frames per second, by placing PMUs on only a subset of the grid's nodes (17 out of 24 nodes in our setup).

The PMU measurements are streamed to our server via a public 4G network, as shown in Fig. 5.4. Our server can be accessed via the Romande Energie VPN. We have installed 6 VMs which are connected via two virtual switches (vSwitch). The PMU measurements are forwarded to VM2, which runs the grid's state estimator via VM1, which acts as a router and firewall. The estimations of the grid's states are then sent to a Database (VM3) for logging. VM4 runs the code of the dispatcher, whereas VM5 runs all the COMMELEC-related code, i.e. the GA and all RAs (see section "COMMELEC implementation"). Finally, VM6 runs the BESS actuator. Our server is connected to the battery management system (BMS) and the BESS converter, which run on separate machines via ethernet cables.

²<https://zaphiro.ch/technology/>

5.2 Dispatch Tracking in a Utility-Scale Grid Using the COMMELEC Framework

Table 5.1

TECHNICAL SPECIFICATIONS OF THE BESS USED FOR THE EXPERIMENTS OF SECTION 5.2 (ADAPTED FROM [3]).

| Parameter | Value |
|--------------------------------------|---|
| Nominal capacity | 1.5 MVA/2.5 MWh |
| Voltage at the grid connection point | 21 kV |
| DC bus voltage range | 770-1000 V |
| PCS efficiency | 93% for all operating conditions |
| Total harmonic distortion | < 3% |
| Number of racks | 30 in parallel |
| Number of modules per rack | 11 in series |
| Cells configuration per module | 1p22s |
| Total number of cells | 7260 |
| Cell nominal voltage | 3.68 V (limits 2.7 V - 4.15 V) |
| Cell nominal capacity | 94 Ah (343 Wh) |
| Cell technology | Lithium Nickel Manganese Cobalt Oxide (NMC) |
| Battery life cycle | 4000 equivalent cycles at 1C rate and 100% Depth-of-Discharge with 80% of initial storage capacity available at the end of life |

COMMELEC Implementation

We implement three software agents to dispatch the grid of Fig. 5.3. The GA and two types of RAs, namely the battery agent (BA) and the shadow agent (SA). The BA is used to control the BESS, whereas the SAs are used to estimate the uncertainties of uncontrollable prosumers. Unlike the BA, the SA is not responsible for implementing power setpoints; it only acts as a middleman between a prosumer and the GA (hence the name "shadow agent"). Fig. 5.5 shows the specific implementation of Fig. 5.2 that was used in our experiment.

We use a modified implementation of the GA used for the experiments in [99], coded in C++, which uses the grid-cost functions and the weight-computation method of Chapter 4. In particular, the grid cost $J(\mathbf{x})$ in (5.1) has been replaced by the one defined in Equation (4.24), and the weights of the objectives are computed by Formula (4.23). The parameters of the controller, as defined in Section 4.3.2, are the following: hard voltage constraint $\beta_{hard} = 0.05$ pu, soft voltage constraint $\beta_{soft} = 0.04$ pu, soft current constraint $\gamma_{soft} = 0.9$, soft slack-active-power-tracking tolerance $|P_s - P^{DP}|_{max} = 100$ kW and soft slack-reactive-power tolerance $|Q_s|_{max} = 100$ kVAr. The values for the slack tolerances were chosen as a 95% confidence interval of the slack's power-differences histogram³. Regarding the hard voltage and current constraints, we do not consider the uncertainty $|\Delta y_m|_{max}$ when computing the weights w_{y_m} (see Section 4.3.1 and Formula (4.23)), because COMMELEC incorporates the uncertainty of the grid in the belief

³In the experiment of Section 5.3, we use the method of Chapter 3 to get a more accurate estimate of the slack's uncertainty.

Chapter 5. Experimental Validation of the Proposed Control Framework for Battery Energy Storage Systems

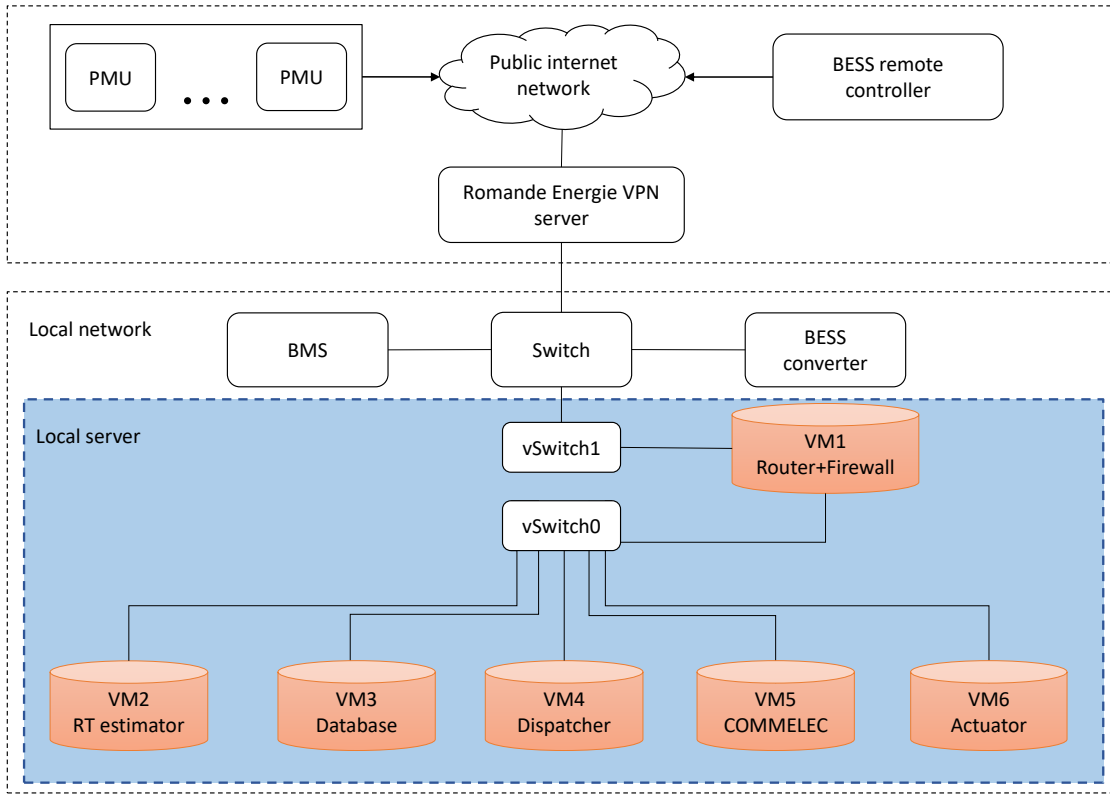


Figure 5.4: IT infrastructure in Aigle.

function, as explained below.

The BA, coded in LabVIEW and adapted from [85], aims to advertise the state of the BESS in a COMMELEC-compatible format and implement the setpoints computed by the GA. The cost function advertised by the BA is in the form defined in Equation (4.3). The goal of the BESS is to achieve an arbitrary target SoC of 50%, so its preference (see Section 4.2.1) is defined as in Equation (4.29) with $SoC^{target} = 0.5$.

The PQ profile reflects the capability curve of the BESS, which depends on the BESS's DC voltage and the AC voltage at the grid [102]. An instance of the PQ profile and the belief function that the BA could advertise is shown in Fig. 5.6a. The BESS is assumed to implement $P=500$ kW and $Q=200$ kVar. The BESS's DC voltage is $V_{DC} = 750$ V, and the nodal AC voltage is $V_g = 390$ V. The PQ profile is shown as a blue curve. Additional constraints were employed for our experiments to ensure that the SoC of the BESS stays in the range 10-90%.

The belief function should yield a set for each point within the PQ profile, indicating all the points the BESS might implement due to uncertainty. However, we assume the BESS is highly controllable and can ignore its uncertainty. Therefore, the belief function is a singleton for each point. For example, the value of the belief function for the implemented point (500 kW, 200 kVar) in Fig. 5.6a is the point itself, indicated by red. Thus, the BESS is a resource with high

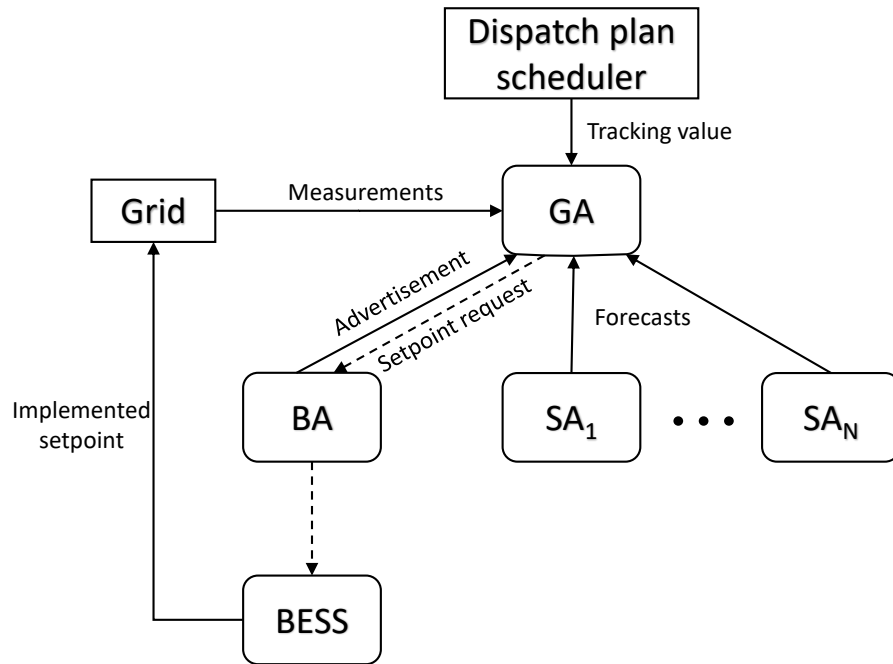


Figure 5.5: COMMELEC decision cycle in the Aigle demonstrator.

controllability (big PQ profile) and low uncertainty (small belief function set).

The opposite case holds for the uncontrollable prosumers in the grid; they have no controllability and non-zero uncertainty. In each node with a stochastic power injection in Fig. 5.3, we install an SA, coded in C++, a software agent that estimates the uncertainty of the node. An example of the PQ profile and the belief function of an SA is shown in Fig. 5.6b for a node that consumes 115 kW of active power and 10 kVar of reactive power. Because the presumption is uncontrollable, the PQ profile advertised by the SA is a single point. The belief function for the measured setpoint is a rectangle constructed by the SA using the method for computing PIs of Chapter 3.

Thus, even though a grid can have different types of energy resources with varying levels of controllability and uncertainty, the format of the messages advertised by the RAs is the same for all of them. This is one of the key features of COMMELEC, contributing to its scalability.

The agents' implementation is optimized to deliver setpoints in the sub-second scale and has been tested for cycles as low as 100 ms. However, we have chosen a cycle of 10 s to fairly compare COMMELEC with an MPC that computes setpoints in the same resolution (see Section 5.2.4). This was done by computing the setpoints every 100 ms in the GA and choosing one setpoint every 10 s in the BA⁴.

⁴Although a better implementation would be to average the grid state every 10 seconds, this simple implementation showed a satisfactory performance because the state of the grid did not change substantially within 10 seconds.

Chapter 5. Experimental Validation of the Proposed Control Framework for Battery Energy Storage Systems

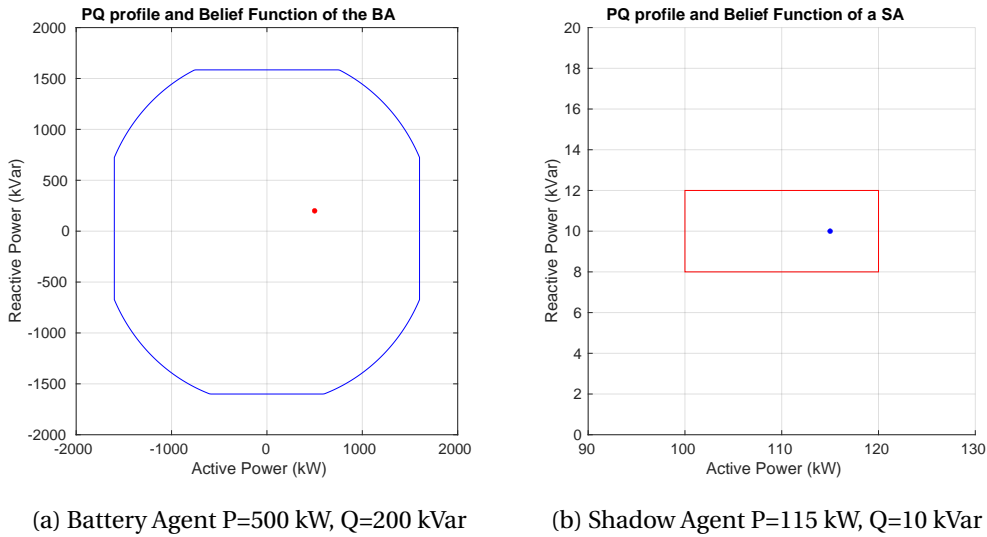


Figure 5.6: Example of a Shadow Agent and the Battery Agent's PQ profile (blue) and Belief Function (red) for the implemented setpoint.

5.2.4 Experimental Results

An example of the COMMELEC framework validation was carried out on Friday, the 19th of March 2021. Fig. 5.7 shows the dispatch plan, the measured slack power with the BESS control contribution, and the same power if the COMMELEC-based BESS control was not activated. The measurements are averaged over 1 minute. The BESS active power and the evolution of the SoC are also shown. Positive power indicates generation from the slack/BESS, while negative power indicates consumption.

COMMELEC can accurately track the dispatch plan for the majority of the experiment. It can be noticed that between 14:20 and 17:40 the tracking of the dispatch plan was missed because the SoC of the battery reached its upper limit of 90%, as shown by Fig. 5.7. The dispatch plan required the slack to produce more power during this period, but the battery could not charge further. As the maximum tracking difference is 100 kW, COMMELEC is expected to track the dispatch plan within this desired bound, assuming the battery has enough controllability. However, when $\text{SoC} > 90\%$, the battery is restricted from consuming power, so COMMELEC loses tracking. It is to be noted that the SoC saturation was due to inaccurate day-ahead forecasts used by the scheduler. Therefore, it could not have been avoided by the RT control.

To better visualize the performance of COMMELEC, Fig. 5.8 compares the CDF of the absolute dispatch tracking error with and without BESS control. It also compares COMMELEC with a state-of-the-art MPC control, employed in the same setup [3], based on the Augmented Relaxed Optimal Power Flow (AR-OPF) approximation [103]. The dispatch tracking error is integrated over 5 minutes, which is the period of the dispatch plan. To have a fair evaluation of the two RT control frameworks, the measurements corresponding to the time window where

5.2 Dispatch Tracking in a Utility-Scale Grid Using the COMMELEC Framework

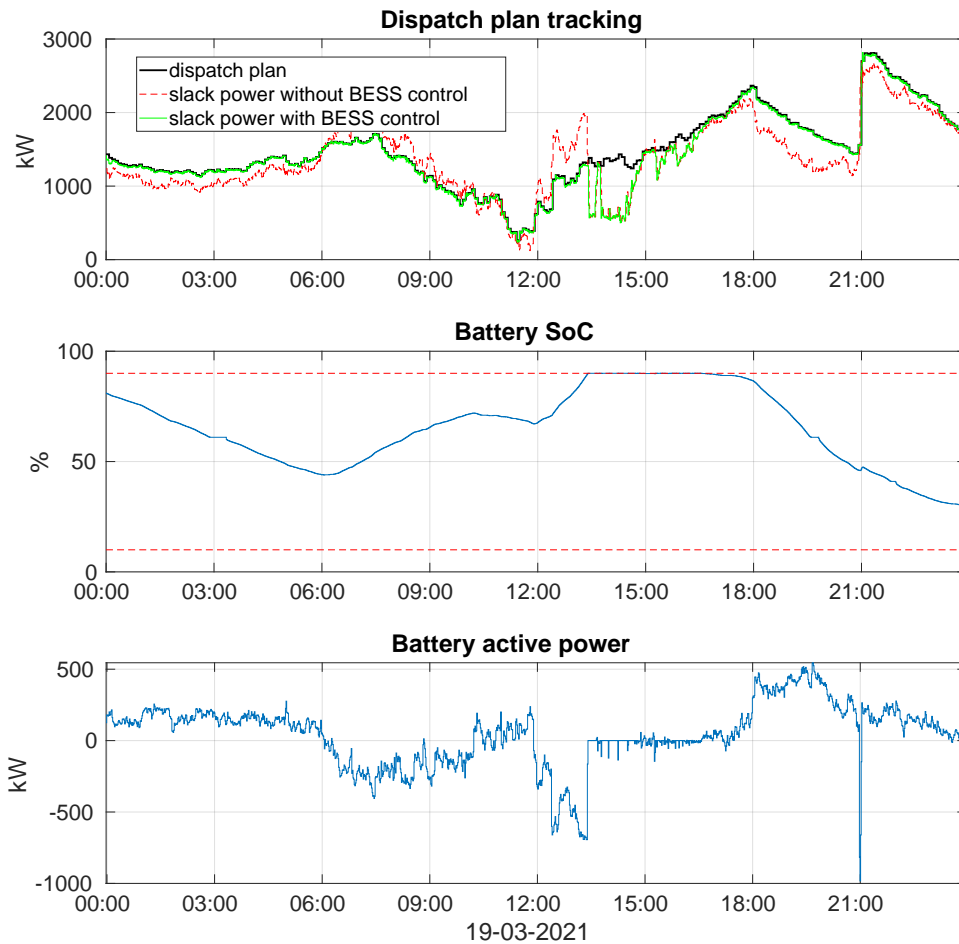


Figure 5.7: Dispatch plan tracking before (top) and after (bottom) COMMELEC control.

the SoC was outside its bounds were not considered when plotting the graph, as the saturation of SoC was caused by the inaccurate forecasts embedded into the computation of the dispatch plan. The graph verifies the theoretical results of Chapter 4 for the slack cost function, as it can be seen that 95% of the measurements were below the 100 kW limit when the COMMELEC control was active.

The performance is also quite similar to that of the MPC. The CDF of the MPC control reaches low confidence levels faster than that of COMMELEC, but COMMELEC performs better for high confidence levels. This means that although the MPC achieves smaller tracking errors most of the day, COMMELEC achieves smaller errors in the worst cases. The benefit of using COMMELEC over MPC is that the former can employ the cost functions developed in Chapter 4 to predict the accuracy of dispatch tracking in advance. On the other hand, the MPC solves a more complicated problem than the ones tackled by this thesis and the theoretical analysis of

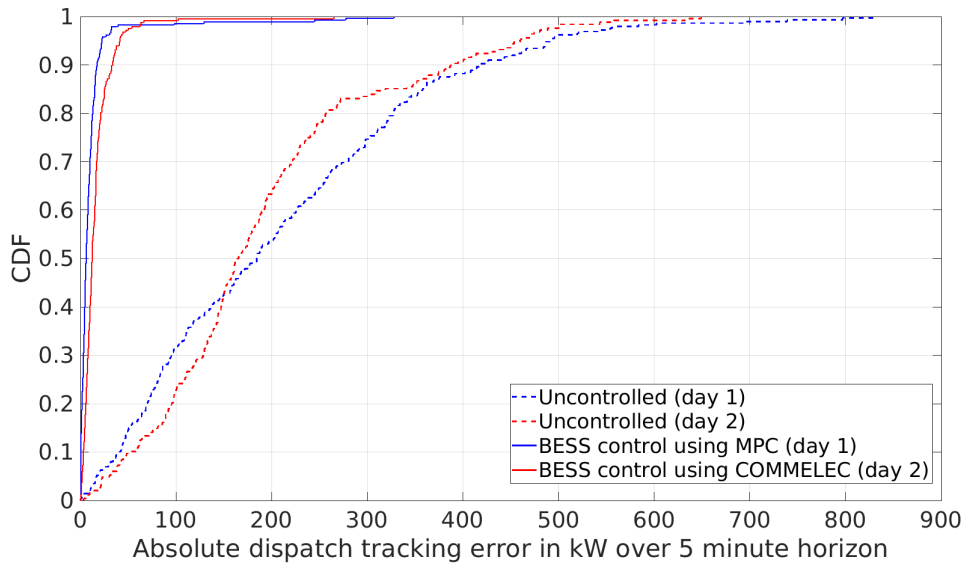


Figure 5.8: Performance comparison between COMMELEC and MPC.

Chapter 4 cannot be applied to it. Therefore, manual tuning of the controller’s weights might still be required in the case of the MPC. Finally, we should mention that the two controls were tested on two separate days, so these experiments are not conclusive of the superiority of one control over the other.

5.3 A Two-Layer Control Approach for the Fair Control of multiple BESSs

The experiment of the previous section showcased how the methods developed in the thesis can be employed in practice to achieve RT dispatch tracking in an ADN. In particular, it showed how the cost functions of Chapter 4 could be used in a state-of-the-art RT control framework (COMMELEC) to have an estimate of the dispatch-tracking error in advance. However, there are still some major points that need to be validated. First, the experiment of Section 5.2.3 used only one BESS. Therefore, it cannot validate the fairness between multiple BESSs, which was a key factor for the method of Chapter 4. Moreover, we did not consider any cases with binding grid constraints, which could affect the performance of the RT control with respect to dispatch tracking or fairness.

Finally, we have only considered so far the single-layer version of the control layer of Figs. 2.4 and 5.1 using only a myopic control. This architecture might not be able to guarantee dispatch tracking and fairness in the long run due to the short horizon of the control. Indeed, we saw in the simulations of Section 4.4 that the proposed cost functions could not guarantee SoC balancing when certain grid constraints were binding. This is a limitation of the proposed method due to the assumption of the short optimization horizon. More precisely, the cost

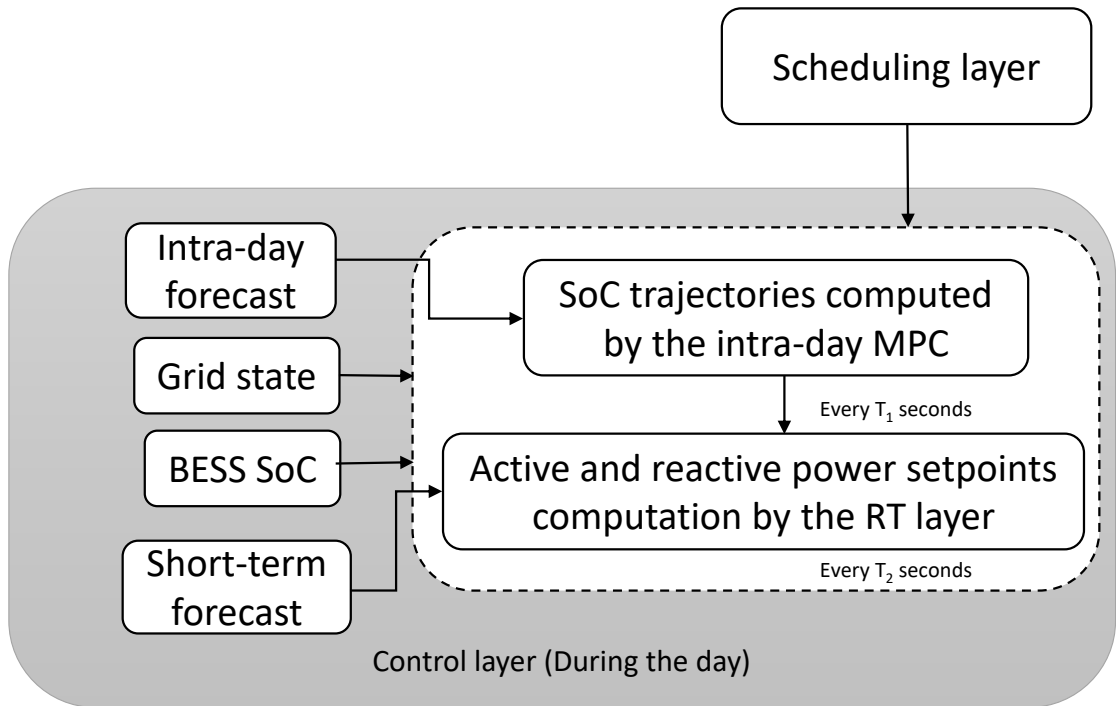


Figure 5.9: Schematic diagram of the control framework.

functions of the two BESSs were fixed throughout the simulation, so the control could not fix any mismatch between their SoCs caused by the binding constraints. Therefore, a supervisory layer is needed to adapt the BESSs' cost functions.

In this section, we address these issues by proposing a control framework comprising two layers based on the architecture of Fig. 2.5. The proposed layer achieves dispatch tracking and SoC fairness under normal operating conditions. It is also validated in a case where grid constraints are binding, where it achieves the best effort in terms of fairness.

5.3.1 Control Framework

As in the rest of the thesis, we assume a given scheduling, or day-ahead layer, and design the control layer. For the control framework of this section, we employ the benefits of both MPC and myopic optimization-based control, as explained in Section 2.1.2. The MPC can handle long-term objectives, whereas the myopic control can be solved efficiently. The proposed control layer, which is inspired by [19], is an example of the general case of Fig. 2.4 and is depicted in Fig. 5.9⁵.

The purpose of the control loop is to follow the dispatch plan computed by the scheduler while guaranteeing the fair usage of the BESSs. The intra-day layer is a model predictive control (MPC) that computes every T_1 seconds (typically 5-15 minutes) the expected trajectories of

⁵The output of the scheduling layer is computed the same way as in Section 5.2.1.

Chapter 5. Experimental Validation of the Proposed Control Framework for Battery Energy Storage Systems

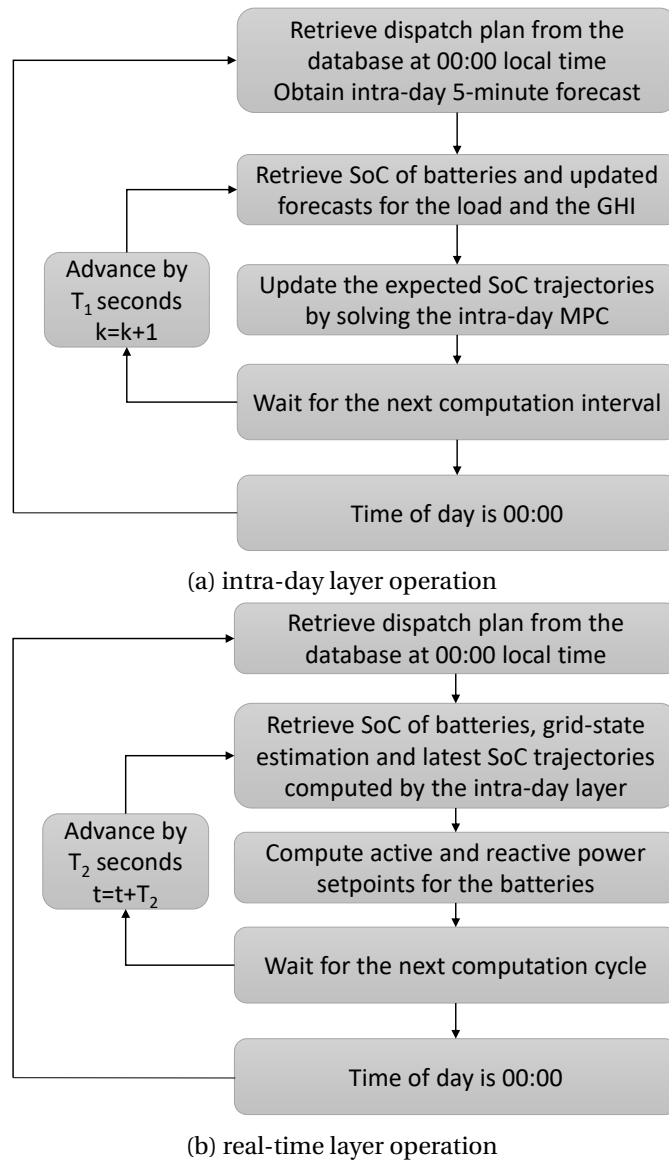


Figure 5.10: Intra-day and real-time operation (executed in parallel).

the BESSs SoC, which should be as close as possible to each other if we want to achieve a fair control. This is done using updated forecasts of the stochastic demand and the generation, as the ones predicted day-ahead might be inaccurate.

The RT layer computes the active and reactive power setpoints for the BESSs every T_2 seconds (typically up to 10 seconds) using a short-term forecast of a T_2 -second horizon and RT estimation of the grid state. The objective of the RT layer is to track the dispatch plan while satisfying the fairness of the SoCs as computed by the MPC and ensuring grid safety with respect to nodal voltages and branch currents.

The operation of the two layers, executed in parallel, is depicted in Fig. 5.10. Every T_1 seconds,

5.3 A Two-Layer Control Approach for the Fair Control of multiple BESSs

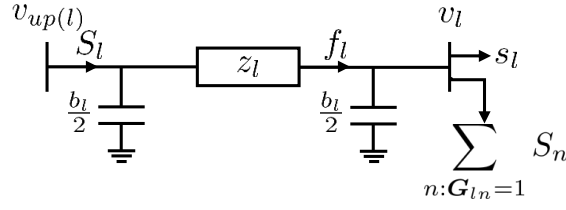


Figure 5.11: π model of a branch

the intra-day layer solves an MPC to compute the expected powers and SoC trajectories of the BESSs for all given scenarios until the end of the day. The RT layer receives as input the dispatch plan computed day-ahead and the expected trajectories of the SoCs computed by the intra-day layer. It then solves an optimization problem every T_2 seconds to compute each BESS's active and reactive power setpoint. Its goal is to track the dispatch plan and a target SoC trajectory for each BESS. Fairness is ensured in the long run by setting the same target SoC for all BESSs (more details are given in Section 5.3.3). Section 5.3.2 describes in detail the formulation of the MPC problem solved by the intra-day layer. Section 5.3.3 explains how the generalized RT framework proposed in Section 2.2.1 is adapted to follow the decisions made by the intra-day layer.

5.3.2 Intra-Day MPC

We consider the set of time indices $\mathcal{K} = \{0, \dots, k^{end}\}$ denoting the T_1 -second intervals where the intra-day MPC is run. At time index k , we assume to be given D scenarios labeled as $d = 1, \dots, D$ of the nodal prosumption for all indices $\kappa = k, \dots, k^{end}$. The method for computing the scenarios is described in Section 5.3.5. The goal at time index k is to compute the expected power of the batteries and the respected SoC trajectories for all scenarios $d = 1, \dots, D$ for the indices $\kappa = k, \dots, k^{end}$.

Grid Model

We consider a generic medium or low-voltage ADN with K buses and L branches. Each branch l is modeled with the π -model equivalent shown in Fig. 5.11. The node at the top of branch l is indicated by $up(l)$, while the node at the bottom is indicated simply by l . $z_l = r_l + jx_l$ and b_l are the branch's longitudinal impedance and shunt capacitance. However, for the case of low-voltage ADNs, shunt elements can be neglected, thus simplifying the problem's constraints, as will be made clear in the section "Constraints". \mathbf{G} denotes the adjacency matrix. For every branch l , scenario d , and time κ , we define the following quantities: $S_{l,\kappa}^d = P_{l,\kappa} + jQ_{l,\kappa}$ is the apparent power entering the branch from the top. $i_{l,\kappa}^d, i_{l,\kappa}^{b,d}$ are the currents entering branch l from the top and bottom respectively, $f_{l,\kappa}^d$ is the square of the current flowing through z_l and I_l^{max} is the ampacity limit of the branch. $v_{l,\kappa}^d$ is the square of the voltage magnitude and v^{min}, v^{max} are its respective bounds. $s_{l,\kappa}^d = p_{l,\kappa}^d + jq_{l,\kappa}^d$ is the total power injected at bus l .

Chapter 5. Experimental Validation of the Proposed Control Framework for Battery Energy Storage Systems

BESS Model

For every battery $i = 1, \dots, N_B$ and for every scenario d and time κ , we define the following: $s_{i,\kappa}^{B,d} = p_{i,\kappa}^{B,d} + jq_{i,\kappa}^{B,d}$ is the power injected by the battery into the grid⁶, $SoC_{i,\kappa}^d$ is its SoC, normalized by its energy capacity E_i^{max}

We use the equivalent diagram of Fig. 2.9 introduced in Section 2.4.1 to model the losses inside a battery and its AC/DC interface. Assuming a battery at node l , we represent the losses of the battery with a virtual branch l' with series resistance R_l^{bess} between node l and a virtual node l' . The power of the battery $s_l^B = p_l^B + jq_l^B$ computed by the MPC is injected at bus l , while an ideal, lossless battery is placed at bus l' . This allows the SoC of the battery to be computed for a lossless system within time T_1 as follows:

$$SoC_{i,\kappa+1} = SoC_{i,\kappa} - \frac{T_1 p_{i,\kappa}^B}{E_i^{max}} \quad (5.3)$$

where E_i^{max} is the battery's energy capacity.

Objective

The objective to be minimized at index k is the following:

$$C_k = \sum_{\kappa=k}^{k^{end}} \left\{ \sum_d \left[w_0 |P_{\kappa}^{DP} - P_{0,\kappa}^d| + w_1 \left(\sum_{i=1}^{N_B} (SoC_{i,\kappa}^d - \frac{1}{N_B} \sum_{j=1}^{N_B} SoC_{j,\kappa}^d) \right) \right] + w_2 |F_{\kappa}| \right\} \quad (5.4)$$

s.t. (5.5) – (5.18)

The first term of the objective, with weight w_0 , minimizes the absolute difference between the realization of the power imported/exported to the primary grid P_0 , i.e., the ADN power flow at its slack bus, and the dispatch plan P^{DP} . The second term, with weight w_1 , aims at SoC balancing. It minimizes the difference between the SoCs of the batteries by minimizing the difference between the SoC of each battery and the average SoC. The purpose of the final term, with weight w_2 , is to ensure that the batteries have enough energy capacity at the end of the day to serve the following day. Instead of placing a hard constraint at the SoC of the batteries, which would limit the system's flexibility, we employ the technique of the offset profile defined in [13]. As will be made clear in the following section, by minimizing the absolute value of the offset profile F_{κ} , the aggregated power of the batteries is kept as close as possible to the variability of the uncertainties. This way, there is no unnecessary overcharging or over-discharging of the batteries.

It is obvious that the choice of the weights in (5.4) affects the problem's solution. However, the exact relation among them is not crucial because (i) the batteries do not directly implement the output of this problem, and (ii) the problem is solved every few minutes. Regarding point

⁶Positive power indicates discharging.

5.3 A Two-Layer Control Approach for the Fair Control of multiple BESSs

(i), as explained in Section 5.3.1, the only output of the MPC needed by the RT layer is the expected trajectories of the SoCs of the batteries. Regarding point (ii), because the problem is solved every few minutes, what truly matters is the direction of change of the expected trajectories. Assuming we fix weight w_0 at (5.4), the choice of w_1 should not affect dispatch tracking unless the SoC constraints are binding. The choice of w_2 will affect the remaining reserve in the batteries at the end of the day, but as long as the direction of the SoC is correct, the exact choice is not crucial. Dispatching is a priority for our experiment, so we choose a very large value $w_0 = 1000$. For the other two objectives, we choose $w_1 = w_2 = 0.01$. As will be verified by our experiments in Section 5.3.6, even such small weights are enough to achieve fairness. On the other hand, the weights in the objective of the RT control are computed using the novel method of Chapter 4.

Constraints

The problem's constraints are defined in [91] and repeated here for completeness. They are the following for branches $l = 1, \dots, L$, time indices $\kappa = k, \dots, k^{end}$, scenarios $d = 1, \dots, D$, and batteries $i = 1, \dots, N_B$.

a) Power Flow Equations $\forall \kappa, d, l$

$$P_{l,\kappa}^d = \sum_{n:G_{ln}=1} P_{n,\kappa}^d + p_{l,\kappa}^d + r_l f_{l,\kappa}^d \quad (5.5)$$

$$Q_{l,\kappa}^d = \sum_{n:G_{ln}=1} Q_{n,\kappa}^d + q_{l,\kappa}^d - (v_{up(l),\kappa}^d + v_{l,\kappa}^d) b_l / 2 + x_l f_{l,\kappa}^d \quad (5.6)$$

$$f_{l,\kappa}^d = \|S_{l,\kappa}^d + j v_{up(l),\kappa}^d b_l / 2\| / v_{up(l),\kappa}^d \quad (5.7)$$

b) Voltage constraints $\forall \kappa, d, l$

$$v_{l,\kappa}^d = v_{up(l),\kappa}^d - 2\Re\{z_l^* (S_{l,\kappa}^d + j v_{up(l),\kappa}^d b_l / 2)\} + \|z_l\|^2 f_{l,\kappa}^d \quad (5.8)$$

$$v_{up(l),\kappa} = 1, v^{min} \leq v_{l,\kappa}^d \leq v^{max} \quad (5.9)$$

c) Ampacity Constraints⁷ $\forall \kappa, d, l$

$$\Re\{i_{l,\kappa}^d\} = \frac{P_{l,\kappa}^d}{\sqrt{v_{up(l),\kappa}^d}}, \Im\{i_{l,\kappa}^d\} = \frac{Q_{l,\kappa}^d}{\sqrt{v_{up(l),\kappa}^d}} \quad (5.10)$$

$$\Re\{i_{l,\kappa}^{b,d}\} = (P_{l,\kappa}^d - r_l f_{l,\kappa}^d) / \sqrt{v_{l,\kappa}^d} \quad (5.11)$$

$$\Im\{i_{l,\kappa}^{b,d}\} = \Im\{i_{l,\kappa}^d\} + (v_{up(l),\kappa}^d + v_{l,\kappa}^d) \frac{b_l}{2\sqrt{v_{l,\kappa}^d}} - \frac{x_l f_{l,\kappa}^d}{\sqrt{v_{l,\kappa}^d}} \quad (5.12)$$

⁷For the case of low-voltage ADNs, b_l can be set to 0 in Constraint (5.12).

Chapter 5. Experimental Validation of the Proposed Control Framework for Battery Energy Storage Systems

$$\|i_{l,\kappa}^d\| \leq I_l^{max}, \|i_{l,\kappa}^{b,d}\| \leq I_l^{max} \quad (5.13)$$

d) Battery Constraints $\forall \kappa, d, i$

$$SoC_{i,k}^d = SoC_{i,k}^{measured} \quad (5.14)$$

where $SoC_{i,k}^{measured}$ is the measured SoC of the battery at the initial time k .

$$SoC_{i,\kappa+1}^d = SoC_{i,\kappa}^d - \frac{T p_{i,\kappa}^{B,d}}{E_i^{max}} \quad (5.15)$$

$$0.2 \leq SoC_{i,\kappa}^d \leq 0.9 \quad (5.16)$$

$$(p_{i,\kappa}^{B,d}, q_{i,\kappa}^{B,d}) \in \mathcal{A}_i \quad (5.17)$$

where \mathcal{A}_i is a linearized approximation of the constraint set of the battery.

e) Offset Profile $\forall \kappa$

$$\sum_{i,d} p_{i,\kappa}^{B,d} - F_\kappa \leq \sum_{n=1}^K \max_d \{p_{n,\kappa}^{uc,d}\} - \min_d \{p_{n,\kappa}^{uc,d}\} \quad (5.18)$$

$$\sum_{i,d} p_{i,\kappa}^{B,d} - F_\kappa \geq \sum_{n=1}^K \min_d \{p_{n,\kappa}^{uc,d}\} - \max_d \{p_{n,\kappa}^{uc,d}\}$$

where $p_{n,\kappa}^{uc,d}$ is the power injection of all uncontrollable resources at node n for scenario d and time κ . By minimizing the absolute value of F_κ , the sum of the BESSs' powers is kept as close as possible to the total uncertainties in the system (right-hand side of the two inequalities). This means that the BESSs should be used to balance the uncertainties in the system and avoid any unnecessary charging or discharging.

Non-Convexity of the Problem

The problem to be solved at index k is the following:

$$\begin{aligned} & \min_{S_{l,\kappa}^d, SoC_{i,\kappa}^d, F_\kappa} \quad (5.4) \\ & \text{s.t.} \quad (5.5) - (5.18) \end{aligned} \quad (5.19)$$

Problem (5.19) is non-convex, because of the Constraints (5.7) and (5.10)-(5.12). To solve the problem, we use CoDistFlow, which is an iterative process proposed in [91] that converges to an approximate solution of (5.19) under mild conditions on the nodal-admittance matrix that can be verified a priori. At each iteration of the algorithm, the problem is convexified using an approximation based on DistFlow [90], denoted as improved DistFlow (iDF). First, DistFlow ignores the losses in the lines' longitudinal-impedances $r_l f_{l,\kappa}^d$ and $x_l f_{l,\kappa}^d$; therefore, Constraint (5.7) is removed. To account for the losses, iDF replaces the loss terms $f_{l,\kappa}^d$ and $x_l f_{l,\kappa}^d$ with correction terms for the active and reactive power losses, denoted by $\hat{p}_{l,\kappa}^d$ and $\hat{q}_{l,\kappa}^d$ respectively. It also replaces the term $\|z_l\|^2 f_{l,\kappa}^d$ in (5.8) with the voltage correction terms $\hat{v}_{l,\kappa}^d$

5.3 A Two-Layer Control Approach for the Fair Control of multiple BESSs

and approximates the voltage magnitudes $\sqrt{v_{l,k}^d}$ with constants $\tilde{v}_{l,k}^d$, thus making the problem convex. After solving the convex version of Problem (5.19), a load flow (LF) module computes a better estimation of the values of the correction terms and the voltage magnitudes. The output of the LF module is fed back to the iDF module, and the cycle continues until the solution satisfies the problem constraints within a given tolerance.

5.3.3 Real-Time Control

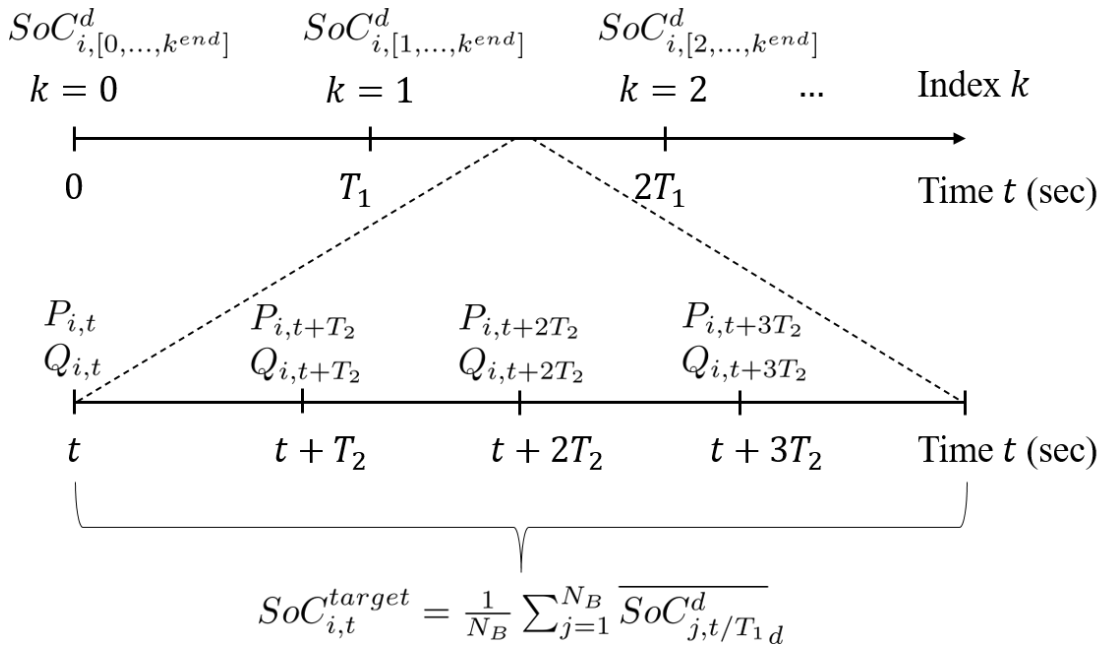


Figure 5.12: Intra-day (top) and real-time (bottom) time axis for a given time slice.

The RT control is performed by solving the optimization problem introduced in Section 2.2.1. Unlike COMMELEC, which uses multiple agents, the problem is solved by a single agent/controller that knows the state of the grid and of the BESSs. Also, in this section, the optimization problem can be solved by a convex optimization problem instead of approximating the solution with gradient descent, as the time resolutions considered (up to 10 seconds) are enough to find the problem's solution with acceptable accuracy.

The cost functions follow the guidelines of Chapter 4 and are the same as in the simulations of Section 4.4. The cost functions for the BESSs' objectives are in the form of Equation (4.3), and their preference is computed by Equation (4.29). Because one of the goals of the RT layer is to follow the expected SoC trajectories computed by the intra-day layer, this target should be incorporated into the BESSs' cost functions. We assume that the median of the SoC trajectories over all scenarios d is a good indicator of the expected SoC trajectory of each battery. Therefore, we take as the target SoC for the RT control of battery i at time t the

Chapter 5. Experimental Validation of the Proposed Control Framework for Battery Energy Storage Systems

following:

$$SoC_{i,t}^{target} = \frac{1}{N_B} \sum_{j=1}^{N_B} \overline{SoC_{j,t/T_1}^d} \quad (5.20)$$

where $\overline{\{\cdot\}}_d$ denotes the median over all scenarios d . The value of $SoC_{j,k}^d$ at $k = t/T_1$ is computed by interpolating the SoC trajectories computed by the MPC. We decided to average overall batteries for better SoC balancing. Indeed, the intra-day MPC might compute slightly different trajectories because the initial SoCs of the batteries might be different. By averaging over all batteries, they will have the same target trajectory, and the RT control will steer the SoCs towards the same value.

The interaction between the intra-day and the RT layer is depicted in Fig. 5.12. At time index k , the intra-day layer initiates the computation of the expected trajectories $SoC_{i,[k,\dots,k^{end}]}^d$. At time t seconds, the RT layer initiates the computation of the power setpoints $(P_{i,t}, Q_{i,t})$, $i = 1, \dots, N_B$ of the batteries. The inputs of the control are (i) the grid-state estimation and the measured SoC of the batteries at t , (ii) the dispatch plan computed at $k = \lfloor t/T_1 \rfloor$ and (iii) the target SoC trajectories computed by (5.20). As a fallback strategy, in case the computation of the MPC at $k = \lfloor t/T_1 \rfloor$ has not finished by time t , then Formula (5.20) takes as input the values of $SoC_{i,k}^d$ computed at index $k - 1$.

Regarding the grid objectives, we use again the cost functions defined in Section 2.3. The hard voltage tolerance in our experimental setup is $\beta_{hard} = 0.1$; therefore, the soft voltage tolerance, as defined in Section 4.3.2, is chosen at $\beta_{soft} = 0.09$. As in the previous experiment, the soft current tolerance is chosen at $\gamma_{soft} = 0.9$. In the experiment of Section 5.2, the uncertainty of the system was taken care of by COMMELEC's belief function. The belief function was used to ensure that the grid's constraints were not violated for any possible realization of the uncertainties. In the RT control of this section, the uncertainty can be incorporated in the computation of the weights according to Theorem 4.3 and Formula (4.23). This way, if the upper or lower bound of the expected voltage or current approaches the respective upper or lower bound, the weight of the relevant objective will be increased to keep the grid state within the bounds.

Regarding the slack-active-power-tracking and slack-reactive-power tolerance, we use the idea introduced in the simulations of Section 4.4.2. The idea is that the slack tolerances should be at least equal to the uncertainty in the forecast of the slack power so that they can be guaranteed with a given confidence level. Therefore, we choose:

$$|P_s - P^{DP}|_{max} = |\Delta P_s|_{max} \quad (5.21)$$

$$|Q_s|_{max} = |\Delta Q_s|_{max} \quad (5.22)$$

where $|\Delta P_s|_{max}$ and $|\Delta Q_s|_{max}$ are the estimated uncertainties in the slack active and reactive

5.3 A Two-Layer Control Approach for the Fair Control of multiple BESSs

power, respectively, computed as follows:

$$|\Delta P_s|_{max} = \sum_{u=1}^U |K_{\mathcal{P}_u}^{P_s} \Delta \mathcal{P}_u| + |K_{\mathcal{Q}_u}^{P_s} \Delta \mathcal{Q}_u| \quad (5.23)$$

$$|\Delta Q_s|_{max} = \sum_{u=1}^U |K_{\mathcal{P}_u}^{Q_s} \Delta \mathcal{P}_u| + |K_{\mathcal{Q}_u}^{Q_s} \Delta \mathcal{Q}_u| \quad (5.24)$$

where $K_{\mathcal{P}_u}^{P_s}, K_{\mathcal{Q}_u}^{P_s}$ are the sensitivities of the slack active-power with respect to the stochastic active and reactive power injection u and $K_{\mathcal{P}_u}^{Q_s}, K_{\mathcal{Q}_u}^{Q_s}$ are the sensitivities of the slack reactive-power with respect to the same stochastic power injection. It should be noted that this method assumes that the system's sensitivities remain the same between two consecutive control cycles, which is a valid assumption because the control period is small. The uncertainty bounds $\Delta \mathcal{P}_u, \Delta \mathcal{Q}_u$ can be estimated using the method of Chapter 3, as will be explained shortly.

Instead of using the full capability curve of the BESSs, we use an approximate box constraint as in the simulations of Section 4.4.2. As already discussed in Section 2.4.1, this is an accurate approximation of the capability curve of a real BESS. In addition to the capability curve, the BESS's constraints should ensure that its SoC stays in the range [0.2, 0.9]. Therefore, the limits for the active power are defined as follows:

$$\begin{aligned} P_i^{max} &= \frac{\sqrt{2}}{2} S_i \mathbb{1}_{SoC_i > 0.2} \\ P_i^{min} &= -\frac{\sqrt{2}}{2} S_i \mathbb{1}_{SoC_i < 0.9} \end{aligned} \quad (5.25)$$

and the limits of the reactive power are:

$$\begin{aligned} Q_i^{max} &= \frac{\sqrt{2}}{2} S_i \\ Q_i^{min} &= -\frac{\sqrt{2}}{2} S_i \end{aligned} \quad (5.26)$$

5.3.4 Experimental Setup

Grid Topology

The proposed framework is validated on the EPFL smart-grid platform. The topology is comprised of both 420 V (LV) and 21 kV (MV) parts, interconnected via two transformers with a rating of 630 kVA (see Fig. 5.13). Local power is generated by an uncontrollable PV of 16 kWp. The consumers include two office loads with a maximum consumption of 50 kW and 8 kW, respectively, and a level 3 electric vehicle (EV) charging station (CS) with a maximum consumption of 150 kW.

Chapter 5. Experimental Validation of the Proposed Control Framework for Battery Energy Storage Systems

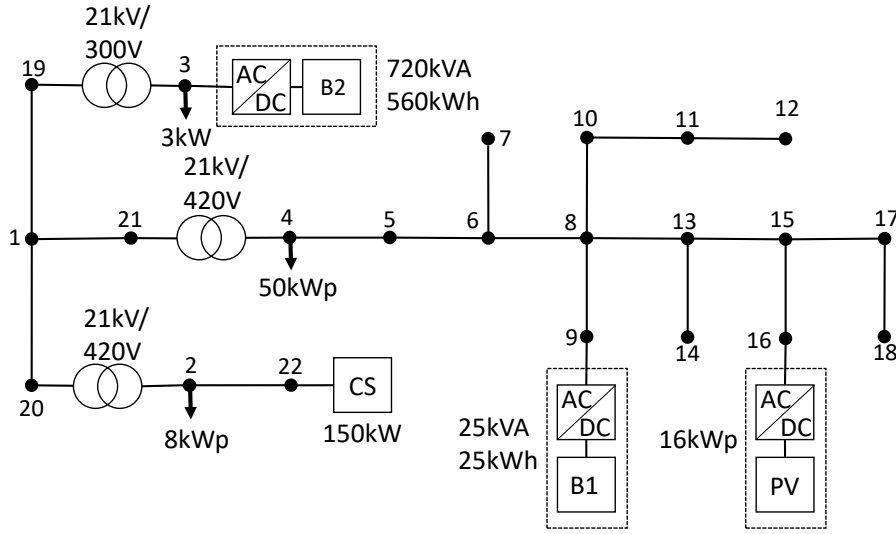


Figure 5.13: Topology of the distribution network at EPFL. Bus 1 is the slack bus.

The controllability of the system is provided by two BESSs connected via DC/AC converters. The technical specifications of the two BESSs are shown in Table 5.2. The two BESSs are a 25 kVA/25 kWh, labeled as BESS 1, and a 720 kVA/560 kWh, labeled as BESS 2, respectively. BESS 2 is connected to the grid via a step-up 0.3/21 kV transformer with a rating of 630 kVA and incorporates a heating, ventilation, and air conditioning (HVAC) system, which consumes approximately 3 kW⁸. As stated in Section 4.2, the proposed method assumes that the energy capacity of the BESS is proportional to its rated power. For this reason, and to avoid operating BESS 2 at the boundary of its capability curve, we limit its apparent power to 560 kVA⁹.

The control of the intra-day layer is performed every 5 minutes (i.e. $T_1 = 300$), and the RT control is performed every 5 seconds (i.e. $T_2 = 5$). The SoC of the BESSs required by the RT optimization problem is estimated by the respective battery management system (BMS).

Metering Infrastructure

RT estimation of the grid state is provided by a similar infrastructure as the one in Section 5.2.3. A subset of the PMUs is located in the DESL local network and stream their measurements to a workstation that runs the state estimator via ethernet cables (see Fig. 5.14). The rest of the PMUs stream their measurements via a public 4G network. The converters of the two BESSs are also located in the same network as the state estimator. The MPC and the RT control are executed in MATLAB in a workstation with an Intel Core i9-12900K processor at 3.2GHz and 32GB of RAM. For the MPC, we use the YALMIP toolbox to construct the problem with the Mosek solver, whereas for the RT control we use the built-in *fmincon* function of MATLAB.

⁸This load has been taken into account in the control.

⁹This is not a strict requirement. The method has been verified with simulation in cases where the ratios of rated powers to energy capacities are not exactly equal.

5.3 A Two-Layer Control Approach for the Fair Control of multiple BESSs

Table 5.2

TECHNICAL SPECIFICATIONS OF BESSs USED FOR THE EXPERIMENTS OF SECTION 5.3 (ADAPTED FROM [4]).

| Parameter | Value |
|--------------------------------|------------------------------|
| Nominal capacity | 25 kW/25 kWh |
| Number of racks | 1 |
| Number of modules per rack | 23 in series |
| Cells configuration per module | 20s3p |
| Total number of cells | 780 |
| Cell nominal voltage | 2.3 V (limits 1.7 V - 2.7 V) |
| Cell nominal capacity | 16 Ah |
| Cell chemistry | Lithium-titanate |

(a) BESS 1

| Parameter | Value |
|--------------------------------------|------------------------------|
| Nominal capacity | 720 kW/500 kWh |
| Voltage at the grid connection point | 20 kV |
| Number of racks | 9 in parallel |
| Number of modules per rack | 15 in series |
| Cells configuration per module | 20s3p |
| Total number of cells | 8100 |
| Cell nominal voltage | 2.3 V (limits 1.7 V - 2.7 V) |
| Cell nominal capacity | 16 Ah |
| Cell chemistry | Lithium-titanate |

(b) BESS 2

To get the one-step-ahead point forecasts required by the RT control (see Section 2.2.1), we use a persistent forecaster on the RT power measurements provided by the infrastructure, aggregated every 5 sec. To estimate the uncertainty of the stochastic power injections required by (5.23) and (5.24), we use the method of Chapter 3. We use model B (which is applied to the differentiated time series) and group all the measurements in one cluster because this was shown to be the best choice for the time resolutions that interest us (5-10 sec). The target confidence level is 99%, and the forgetting time constant is 60 s^{10} .

¹⁰In the simulations of Chapter 3, this choice was proven too small to compute PIs with high accuracy. However, high accuracy is not crucial in this experiment because we only consider soft constraints. A small forgetting time constant is a better choice because the PIs will adapt more quickly to large power changes, such as the connection and disconnection of an electric vehicle.

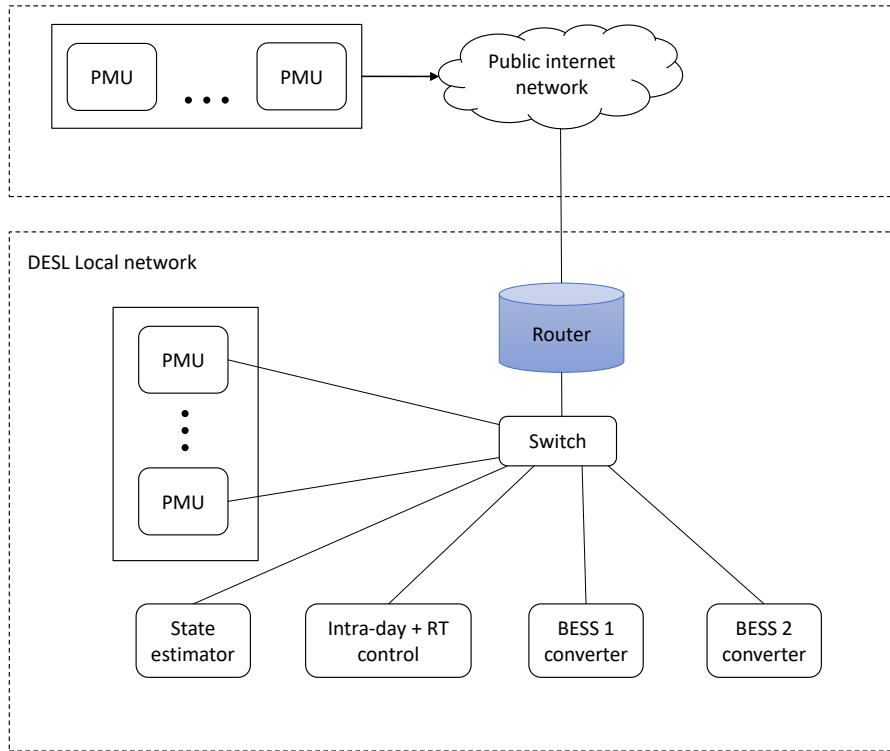


Figure 5.14: IT infrastructure of the EPFL smart-grid platform.

5.3.5 Intra-Day Forecasting

PV Generation

To forecast the PV generation required by the intra-day MPC, we use GHI forecasts provided by a commercial service called SoDa¹¹. It provides forecasts for the GHI for the present and the next day at a 30-minute resolution, which is updated every 6 hours. The GHI forecasts are fed into a physics-based model [104] to generate three scenarios for the generation of each PV, using the median and the 5th and 95th percentiles of the GHI. The 30-minute forecasts are linearly interpolated to get the 5-minute forecasts required by the MPC.

Load Demand

For the two loads, we use the method described in [4]. We first cluster historical measurements, aggregated every 5 minutes, based on the type of day. We use four clusters: Mondays to Thursdays in one cluster and Fridays, Saturdays, and Sundays in three separate clusters. Then, we fit each day type into a multivariate Gaussian model, with the following steps: (i) we subtract from all historical measurements the mean of their corresponding cluster, (ii) we compute the time cross-correlation matrix of the zero-mean power profiles, (iii) we sample

¹¹<https://www.soda-pro.com/soda-products/ai-forecast>

5.3 A Two-Layer Control Approach for the Fair Control of multiple BESSs

two scenarios for each load by taking the 5th and the 95th percentile of the time-correlated multivariate-Gaussian distribution model and, finally, (iv) we generate the demand scenarios by adding the cluster mean.

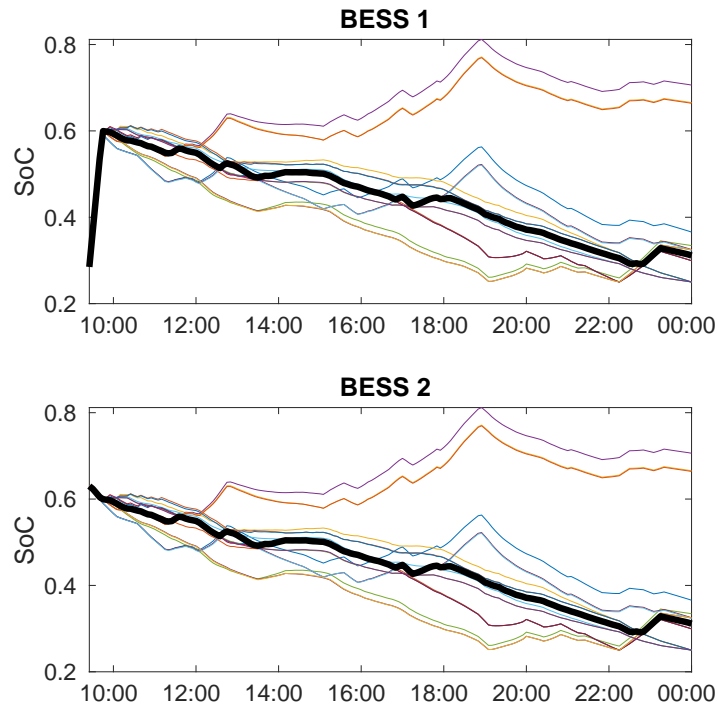


Figure 5.15: Expected SoC trajectories computed by the intra-day MPC for the first experiment. Each colored line corresponds to one scenario, whereas the bold black line indicates the median trajectory used by the RT control.

Electric-Vehicle Charging

For the scenarios of EV charging, we use another method developed in [4]. It consists in training a model to forecast the EV user behavior for the following day, using historical data for the number of EV charging sessions per day, the EVs' arrival and departure times, the initial and final, i.e., target, SoCs of EVs' batteries, the EVs' battery capacities, and the EVs' minimum and maximum active power injections. We first filter the available dataset by keeping the observations that match the day we want to forecast based on season and type of day. Then, we fit the remaining observations into three models, namely (i) a multivariate Gaussian mixture model (GMM) of K dimensions, where K is the number of features, (ii) K univariate GMMs and (iii) a mix of the two which is achieved by splitting the features into groups based on their degree of correlation and fitting a GMM for each group. From the three models, we select the one that best fits the historical observations based on the value of various statistical metrics,

Chapter 5. Experimental Validation of the Proposed Control Framework for Battery Energy Storage Systems

such as accuracy, bias, and the Kolmogorov–Smirnov test. We then sample 80 scenarios¹² of EV arrivals and charging from the selected model, and finally, we keep the ones with (i) the minimum, (ii) the maximum, and (iii) the median total energy consumed by the EVs. Therefore, given the two scenarios for the loads and three for the PV generation, we have 18 scenarios.

5.3.6 Experimental Results

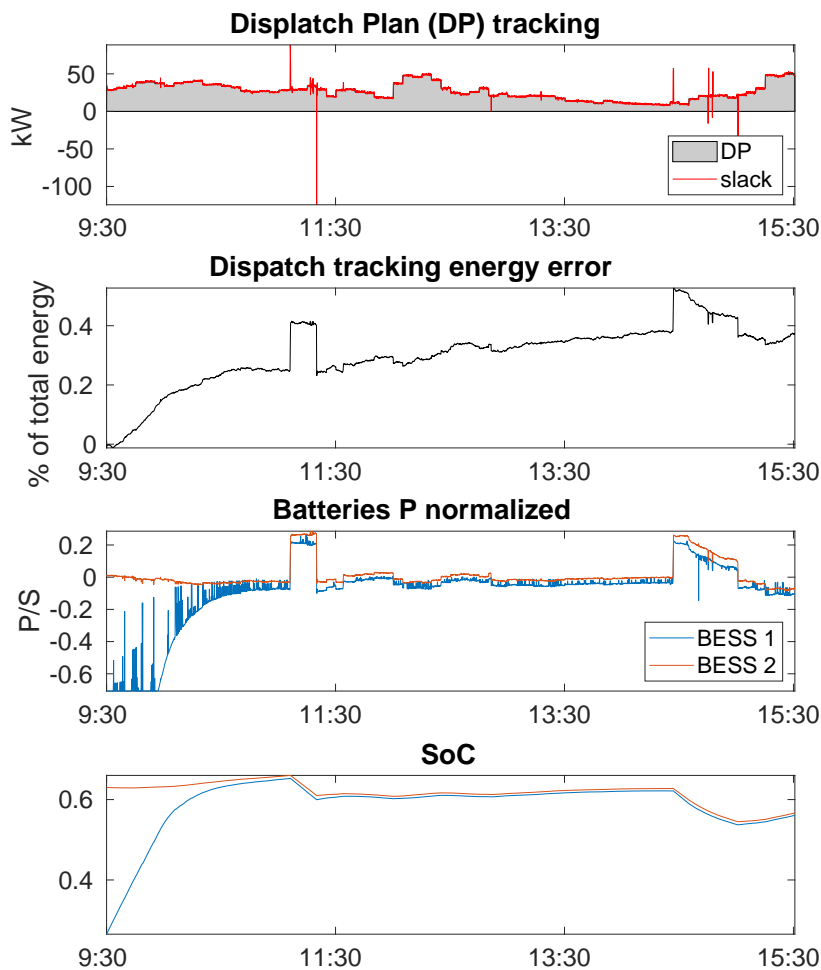


Figure 5.16: Dispatch plan tracking and BESS power and SoC for the first experiment. Positive power indicates the importing of energy from the upper grid at the top plot and the discharging of BESS at the third plot.

¹²The 80 scenarios were used to compute the dispatch plan, but because there are stricter time constraints in intra-day, we choose only three of those scenarios for the MPC.

5.3 A Two-Layer Control Approach for the Fair Control of multiple BESSs

First Experiment: SoC Balancing

We performed an experiment for 6 hours with the above setup, starting at 9:30 a.m. on Wednesday, 27/09/2023. The initial SoCs of the two BESSs estimated by the BMS were $SoC_1 = 0.35$ for BESS 1 and $SoC_2 = 0.71$ for BESS 2. Fig. 5.15 shows the expected SoC trajectories computed by the intra-day MPC at the first iteration. The MPC instruct BESS 1 to charge at the beginning of the experiment until the two SoCs reach the same value, which is kept throughout the day.

Fig. 5.16 shows the dispatch plan tracking and the power and SoC of the BESSs. BESS 1 started charging at maximum power, which is $\sqrt{2}/2 \cdot S$, as predicted by the MPC. After one and a half hours, the two SoCs reached the same value, and the fairness continued throughout the day. It is worth noting that dispatching was not compromised even when the two SoCs were very different. After 6 h of operation, the dispatch-tracking energy error was 0.4% (expressed as a percentage of the total energy flow at the slack bus), whereas the maximum deviation between the two SoCs after 11:00 h was just 1%. The spikes observed in the slack power were caused by the errors of the persistent forecaster when an EV connected or disconnected to the grid. Because the control actions are taken every 5 seconds and EV connections and disconnections cannot be predicted by the persistent forecaster, the EV can cause a large error in the dispatch tracking until the RT control detects it. However, these mismatches were compensated quickly by the RT control, i.e., in a single RT control cycle.

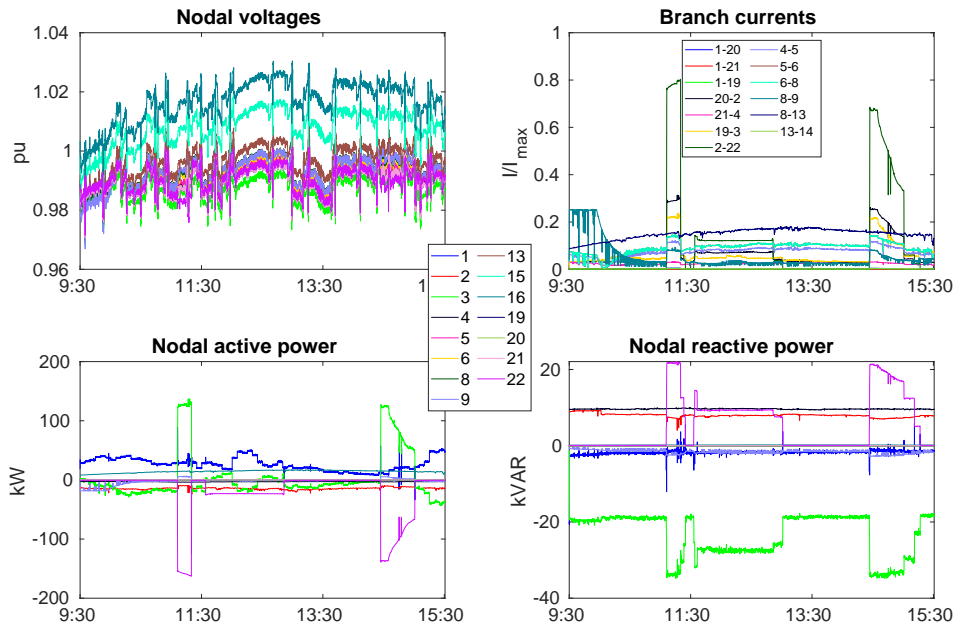


Figure 5.17: Grid state measured by PMUs for the first experiment.

Fig. 5.17 shows the nodal voltages, power injections, and the branch currents measured by

Chapter 5. Experimental Validation of the Proposed Control Framework for Battery Energy Storage Systems

the PMUs during our experiment. To limit the number of plots, we omitted the nodes and branches in Fig. 5.13 that do not contribute to power flows. We observe that all nodal voltages and branch currents were within their respective limits, meaning there were no binding grid constraints. In the following section, we study how the fairness between BESSs might be affected in the presence of binding constraints.

Second Experiment: Operation Under a Grid Binding Constraint

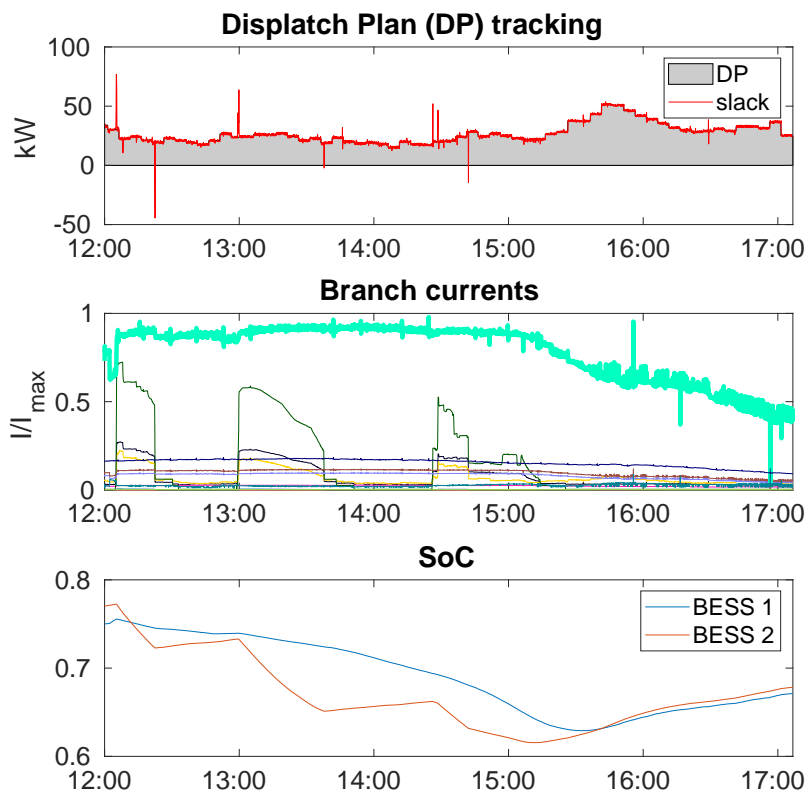


Figure 5.18: Results for the second experiment, with artificially reduced ampacity of branch 6-8. The bold line in the second graph indicates the current of branch 6-8.

For this experiment, we artificially reduced the ampacity of branch 6-8 to 1/8 th of its actual value. We started the experiment at 12:00 h when the PV generation was maximum. The results are shown in Fig. 5.18. At the beginning of the experiment, the two SoCs had the same value. Then, three EVs started charging at 12:05, 12:50, and 14:20. When the first EV arrived, the batteries needed to discharge to continue tracking the dispatch plan. However, BESS 1 could not discharge because the current on branch 6-8 was close to its ampacity. This forced BESS 2 to discharge at a faster rate, which caused an imbalance between the two SoCs. After each car was disconnected, the control tried to bring the two SoCs together as fast as possible

without compromising dispatching or the binding constraint. The fairness could only be guaranteed after 15:30, when all the EVs had stopped charging and the PV generation had been reduced. This experiment verifies that even under binding constraints, the proposed control will make the best effort toward the fairness of BESSs.

5.4 Conclusion and Impact of Experiments

In this chapter, we have seen how the methods presented in the thesis can be employed in practice to control ADNs successfully. First, the two experiments verified the theoretical results of Chapter 4 in an experimental setting. In particular, we saw how the proposed cost functions can achieve dispatch tracking and SoC fairness with high accuracy in two different RT control frameworks without any major modifications to the framework itself. Therefore, the method to design cost functions could be employed by other frameworks as well to prevent the problems of the oracle-based approach discussed in Chapter 2. We also proposed two ways to incorporate the PI computation method of Chapter 3 in RT control frameworks. In COMMELEC, the PIs are incorporated in the belief function, whereas in our proposed RT control, they are incorporated in the computation of the objective's weights. This showcases that the method is flexible and is not tied to a specific framework.

Regarding the intra-day MPC proposed in Section 5.3.2, it should be noted that it is not tied to the RT control framework designed throughout the thesis. The MPC was suggested as an example to enhance the RT control with a longer horizon. However, we leave the possibility that other suitably designed intra-day controls could be used to improve the long-term behavior of the control layer.

6 Conclusion

We have proposed a generic RT optimization-based control to achieve dispatching and fair control of BESSs. We have defined guidelines for the design of cost functions for the various objectives that the control might consider and have proposed a method for dynamically computing their weights. Our guidelines are backed by an extensive theoretical analysis, in which we have proved various properties of the proposed cost functions that imply a balanced control of the controller's objectives. Our method achieves comparable performance to the approaches used by the state-of-the-art, which require manually tuning the controller's parameters and are not practical. We have also shown how the method can be effectively applied by other RT control frameworks in the literature with minimal modifications.

To achieve robust control of ADNs in RT, we have also presented a non-parametric method for computing ultra-short-term prediction intervals, that is, in resolutions as small as 20 ms, of the power prosumption of heterogeneous resources. We have provided an extensive performance evaluation of the algorithm that could help users choose the optimal value of the algorithm's parameters. The method was evaluated on different types of prosumers and aggregation levels and it was shown to compute relatively narrow prediction intervals for confidence levels up to 99.9% for time resolutions up to 10 s. We have also discussed how the prediction intervals can be integrated into the optimization problem of the RT control and, more specifically, in the weight-computation method proposed in the thesis.

Finally, we have demonstrated how the two methods developed in the thesis can be used in an experimental setting. We have considered two control frameworks, COMMELEC, and a novel two-layer framework based on MPC. In the first set of experiments, we have shown how COMMELEC can employ our new cost functions and our method for computing prediction intervals to achieve RT dispatchability of a BESS in an MV utility-scale grid located in Aigle Switzerland. In the second set of experiments, we used the contributions of the thesis as a part of a two-layer framework for the fair control of multiple BESSs. The lower layer is a fast, myopic control that tracks a day-ahead dispatch plan and fairly regulates the batteries' SoCs while ensuring grid safety. The upper layer is an MPC that uses long-term forecasts of the stochastic power injections to supervise and correct the decisions made by the myopic

Chapter 6. Conclusion

layer. This framework was experimentally validated on the EPFL smart-grid platform, using two BESSs of largely different capabilities, namely at 25 kVA/25 kWh and 720 kVA/560 kWh. It achieved dispatching with an error of 0.4% after 6 h of operation and SoC fairness with an accuracy of 99% under normal operating conditions. A stress test was also performed to examine the control's behavior in the presence of binding grid constraints. It was verified that, even in such cases, the control achieves a best-effort SoC fairness without compromising dispatching.

In future research, the limitations of the proposed guidelines for designing cost functions could be addressed. To derive the proposed cost functions, we assumed that the only purpose of the BESSs is to achieve dispatchability. However, this might not always be the case. For example, a BESS that acts as the slack bus could have a different objective than the rest. More work could also be done designing suitable intra-day controls to pair with our proposed RT control framework. More sophisticated frameworks could be developed to incorporate long-term objectives in RT cost functions to guarantee the balanced satisfaction of the objectives in the long run. For example, the objectives' weights could be dynamically computed according to long-term forecasts of the grid's state. The framework proposed in the thesis could be of interest to DSOs that need to control assets controlled by different individuals, in which case fairness might be desirable.

A Proofs of Theorems of Chapter 4

A.1 Proof of Theorem 4.2

We present the proof for Inequality (4.8). Assuming battery cost functions in the form of Equation (4.3), we compute the derivative of the total cost function C_t with respect to P_m , $m \in \{i, j\}$.

$$\frac{\partial C_t}{\partial P_m} = a_P \frac{r_{P,m}}{2} + \frac{\partial J(\mathbf{x}|\mathbf{u})}{\partial P_m} \quad (\text{A.1})$$

where $r_{P,m}$ is defined in (4.1). We consider all the possible cases that might hold at the optimum \mathbf{x}^{opt} :

(a)

$$\frac{\partial C_t(\mathbf{x}^{opt}|\hat{\mathbf{u}})}{\partial P_m} = 0, m \in \{i, j\}$$

By setting Equation (A.1) equal to 0 for both batteries and considering Condition (4.6), we verify that the upper bound of Inequality (4.8) is achieved. This case is met under the assumption of Theorem 4.1.

(b)

$$\frac{\partial C_t(\mathbf{x}^{opt}|\hat{\mathbf{u}})}{\partial P_i} \cdot \frac{\partial C_t(\mathbf{x}^{opt}|\hat{\mathbf{u}})}{\partial P_j} > 0$$

If the derivative of the total cost function with respect to P_i at the optimum is strictly positive, this means that the value of P_i cannot be decreased further, which implies that it should take its minimum value, i.e.

$$\frac{P_i^{opt}}{S_i} = \left(\frac{P}{S}\right)_{min}$$

On the other hand, if the derivative is negative, then

$$\frac{P_i^{opt}}{S_i} = \left(\frac{P}{S}\right)_{max}$$

Appendix A. Proofs of Theorems of Chapter 4

Since the derivatives of C_t with respect to P_i and P_j have the same sign, and considering Assumptions (4.6) and (4.7), we get that in both of these cases we have $r_{P,i} = r_{P,j}$. Hence, Inequality (4.8) is satisfied.

(c)

$$\frac{\partial C_t(\mathbf{x}^{opt}|\hat{\mathbf{u}})}{\partial P_i} > 0, \frac{\partial C_t(\mathbf{x}^{opt}|\hat{\mathbf{u}})}{\partial P_j} = 0$$

Using the explanation of the previous point, we should have only for battery i

$$\frac{P_i^{opt}}{S_i} = \left(\frac{P}{S}\right)_{min}$$

and given Assumption (4.7) we should have:

$$r_{P,i} - r_{P,j} \leq 0 \tag{A.2}$$

Moreover we should have:

$$\begin{aligned} \frac{\partial C_t(\mathbf{x}^{opt}|\hat{\mathbf{u}})}{\partial P_i} - \frac{\partial C_t(\mathbf{x}^{opt}|\hat{\mathbf{u}})}{\partial P_j} > 0 \implies \\ \frac{a_P}{2}(r_{P,i} - r_{P,j}) > -\left(\frac{\partial J(\mathbf{x}^{opt}|\hat{\mathbf{u}})}{\partial P_i} - \frac{\partial J(\mathbf{x}^{opt}|\hat{\mathbf{u}})}{\partial P_j}\right) \end{aligned} \tag{A.3}$$

Combining (A.2) and (A.3), we derive that both sides of Inequality (A.3) are negative, therefore, taking the absolute value results in the desired Condition (4.8).

(d)

$$\frac{\partial C_t(\mathbf{x}^{opt}|\hat{\mathbf{u}})}{\partial P_i} < 0, \frac{\partial C_t(\mathbf{x}^{opt}|\hat{\mathbf{u}})}{\partial P_j} = 0$$

We can work in a similar way as case (d) and show that

$$r_{P,i} - r_{P,j} \geq 0 \tag{A.4}$$

and

$$\frac{a_P}{2}(r_{P,i} - r_{P,j}) < -\left(\frac{\partial J(\mathbf{x}^{opt}|\hat{\mathbf{u}})}{\partial P_i} - \frac{\partial J(\mathbf{x}^{opt}|\hat{\mathbf{u}})}{\partial P_j}\right) \tag{A.5}$$

Now, both scales of Inequality (A.5) are positive so taking the absolute value results once again in Condition (4.8).

(e)

$$\frac{\partial C_t(\mathbf{x}^{opt}|\hat{\mathbf{u}})}{\partial P_i} \cdot \frac{\partial C_t(\mathbf{x}^{opt}|\hat{\mathbf{u}})}{\partial P_j} < 0$$

The proof follows in the same way as in cases (c)-(d). In particular, we can show that either (A.2) and (A.3) will hold together or (A.4) together with (A.5).

We have, thus, concluded that Inequality (4.8) should hold for every possible values of $\frac{\partial C_t(\mathbf{x}^{opt}|\hat{\mathbf{u}})}{\partial P_m}$, $m \in \{i, j\}$. The same method can be used to prove the result for the reactive power.

A.2 Proof of Lemma 4.1

We assume that for some value $d > 0$ we have

$$|y_m^{opt} - y_m^*| > d \quad (\text{A.6})$$

which can be rewritten as:

$$\begin{aligned} y_m^{opt} &> y_m^* + d \\ \text{or } y_m^{opt} &< y_m^* - d \end{aligned} \quad (\text{A.7})$$

Because J_{y_m} is a convex function by design, then its derivative J'_{y_m} is an increasing function, which means that:

$$\begin{aligned} J'_{y_m}(y_m^{opt}) &> J'_{y_m}(y_m^* + d) \\ \text{and } J'_{y_m}(y_m^{opt}) &< J'_{y_m}(y_m^* - d) \end{aligned} \quad (\text{A.8})$$

Moreover, because $J_{y_m}(y_m + y_m^*)$ is also an even function by design, then $J'_{y_m}(y_m + y_m^*)$ is an odd function. This means that

$$J'_{y_m}(y_m^* + d) = -J'_{y_m}(y_m^* - d), \forall d \quad (\text{A.9})$$

Combining Conditions (A.8) and (A.9), we get

$$|J'_{y_m}(y_m^{opt})| > |J'_{y_m}(y_m^* \pm d)|, \forall d \quad (\text{A.10})$$

We consider any variable $x_j \in \{P_j, Q_j\}$, i.e. it represents either the active or the reactive power of battery j , such that the respective sensitivity coefficient satisfies the inequality $|K_{x_j}^m| \geq K_t(d, w_{y_m})$. Then, we compute the following quantity

$$w_{y_m} \left| \frac{\partial J(\mathbf{x}^{opt}|\hat{\mathbf{u}})}{\partial x_j} \right| \stackrel{(4.12)}{=} \frac{|J'_{y_m}(y_m^{opt})|}{|J'_{y_m}(y_m^* + d)|} \frac{|K_{x_j}^m|}{K_t(d, w_{y_m})} \stackrel{(A.10)}{>} 1 \quad (\text{A.11})$$

Considering the battery cost-function in the form of Equation (4.3) with $a_{P,j}, a_{Q,j} \in (0, 1], \forall j$ and the fact that for every battery we have $P_j, Q_j \in [-S_j, S_j]$ we derive the following inequality

$$\left| \frac{\partial C_j}{\partial x_j} \right| \leq 1, \forall j \quad (\text{A.12})$$

Appendix A. Proofs of Theorems of Chapter 4

From inequalities (A.11) and (A.12) we infer that we should have one the following two cases:

$$w_{y_m} \frac{\partial J(\mathbf{x}^{opt} | \hat{\mathbf{u}})}{\partial x_j} > 1 \implies x_j^{opt} = x_{j,min} \quad (\text{A.13})$$

$$w_{y_m} \frac{\partial J(\mathbf{x}^{opt} | \hat{\mathbf{u}})}{\partial x_j} < -1 \implies x_j^{opt} = x_{j,max} \quad (\text{A.14})$$

This result follows from the box form of the constraints of the problem in the same way as in case (b) of the proof of Theorem 4.2.

Now, we consider the following two cases:

A) $J'_{y_m}(y_m^{opt}) > 0$

In this case, for any variable x_j , with $|K_{x_j}^m| \geq K_t$ we have

$$\begin{cases} K_{x_j}^m > 0 \xrightarrow{(\text{A.13})} x_j^{opt} = x_{j,min} \\ K_{x_j}^m < 0 \xrightarrow{(\text{A.14})} x_j^{opt} = x_{j,max} \end{cases}$$

Therefore, no matter what is the value of the sensitivity $K_{x_j}^m$, the product $K_{x_j}^m x_j^{opt}$ takes the minimum possible value, which we denote as $K_{x_j}^m x_j^{opt} = (K_{x_j}^m x_j)_{min}$.

The next step is to examine the ordering of the following three points, namely (i) the value of y_m evaluated at the optimal solution y_m^{opt} , (ii) its minimum value within the domain of the problem y_m^{min} and (iii) the value that minimizes the grid cost within the same domain y_m^{inf} . Now we consider two cases regarding the point y_m^{inf} :

- i. The point that minimizes J_{y_m} is not stationary, i.e. $J'_{y_m}(y_m^{inf}) \neq 0$. Then, variable y_m must be constrained. Because $J'_{y_m}(y_m^{opt}) > 0$ by assumption, y_m must be constrained by its lower bound y_m^{min} , i.e. $y_m^{inf} = y_m^{min}$ and since y_m^{opt} is within the domain of y_m , we derive the ordering of the points as $y_m^{min} = y_m^{inf} \leq y_m^{opt}$
- ii. The point is stationary, i.e. $J'_{y_m}(y_m^{inf}) = 0$. Then variable y_m is not constrained, which means that $y_m^{inf} \geq y_m^{min}$ and $y_m^{opt} \geq y_m^{min}$. Now, considering the assumption that $J'_{y_m}(y_m^{opt}) > 0 = J'_{y_m}(y_m^{inf})$ and the fact that J'_{y_m} is an increasing function (by convexity), we get the following ordering of the points $y_m^{min} \leq y_m^{inf} < y_m^{opt}$

The ordering derived above can be re-written in the following way

$$J'_{y_m}(y_m^{opt}) > 0 \implies |y_m^{opt} - y_m^{inf}| \leq |y_m^{opt} - y_m^{min}| \quad (\text{A.15})$$

We can continue to show that

$$\begin{aligned}
 |y_m^{opt} - y_m^*| &\leq |y_m^* - y_m^{inf}| + |y_m^{opt} - y_m^{inf}| \leq \\
 &\leq |y_m^* - y_m^{inf}| + \left| \sum_i K_{x_i}^m x_i^{opt} - \sum_i (K_{x_i}^m x_i)_{min} \right| \leq \\
 &\leq |y_m^* - y_m^{inf}| + \sum_{|K_{x_i}^m| < K_t(d, w_{y_m})} |K_{x_i}^m| |x_{i,max} - x_{i,min}|
 \end{aligned} \tag{A.16}$$

B) $J'_{y_m}(y_m^{opt}) < 0$

We can show in a similar way, that in this case, we have $K_{x_j}^m x_j^{opt} = (K_{x_j}^m x_j)_{max}$ for any variable x_j with $|K_{x_j}^m| \geq K_t$ and that:

$$J'_{y_m}(y_m^{opt}) < 0 \implies |y_m^{opt} - y_m^{inf}| \leq |y_m^{opt} - y_m^{max}| \tag{A.17}$$

From this, we can show that we get again Inequality (A.16). Since the above inequalities are true for any $d > 0$, we can take as upper bound the minimum of these bounds over all values d . Hence, we get the upper bound $f(w_{y_m})$.

A.3 Proof of Theorem 4.4

Let $w_{y_m}^*$ be a solution to Problem 2. Considering the nature of the problem, this solution is the minimum value of w_{y_m} that satisfies a constraint, therefore it should be unique. By Definition (4.18) we have

$$f_u(w_{y_m}^*) = \min_d g(w_{y_m}^*, d) + |\Delta y_m|_{max} \tag{A.18}$$

Now, by evaluating $g(w_{y_m}^*, d)$ at $d = d_{max}^* - |\Delta y_m|_{max}$ we get

$$f_u(w_{y_m}^*) \leq g(w_{y_m}^*, d_{max,m}^* - |\Delta y_m|_{max}) + |\Delta y_m|_{max} \tag{A.19}$$

Also, because $w_{y_m}^*$ is a solution to Problem 2, it should satisfy Constraint (4.22). Combining it with the previous inequality we have

$$f_u(w_{y_m}^*) \leq d_{max,m}^* - |\Delta y_m|_{max} + |\Delta y_m|_{max} = d_{max,m}^* \tag{A.20}$$

which is equivalent to (4.21). Therefore, $w_{y_m}^*$ also satisfies the constraint of Problem 1.

Now, we assume another weight $w'_{y_m} \in (0, w_{y_m}^*)$ and denote $\Delta d_{max,m}^* = d_{max,m}^* - |\Delta y_m|_{max}$, for ease of notation. We will show that w'_{y_m} cannot satisfy the constraint of Problem 1. Let $d > 0$ be an arbitrary value. We consider the following two cases

1. $d > \Delta d_{max,m}^*$

Appendix A. Proofs of Theorems of Chapter 4

By the definition of function g in (4.14) we have

$$g(w'_{y_m}, d) = \max\{d, h(K_t(w'_{y_m}, d))\} \geq d > \Delta d_{max,m}^* \quad (\text{A.21})$$

2. $d < \Delta d_{max,m}^*$

By the definition of function K_t in (4.12) and the fact that J'_{y_m} is an increasing function (by convexity of J_{y_m}) we see that for a given argument w_{y_m} the function $K_t(w_{y_m}, d)$ is strictly decreasing for $d > 0$. And because we consider the case where $d < \Delta d_{max,m}^*$ we should have

$$K_t(w'_{y_m}, d) > K_t(w'_{y_m}, \Delta d_{max,m}^*) \quad (\text{A.22})$$

Now, from the definition of h in (4.13) we can derive that $h(K)$ is increasing in K , so from (A.22) we get

$$h(K_t(w'_{y_m}, d)) \geq h(K_t(w'_{y_m}, \Delta d_{max,m}^*)) \quad (\text{A.23})$$

Because $w'_{y_m} < w_{y_m}^*$ and $w_{y_m}^*$ is the solution to Problem 2, then w'_{y_m} should not satisfy constraint (4.22). Therefore, by using the term $\Delta d_{max,m}^*$ we defined in this proof we get

$$g(w'_{y_m}, \Delta d_{max,m}^*) > \Delta d_{max,m}^* \quad (\text{A.24})$$

Also, from the definition of g , we have

$$g(w'_{y_m}, \Delta d_{max,m}^*) = \max\{\Delta d_{max,m}^*, h(K_t(w'_{y_m}, \Delta d_{max,m}^*))\} \quad (\text{A.25})$$

and taking into account the last two conditions, we can infer that

$$h(K_t(w'_{y_m}, \Delta d_{max,m}^*)) > \Delta d_{max,m}^* \quad (\text{A.26})$$

Combining all the above results, we get

$$\begin{aligned} g(w'_{y_m}, d) &= \max\{d, h(K_t(w'_{y_m}, d))\} \geq \\ &\geq h(K_t(w'_{y_m}, d)) \geq h(K_t(w'_{y_m}, \Delta d_{max,m}^*)) \geq \\ &\geq \Delta d_{max,m}^* > d \end{aligned} \quad (\text{A.27})$$

Hence, we get $g(w'_{y_m}, d) > \Delta d_{max,m}^* \forall d \neq \Delta d_{max,m}^*$ and given the definition of $f_u(w_{y_m})$ in (4.18) we have

$$f_u(w'_{y_m}) > d_{max,m}^*, \forall w'_{y_m} < w_{y_m}^* \quad (\text{A.28})$$

which means that any $w'_{y_m} < w_{y_m}^*$ cannot be the solution to Problem 1. Therefore, $w_{y_m}^*$ is also the solution to Problem 1.

Bibliography

- [1] G. Rancilio, "Abate the barriers : Opening electricity markets to storage and res," Politecnico Milano, PhD dissertation, 2022. [Online]. Available: <https://hdl.handle.net/10589/188700>
- [2] A. Borghetti, M. Bosetti, S. Grillo, S. Massucco, C. A. Nucci, M. Paolone, and F. Silvestro, "Short-term scheduling and control of active distribution systems with high penetration of renewable resources," *IEEE Systems Journal*, vol. 4, no. 3, pp. 313–322, 2010.
- [3] R. K. Gupta, "Methods for grid-aware operation and planning of active distribution networks," EPFL PhD dissertation, 2023. [Online]. Available: <http://infoscience.epfl.ch/record/299705>
- [4] S. A. S. Fahmy, "Efficient methods for the operation of active distribution networks in unsymmetric and uncertain states," EPFL PhD dissertation, 2022. [Online]. Available: <http://infoscience.epfl.ch/record/298819>
- [5] F. Pilo, S. Jupe, F. Silvestro, C. Abbey, A. Baitch, B. Bak-Jensen, C. Carter-Brown, G. Celli, K. El Bakari, P. Georgilakis, T. Hearne, L. Ochoa, G. Petretto, and J. Taylor, "Planning and optimization methods for active distribution systems," 08 2014.
- [6] N. Hatziargyriou, *Microgrids: Architectures and Control*, ser. Wiley - IEEE. Wiley, 2014.
- [7] A. Bernstein, L. Reyes-Chamorro, J.-Y. Le Boudec, and M. Paolone, "A composable method for real-time control of active distribution networks with explicit power setpoints. Part I: Framework," *Electric Power Systems Research*, vol. 125, pp. 254 – 264, 2015.
- [8] L. Reyes, A. Bernstein, J.-Y. Le Boudec, and M. Paolone, "A composable method for real-time control of active distribution networks with explicit power setpoints. Part II: Implementation and validation," *Electric Power Systems Research*, vol. 125, 04 2015.
- [9] J. Machowski, J. Bialek, and J. Bumby, "Power system dynamics. stability and control," 01 2012.
- [10] T. L. Vandoorn, B. Meersman, J. D. M. D. Kooning, and L. Vandeveldel, "Directly-coupled synchronous generators with converter behavior in islanded microgrids," *IEEE Transactions on Power Systems*, vol. 27, pp. 1395–1406, 2012.

Bibliography

- [11] R. Palma-Behnke, C. Benavides, F. Lanas, B. Severino, L. Reyes, J. Llanos, and D. Sáez, "A microgrid energy management system based on the rolling horizon strategy," *IEEE Transactions on Smart Grid*, vol. 4, no. 2, pp. 996–1006, 2013.
- [12] "Trends in local electricity market design: Regulatory barriers and the role of grid tariffs," *Journal of Cleaner Production*, vol. 358, p. 131805, 2022. [Online]. Available: <https://www.sciencedirect.com/science/article/pii/S0959652622014159>
- [13] F. Sossan, E. Namor, R. Cherkaoui, and M. Paolone, "Achieving the dispatchability of distribution feeders through prosumers data driven forecasting and model predictive control of electrochemical storage," *IEEE Transactions on Sustainable Energy*, vol. 7, no. 4, pp. 1762–1777, 2016.
- [14] T. Logenthiran, D. Srinivasan, A. Khambadkone, and H. Aung, "Multiagent system for real-time operation of a microgrid in real-time digital simulator," 2012.
- [15] R. R. Appino, J. Ángel González Ordiano, R. Mikut, T. Faulwasser, and V. Hagenmeyer, "On the use of probabilistic forecasts in scheduling of renewable energy sources coupled to storages," *Applied Energy*, vol. 210, pp. 1207–1218, 2018. [Online]. Available: <https://www.sciencedirect.com/science/article/pii/S0306261917311492>
- [16] M. Bozorg, F. Sossan, J.-Y. Le Boudec, and M. Paolone, "Influencing the bulk power system reserve by dispatching power distribution networks using local energy storage," *Electric Power Systems Research*, vol. 163, pp. 270–279, 2018. [Online]. Available: <https://www.sciencedirect.com/science/article/pii/S0378779618301901>
- [17] G. Valverde and T. Van Cutsem, "Model predictive control of voltages in active distribution networks," *IEEE Transactions on Smart Grid*, vol. 4, no. 4, pp. 2152–2161, 2013.
- [18] B. Wang, G. Cai, and D. Yang, "Dispatching of a wind farm incorporated with dual-battery energy storage system using model predictive control," *IEEE Access*, vol. 8, pp. 144 442–144 452, 2020.
- [19] R. Gupta, A. Zecchino, J.-H. Yi, and M. Paolone, "Reliable dispatch of active distribution networks via a two-layer grid-aware model predictive control: Theory and experimental validation," *IEEE Open Access Journal of Power and Energy*, vol. 9, pp. 465–478, 2022.
- [20] A. Dimeas and N. Hatziaargyriou, "Operation of a multiagent system for microgrid control," *IEEE Transactions on Power Systems*, vol. 20, no. 3, pp. 1447–1455, 2005.
- [21] D. Khastieva, M. R. Hesamzadeh, I. Vogelsang, J. Rosellón, and M. Amelin, "Value of energy storage for transmission investments," *Energy Strategy Reviews*, vol. 24, pp. 94–110, 2019. [Online]. Available: <https://www.sciencedirect.com/science/article/pii/S2211467X19300070>
- [22] S. Bjarghov, M. Löschenbrand, A. U. N. Ibn Saif, R. Alonso Pedrero, C. Pfeiffer, S. K. Khadem, M. Rabelhofer, F. Revheim, and H. Farahmand, "Developments and challenges

- in local electricity markets: A comprehensive review,” *IEEE Access*, vol. 9, pp. 58 910–58 943, 2021.
- [23] C. Park and T. Yong, “Comparative review and discussion on p2p electricity trading,” *Energy Procedia*, vol. 128, pp. 3–9, 2017, international Scientific Conference “Environmental and Climate Technologies”, CONECT 2017, 10-12 May 2017, Riga, Latvia. [Online]. Available: <https://www.sciencedirect.com/science/article/pii/S1876610217338456>
- [24] M. F. Zia, M. Benbouzid, E. Elbouchikhi, S. M. Muyeen, K. Techato, and J. M. Guerrero, “Microgrid transactive energy: Review, architectures, distributed ledger technologies, and market analysis,” *IEEE Access*, vol. 8, pp. 19 410–19 432, 2020.
- [25] P. S. Georgilakis, “Review of computational intelligence methods for local energy markets at the power distribution level to facilitate the integration of distributed energy resources: State-of-the-art and future research,” *Energies*, vol. 13, no. 1, 2020. [Online]. Available: <https://www.mdpi.com/1996-1073/13/1/186>
- [26] A. Picciariello, J. Reneses, P. Frias, and L. Söder, “Distributed generation and distribution pricing: Why do we need new tariff design methodologies?” *Electric Power Systems Research*, vol. 119, pp. 370–376, 2015. [Online]. Available: <https://www.sciencedirect.com/science/article/pii/S0378779614003927>
- [27] M. Dynge, E. N. Anfinnsen, and U. Cali, “Evaluating fairness indicators for local energy markets,” 05 2023.
- [28] F. Moret and P. Pinson, “Energy collectives: A community and fairness based approach to future electricity markets,” *IEEE Transactions on Power Systems*, vol. 34, no. 5, pp. 3994–4004, 2019.
- [29] A. K. Zarabie, S. Das, and M. N. Faqiry, “Fairness-regularized dlmp-based bilevel transactive energy mechanism in distribution systems,” *IEEE Transactions on Smart Grid*, vol. 10, no. 6, pp. 6029–6040, 2019.
- [30] N. Gueissaz, K. Christakou, J.-Y. Le Boudec, and M. Paolone, “Fair control of distributed PV plants in low voltage grids,” in *2017 IEEE PES Innovative Smart Grid Technologies Conference Europe (ISGT-Europe)*, 2017, pp. 1–6.
- [31] D. Gebbran, S. Mhanna, Y. Ma, A. C. Chapman, and G. Verbič, “Fair coordination of distributed energy resources with volt-var control and PV curtailment,” *Applied Energy*, vol. 286, p. 116546, 2021. [Online]. Available: <https://www.sciencedirect.com/science/article/pii/S0306261921000933>
- [32] K. Petrou, M. Liu, A. Procopiou, L. Ochoa, J. Theunissen, and J. Harding, “Operating envelopes for prosumers in LV networks: A weighted proportional fairness approach,” 10 2020.

Bibliography

- [33] D. Zhang, N. J. Samsatli, A. D. Hawkes, D. J. Brett, N. Shah, and L. G. Papageorgiou, "Fair electricity transfer price and unit capacity selection for microgrids," *Energy Economics*, vol. 36, pp. 581–593, 2013. [Online]. Available: <https://www.sciencedirect.com/science/article/pii/S0140988312002794>
- [34] Y. Yang, G. Hu, and C. Spanos, "Optimal sharing and fair cost allocation of community energy storage," *IEEE Transactions on Smart Grid*, vol. PP, pp. 1–1, 05 2021.
- [35] F. Asarias and M. A. Pedrasa, "A transactive energy market framework considering network constraints and fairness," 2021.
- [36] M. D. de Souza Dutra and N. Alguacil, "Fairness of prosumers' incentives in residential demand response: A practical decentralized optimization approach," *International Journal of Electrical Power & Energy Systems*, vol. 148, p. 109015, 2023. [Online]. Available: <https://www.sciencedirect.com/science/article/pii/S0142061523000728>
- [37] G. O'Brien, A. El Gamal, and R. Rajagopal, "Shapley value estimation for compensation of participants in demand response programs," *IEEE Transactions on Smart Grid*, vol. 6, no. 6, pp. 2837–2844, 2015.
- [38] D. R. Biggar and M. R. Hesamzadeh, "An integrated theory of dispatch and hedging in wholesale electric power markets," *Energy Economics*, vol. 112, p. 106055, 2022. [Online]. Available: <https://www.sciencedirect.com/science/article/pii/S0140988322002225>
- [39] I. I. Avramidis, F. Capitanescu, and G. Deconinck, "A comprehensive multi-period optimal power flow framework for smart LV networks," *IEEE Transactions on Power Systems*, vol. 36, no. 4, pp. 3029–3041, 2021.
- [40] I.-I. Avramidis, F. Capitanescu, and G. Deconinck, "Thoughts on conceiving a "fair" value for flexibility," *International Journal of Electrical Power & Energy Systems*, vol. 147, p. 108893, 2023. [Online]. Available: <https://www.sciencedirect.com/science/article/pii/S0142061522008894>
- [41] A. M. Jadhav, N. R. Patne, and J. M. Guerrero, "A novel approach to neighborhood fair energy trading in a distribution network of multiple microgrid clusters," *IEEE Transactions on Industrial Electronics*, vol. 66, no. 2, pp. 1520–1531, 2019.
- [42] H. Cai and G. Hu, "Distributed control scheme for package-level state-of-charge balancing of grid-connected battery energy storage system," *IEEE Transactions on Industrial Informatics*, vol. 12, no. 5, pp. 1919–1929, 2016.
- [43] H. Wang, Z. Wu, G. Shi, and Z. Liu, "SOC balancing method for hybrid energy storage system in microgrid," in *2019 IEEE 3rd International Conference on Green Energy and Applications (ICGEA)*, 2019, pp. 141–145.
- [44] M. Eydi and R. Ghazi, "A novel communication-less control method to improve proportional power-sharing and SOCs balancing in a geographically dispersed hybrid

- AC/DC microgrid,” *Electric Power Systems Research*, vol. 209, p. 107989, 2022. [Online]. Available: <https://www.sciencedirect.com/science/article/pii/S0378779622002097>
- [45] S. Ouoba, A. Houari, and M. Machmoum, “Robust SoC balancing method for distributed storage based islanded microgrids,” in *IECON 2021 – 47th Annual Conference of the IEEE Industrial Electronics Society*, 2021, pp. 1–6.
- [46] C. Li, E. A. A. Coelho, T. Dragicevic, J. M. Guerrero, and J. C. Vasquez, “Multiagent-based distributed state of charge balancing control for distributed energy storage units in AC microgrids,” *IEEE Transactions on Industry Applications*, vol. 53, no. 3, pp. 2369–2381, 2017.
- [47] C.-K. Nguyen, T.-T. Nguyen, H.-J. Yoo, and H.-M. Kim, “Consensus-based SOC balancing of battery energy storage systems in wind farm,” *Energies*, vol. 11, no. 12, 2018. [Online]. Available: <https://www.mdpi.com/1996-1073/11/12/3507>
- [48] Y. Xu, Z. Li, J. Zhao, and J. Zhang, “Distributed robust control strategy of grid-connected inverters for energy storage systems’ state-of-charge balancing,” *IEEE Transactions on Smart Grid*, vol. 9, no. 6, pp. 5907–5917, 2018.
- [49] W. Xie and X. Xia, “Distributed energy dispatch of electrical energy storage systems using consensus control approach,” *IFAC-PapersOnLine*, vol. 51, no. 13, pp. 229–234, 2018, 2nd IFAC Conference on Modelling, Identification and Control of Nonlinear Systems MICNON 2018. [Online]. Available: <https://www.sciencedirect.com/science/article/pii/S240589631831036X>
- [50] O. Montoya Giraldo, A. Arias-Londoño, V. Garrido, W. Gil González, and L. Grisales-Noreña, “A quadratic convex approximation for optimal operation of battery energy storage systems in dc distribution networks,” *Energy Systems*, 11 2021.
- [51] G. Krishnamoorthy, A. Dubey, and A. H. Gebremedhin, “Reinforcement learning for battery energy storage dispatch augmented with model-based optimizer,” in *2021 IEEE International Conference on Communications, Control, and Computing Technologies for Smart Grids (SmartGridComm)*, 2021, pp. 289–294.
- [52] Y. Xu, T. Zhao, S. Zhao, J. Zhang, and Y. Wang, “Multi-objective chance-constrained optimal day-ahead scheduling considering bess degradation,” *CSEE Journal of Power and Energy Systems*, vol. 4, no. 3, pp. 316–325, 2018.
- [53] B. Wang, C. Zhang, and Z. Y. Dong, “Interval optimization based coordination of demand response and battery energy storage system considering SOC management in a microgrid,” *IEEE Transactions on Sustainable Energy*, vol. 11, no. 4, pp. 2922–2931, 2020.
- [54] S. Wang, F. Yang, X. Bai, S. Liu, and C. Yue, “Optimal power dispatch strategy for multiple battery containers in a grid-scale bess station,” in *2019 IEEE PES Asia-Pacific Power and Energy Engineering Conference (APPEEC)*, 2019, pp. 1–5.

Bibliography

- [55] A. Nurkanovic, A. Mešanović, A. Zanelli, G. Frison, J. Frey, S. Albrecht, and M. Diehl, “Real-time nonlinear model predictive control for microgrid operation,” 07 2020.
- [56] M. Cintuglu, T. Youssef, and O. Mohammed, “Development and application of a real-time testbed for multiagent system interoperability: A case study on hierarchical microgrid control,” in *2017 IEEE Power Energy Society General Meeting*, 2017, pp. 1–1.
- [57] B. Zhao, X. Zhang, J. Chen, C. Wang, and L. Guo, “Operation optimization of standalone microgrids considering lifetime characteristics of battery energy storage system,” *IEEE Transactions on Sustainable Energy*, vol. 4, no. 4, pp. 934–943, 2013.
- [58] R. de Azevedo, M. H. Cintuglu, T. Ma, and O. A. Mohammed, “Multiagent-based optimal microgrid control using fully distributed diffusion strategy,” *IEEE Transactions on Smart Grid*, vol. 8, no. 4, pp. 1997–2008, 2017.
- [59] C. M. Colson and M. H. Nehrir, “Comprehensive real-time microgrid power management and control with distributed agents,” *IEEE Transactions on Smart Grid*, vol. 4, no. 1, pp. 617–627, 2013.
- [60] K. Zhang, W. Shi, H. Zhu, E. Dall’Anese, and T. Başar, “Dynamic power distribution system management with a locally connected communication network,” *IEEE Journal of Selected Topics in Signal Processing*, vol. 12, no. 4, pp. 673–687, 2018.
- [61] B. Hayes, J. Gruber, and M. Prodanovic, “Short-term load forecasting at the local level using smart meter data,” in *PowerTech, 2015 IEEE Eindhoven*, June 2015, pp. 1–6.
- [62] R. Rudnik, C. Wang, L. Reyes-Chamorro, J. Achara, J.-Y. L. Boudec, and M. Paolone, “Real-time control of an electric vehicle charging station while tracking an aggregated power setpoint,” *IEEE Transactions on Industry Applications*, vol. 56, no. 5, pp. 5750–5761, 2020.
- [63] E. Scolari, D. Torregrossa, J.-Y. Le Boudec, and M. Paolone, “Ultra-short-term prediction intervals of photovoltaic AC active power,” in *2016 International Conference on Probabilistic Methods Applied to Power Systems (PMAPS)*, 2016, pp. 1–8.
- [64] W. U. Rehman, A. Moeini, O. Oboreh-Snapps, R. Bo, and J. Kimball, “Deadband voltage control and power buffering for extreme fast charging station,” in *2021 IEEE Madrid PowerTech*, 2021, pp. 1–6.
- [65] L. Reyes-Chamorro, W. Saab, R. Rudnik, A. M. Kettner, M. Paolone, and J. Le Boudec, “Slack selection for unintentional islanding: Practical validation in a benchmark microgrid,” in *2018 Power Systems Computation Conference (PSCC)*, 2018, pp. 1–7.
- [66] R. Posree and S. Sirisumrannukul, “Voltage sag assessment in distribution system with neutral grounding resistance by methods of fault position and monte carlo simulation,” in *2021 5th International Conference on Power and Energy Engineering (ICPEE)*, 2021, pp. 26–31.

- [67] “Voltage sag prediction for network planning,” *Electric Power Systems Research*, vol. 140, pp. 976–983, 2016. [Online]. Available: <https://www.sciencedirect.com/science/article/pii/S0378779616300803>
- [68] M. Bollen and I. Gu, *Signal Processing of Power Quality Disturbances*, ser. IEEE Press Series on Power and Energy Systems. Wiley, 2006. [Online]. Available: <https://books.google.ch/books?id=tOhSAAAAMAAJ>
- [69] M. Cho, J. Hwang, and C. Chen, “Customer short term load forecasting by using arima transfer function model,” in *Energy Management and Power Delivery, 1995. Proceedings of EMPD’95., 1995 International Conference on*, vol. 1. IEEE, 1995, pp. 317–322.
- [70] R. Mamlook, O. Badran, and E. Abdulhadi, “A fuzzy inference model for short-term load forecasting,” *Energy Policy*, vol. 37, no. 4, pp. 1239 – 1248, 2009.
- [71] F. Sossan, V. Lakshmanan, G. Costanzo, M. Marinelli, P. Douglas, and H. Bindner, “Grey-box modelling of a household refrigeration unit for energy consumption prediction and optimization using time series data,” 2013, currently unpublished.
- [72] F. Sossan, H. Bindner, H. Madsen, L. Reyes, D. Torregrossa, and M. Paolone, “A MPC replacement strategy for electric space heating including cogeneration of a fuel cell-electrolyzer system,” *International Journal of Electrical Power & Energy Systems*, 2013.
- [73] A. Azadeh, S. Ghaderi, and S. Sohrabkhani, “Annual electricity consumption forecasting by neural network in high energy consuming industrial sectors,” *Energy Conversion and Management*, vol. 49, no. 8, pp. 2272–2278, 2008.
- [74] H. K. Alfares and M. Nazeeruddin, “Electric load forecasting: literature survey and classification of methods,” *International Journal of Systems Science*, vol. 33, no. 1, pp. 23–34, 2002.
- [75] H. Hahn, S. Meyer-Nieberg, and S. Pickl, “Electric load forecasting methods: Tools for decision making,” *European Journal of Operational Research*, vol. 199, no. 3, pp. 902–907, 2009.
- [76] M. Tan, S. Yuan, S. Li, Y. Su, H. Li, and F. He, “Ultra-short-term industrial power demand forecasting using LSTM based hybrid ensemble learning,” *IEEE Transactions on Power Systems*, vol. 35, no. 4, pp. 2937–2948, 2020.
- [77] Z. Wang and A. Perera, “Robust optimization of power grid with distributed generation and improved reliability,” *Energy Procedia*, vol. 159, pp. 400–405, 2019, renewable Energy Integration with Mini/Microgrid. [Online]. Available: <https://www.sciencedirect.com/science/article/pii/S187661021831364X>
- [78] H. A. Nielsen, H. Madsen, and T. S. Nielsen, “Using quantile regression to extend an existing wind power forecasting system with probabilistic forecasts,” *Wind Energy*, vol. 9, no. 1-2, pp. 95–108, 2006.

Bibliography

- [79] P. Pinson, "Estimation of the uncertainty in wind power forecasting," 2006.
- [80] M. Rana, I. Koprinska, A. Khosravi, and V. Agelidis, "Prediction intervals for electricity load forecasting using neural networks," in *Neural Networks (IJCNN), The 2013 International Joint Conference on*, Aug 2013, pp. 1–8.
- [81] T. Xiong, Y. Bao, and Z. Hu, "Interval forecasting of electricity demand: A novel bivariate emd-based support vector regression modeling framework," *International Journal of Electrical Power & Energy Systems*, vol. 63, no. 0, pp. 353 – 362, 2014.
- [82] R. Rudnik, J. Le Boudec, A. Bernstein, L. Reyes-Chamorro, and M. Paolone, "Handling large power steps in real-time microgrid control via explicit power setpoints," in *2017 IEEE Manchester PowerTech*, 2017, pp. 1–6.
- [83] K. Christakou, J.-Y. LeBoudec, M. Paolone, and D.-C. Tomozei, "Efficient computation of sensitivity coefficients of node voltages and line currents in unbalanced radial electrical distribution networks," *IEEE Transactions on Smart Grid*, vol. 4, no. 2, pp. 741–750, 2013.
- [84] A. Bernstein, C. Wang, E. Dall'Anese, J.-Y. Le Boudec, and C. Zhao, "Load flow in multi-phase distribution networks: Existence, uniqueness, non-singularity and linear models," *IEEE Transactions on Power Systems*, vol. 33, no. 6, pp. 5832–5843, 2018.
- [85] L. E. Reyes Chamorro, "Real-time control framework for active distribution networks theoretical definition and experimental validation," p. 176, EPFL PhD dissertation, 2016. [Online]. Available: <http://infoscience.epfl.ch/record/221619>
- [86] "EN 50160, Voltage characteristics of electricity supplied by public distribution systems, 2023."
- [87] "IEC 60287-1-1, Electric cables - Calculation of the current rating - Part 1-1: Current rating equations (100 % load factor) and calculation of losses - General, 2023."
- [88] M. Nick, "Exact convex modeling of the optimal power flow for the operation and planning of active distribution networks with energy storage systems," p. 208, 2016, EPFL PhD dissertation, 2016. [Online]. Available: <http://infoscience.epfl.ch/record/218631>
- [89] S. Papathanassiou, N. Hatziargyriou, and K. Strunz, "A benchmark low voltage microgrid network," *CIGRE Symposium*, 01 2005.
- [90] M. Baran and F. Wu, "Optimal sizing of capacitors placed on a radial distribution system," *IEEE Transactions on Power Delivery*, vol. 4, no. 1, pp. 735–743, 1989.
- [91] E. Stai, L. Reyes-Chamorro, F. Sossan, J.-Y. Le Boudec, and M. Paolone, "Dispatching stochastic heterogeneous resources accounting for grid and battery losses," *IEEE Transactions on Smart Grid*, vol. 9, no. 6, pp. 6522–6539, 2018.

- [92] Z. Yuan, A. Zecchino, R. Cherkaoui, and M. Paolone, "Real-time control of battery energy storage systems to provide ancillary services considering voltage-dependent capability of DC-AC converters," *IEEE Transactions on Smart Grid*, vol. 12, no. 5, pp. 4164–4175, 2021.
- [93] P. Grammatikos, F. Sossan, J.-Y. L. Boudec, and M. Paolone, "Computation of ultra-short-term prediction intervals of the power prosumption in active distribution networks," accepted to PSCC 2024.
- [94] H. Chernoff, S.-H. Lo, and T. Zheng, "Discovering influential variables: a method of partitions," *The Annals of Applied Statistics*, pp. 1335–1369, 2009.
- [95] M. Pignati, M. Popovic, S. Barreto Andrade, R. Cherkaoui, D. Flores, J.-Y. Le Boudec, M. M. Maaz, M. Paolone, P. Romano, S. Sarri, T. T. Tesfay, D.-C. Tomozei, and L. Zanni, "Real-Time State Estimation of the EPFL-Campus Medium-Voltage Grid by Using PMUs," in *The Sixth Conference on Innovative Smart Grid Technologies (ISGT2015)*, 2014.
- [96] A. Khosravi, S. Nahavandi, and D. Creighton, "Prediction intervals for short-term wind farm power generation forecasts," *IEEE Transactions on Sustainable Energy*, vol. 4, no. 3, p. 602 – 610, 2013.
- [97] P. Grammatikos, M. Paolone, and J.-Y. Le Boudec, "Design of cost functions for the real-time control of microgrids hosting distributed energy-storage systems," *Sustainable Energy, Grids and Networks*, vol. 35, p. 101141, 2023. [Online]. Available: <https://www.sciencedirect.com/science/article/pii/S2352467723001492>
- [98] T. Saaty, "Decision making — the analytic hierarchy and network processes (ahp/ anp)," *Journal of Systems and Systems Engineering*, vol. 13, pp. 1–35, 03 2004.
- [99] L. Reyes-Chamorro, A. Bernstein, N. J. Bouman, E. Scolari, A. M. Kettner, B. Cathiard, J.-Y. Le Boudec, and M. Paolone, "Experimental validation of an explicit power-flow primary control in microgrids," *IEEE Transactions on Industrial Informatics*, vol. 14, no. 11, pp. 4779–4791, 2018.
- [100] E. Scolari, D. Torregrossa, J.-Y. Le Boudec, and M. Paolone, "Ultra-short-term prediction intervals of photovoltaic AC active power," 10 2016, pp. 1–8.
- [101] A. Zecchino, R. Gupta, P. Grammatikos, and M. Paolone, "Compilation of real-time control strategies for heterogeneous resources at MV and LV," SCCER-FURIES technical report 2021, <https://infoscience.epfl.ch/record/293429>.
- [102] A. Zecchino, Z. Yuan, F. Sossan, R. Cherkaoui, and M. Paolone, "Optimal provision of concurrent primary frequency and local voltage control from a bess considering variable capability curves: Modelling and experimental assessment," *Electric Power Systems Research*, vol. 190, p. 106643, 2021. [Online]. Available: <https://www.sciencedirect.com/science/article/pii/S0378779620304466>

Bibliography

- [103] M. Nick, R. Cherkaoui, J.-Y. L. Boudec, and M. Paolone, “An exact convex formulation of the optimal power flow in radial distribution networks including transverse components,” *IEEE Transactions on Automatic Control*, vol. 63, no. 3, pp. 682–697, 2018.
- [104] W. Holmgren, C. Hansen, and M. Mikofski, “pvlib python: a python package for modeling solar energy systems,” *Journal of Open Source Software*, vol. 3, p. 884, 09 2018.

Plouton Grammatikos

PHD STUDENT AT EPFL

PPH 331, Station 13, EPFL, 1015 Lausanne, CH

☎ +41 782157842 | ✉ plouton.grammatikos@epfl.ch | 📅 December 20th, 1995 | 🌐 plouton-grammatikos

Education

École Polytechnique Fédérale de Lausanne (EPFL)

Lausanne, CH

Ph.D. in Computer and Communication Sciences (in collaboration with the school of engineering)

Sept 1st 2019 - May 15th 2024

- Thesis title: Fair Real-Time Control of Energy Storage Systems in Active Distribution Networks in the Presence of Uncertainties
- Thesis supervisors: Mario Paolone and Jean-Yves Le Boudec

National Technical University of Athens (NTUA)

Athens, GR

Diploma in Electrical and Computer Engineering (integrated Masters)

Dec 2013 - Oct 2018

- Major in Communications (Telecommunications, Networking, Electronics)
- GPA: 9.56/10 – Excellent
- Thesis title: Application of Mobile Edge Computing in Vehicular Communications.
- Thesis supervisor: Panayotis Cottis

Work Experience

Distributed Electrical Systems Laboratory, EPFL

Lausanne, CH

Doctoral Researcher

Sept 1st 2019 - Current

- Optimization strategies for the real-time control of active distribution networks with a focus on fairness.
- Forecasting of nodal demand and generation using machine-learning techniques.
- Implementation and experimental validation of control frameworks on the EPFL smart-grid platform and a medium-voltage distribution network in Aigle Switzerland.

Vodafone Greece

Athens, GR

Internship

Oct 29th 2018 - Dec 21st 2018

- Training on core network management required for the research project: “TCP optimization in LTE systems by leveraging information available at the Radio Access Network” in collaboration with Prof. Panayotis Cottis at NTUA.

Hellenic Telecommunications & Post Commission (EETT)

Athens, GR

Internship

July 7th 2017 - Sept 9th 2017

- Evaluation and approval of requests submitted by the Greek mobile network operators to upgrade their cellular base station antennas.
- Development of a web application to provide information on the allocation of the radio frequency spectrum in Greece.
- Training on various spectrum management and monitoring issues.

Publications

JOURNAL ARTICLES

Design of cost functions for the real-time control of microgrids hosting distributed energy-storage systems

Plouton Grammatikos, Mario Paolone, Jean-Yves Le Boudec

Sustainable Energy, Grids and Networks p. 101141. 2023

A mobile edge computing approach for vehicle to everything communications

Plouton V. Grammatikos, Panayotis G. Cottis

Communications and Network pp. 65–81. 2019

CONFERENCE PROCEEDINGS

Computation of ultra-short-term prediction intervals of the power prosumption in active distribution networks

Plouton Grammatikos, Fabrizio Sossan, Jean-Yves Le Boudec, Mario Paolone

PSCC 2024

TECHNICAL REPORTS

Compilation of real-time control strategies for heterogeneous resources at MV and LV

Antonio Zecchino, Rahul Gupta, Plouton Grammatikos, Mario Paolone

SCCER-FURIES technical report 2021, <https://infoscience.epfl.ch/record/293429>

IN PREPARATION

Experimental Validation of a Two-Layer Model Predictive Control for the Fair Control of Batteries Hosted in Active Distribution Networks

Plouton Grammatikos, Rahul Gupta, Matthieu Benoit C. Jacobs, Jean-Yves Le Boudec, Mario Paolone

Presentations

- Short-term forecasting of unmonitored photovoltaics generation. Proposed challenge for the Energy Data Hackdays, Brugg CH, Sept 24th 2021
- Experimental validation of COMMELEC in the Aigle demonstrator. Industry Day, Aigle CH, Aug 31st 2021

Teaching Activities

EPFL

Feb 2020 - Jan 2024

- Prepared lab exercises for the courses “Smart Grids Technologies” and “TCP/IP Networking”.
- Provided assistance to students in the courses “Analysis I” and “Probability and Statistics”.

Supervised Student Projects

EPFL

- Design and evaluation of an MPC for the fair control of batteries. Master Semester Project by Louis-Dardaye Dramé, Fall 2022
- Development of a graphical user interface for a grid-control emulator. Bachelor Semester Project by Emma Romanetti, Fall 2022
- Data analytics for the forecasting of electricity prosumption in real time. Master Semester Project by Hafsa Aoutir, Spring 2022
- Development of a discrete event simulator for the real-time control of electrical grids. Master Semester Project by Alexandre Dherse, Spring 2022
- Development of a simulator for evaluating algorithms for short-term forecasting of electricity prosumption. Master Semester Project by Louis-Nicolas Durand, Fall 2021
- Probabilistic Forecasting of Electricity Demand and PV Generation for Microgrids Applications. Master Thesis by Kristijan Lopatichki, Fall 2020
- Simulation of a real-time charging algorithm for electric vehicles. Bachelor Semester project by Etienne Bruno, Fall 2020

Skills

Expertise Optimal Power Flow, Real-Time Grid Control, Forecasting, Machine Learning, Computer Networking

Software MATLAB, C/C++, Python, LabVIEW, Git, \LaTeX

Languages

Greek Native proficiency

English Professional proficiency

French Elementary proficiency